Karlsruher Institut für Technologie (KIT)

Control of Solar Thermal Linear Fresnel Collector Plants in Single Phase and Direct Steam Generation Modes

Zur Erlangung des akademischen Grades

Doktor der Ingenieurwissenschaften

der Fakultät für Maschinenbau
Karlsruher Institut für Technologie (KIT)

genehmigte

Dissertation

von

Marwan M. Mokhtar

Institut für Neutronenphysik und Reaktortechnik (INR)

Tag der mündlichen Prüfung: 14.09.2018

Hauptreferent:
Prof. Dr.-Ing. Robert Stieglitz
Karlsruher Institut für Technologie (KIT)

Korreferent:
Prof. Dr. Hans-Martin Henning
Fraunhofer-Institut für Solare Energiesysteme (ISE)

Karlsruhe, 2019
KIT – Die Forschungsuniversität in der Helmholtz-Gemeinschaft

Abstract

One key difference between renewable energy and fossil fuels originates from temporal availability. While energy flow in a fossil powered process can be controlled, this is not the case for most renewable energy sources. In the case of solar energy, not only is the energy source not controllable, but it is often practically not predictable. This seemingly slight difference has far reaching implications that has spurred research in different areas of science and engineering including, storage, hybrid systems, dynamic behavior, partial load operation and of course control systems.

The main objective of this work is to develop suitable control laws for solar thermal systems capable of dealing with the intermittent nature of the solar resource. A good control strategy will maximize solar energy use, minimize downtime, provide good setpoint tracking and increase system stability and robustness, all while maintaining personnel and equipment safety at highest priority.

This research is divided into two main parts, the first part deals with the control system of the concentrated solar thermal system in single phase flow mode of operation, where the main controlled parameter is the temperature at the exit of the solar field. Several control systems have been tested experimentally for different situations and process requirements and it was found that advanced Proportional–Integral–Derivative (PID) control with suitable feed forward loops provides a very good performance while maintaining design and implementation simplicity.

The second part is dedicated to the control of the solar system in direct steam generation mode where the main controlled parameter is the steam pressure at the consumer process. In direct steam generation mode, the system is considered a multi input multi output control system. Two main control strategies were developed and tested within this work, one is based on advanced PID control and feed forward and the other is based on Model Predictive Control (MPC) theory.

The former was thoroughly developed within this work and has been extensively tested under real life conditions for several years now. The latter is a new promising technique offering a universal control law that has the potential of reducing control system deployment and commissioning times. This of course comes at the cost of a more complex control law that requires big research and development efforts.

This thesis proves that, in spite of the complicated dynamics of solar thermal plants, reliable and robust energy delivery can be achieved through carefully designed systems employing suitable control strategies.

Zusammenfassung

Ein wesentlicher Unterschied erneuerbarer Energiequellen zu fossilen Energieträgern liegt in der zeitlichen Verfügbarkeit. Im Gegensatz zu fossil angetriebenen Prozessen lässt sich die Energiezufuhr nicht regeln. Dies stellt vor allem die Solarenergie vor eine wesentliche Herausforderung. Die Sonne als Energiequelle unterliegt nicht nur tages- bzw. jahreszeitlichen Schwankungen, sie ist oft auch nicht vorhersehbar. Dieser scheinbar kleine Unterschied zur fossilen Energiegewinnung, hat zu weitreichenden Forschungsaktivitäten in verschiedenen Bereichen der Wissenschaft und des Ingenieurwesens geführt, darunter die Entwicklung von Speichertechnologien und hybrider Systeme, die Abbildung des dynamischen Verhaltens, insbesondere im Teillastbetrieb und nicht zu Letzt die entsprechende Ausarbeitung verschiedener Regelsysteme.

Das Hauptziel der vorliegenden Arbeit ist die Entwicklung geeigneter Regelgesetze für solarthermische Anlagen um der intermittierenden Natur der Sonne als Energieressource gerecht zu werden. Eine gute Regelung erhöht den Solarertrag, reduziert Stillstände, bietet eine optimierte Wahl des Betriebspunktes und garantiert die Stabilität und Robustheit des Systems, mit der Personen- und Anlagensicherheit als oberste Priorität.

Die Thesis gliedert sich in zwei Hauptteile. Der erste Teil beinhaltet die Regelungstechnik konzentrierender, solarthermischer Systeme mit einphasigen Strömungen. Als wesentliche Regelgröße dient die Kollektoraustritttemperatur. Mehrere Regelsysteme wurden unter verschiedenen Rahmenbedingungen und Prozessanforderungen experimentell getestet. Eine erweiterte PID-Regelung mit geeigneten Vorsteuerungsschleifen zeigt sehr gute Resultate, zudem lässt sich die Gestaltung und Umsetzung des Regelsystems einfach halten.

Der zweite Teil der Arbeit widmet sich dem Regelsystem im solaren Direktverdampfungsbetrieb. Hierbei ist die Hauptregelgröße der benötigte Dampfdruck an der Prozessschnittstelle. Im Direktverdampfungsbetrieb wird die Anlage als Mehrgrößenregelsystem betrachtet. Zwei Regelkonzepte wurden mit der vorliegenden Arbeit entwickelt und getestet. Eines der Konzepte basiert auf einer erweiterten PID-Regelung mit Vorsteuerung. Dieses wurde erfolgreich umgesetzt und unter Realbedingungen über mehrere Jahre intensiv getestet. Das zweite Konzept stützt sich auf die Theorie der modellbasierten, Modellprädiktive Regelung (MPC). Hierbei handelt es sich um ein komplexes, entwicklungsintensives, Regelkonzept. Der wesentliche Vorteil ist die universelle Anwendbarkeit, mit reduziertem Aufwand für Implementierung, Bewirtschaftung und Inbetriebnahme.

Die vorliegende Thesis zeigt, dass sich trotz der komplexen Dynamik solarthermischer Grossanlagen mit den vorgeschlagenen Regelkonzepten

eine zuverlässige, robuste und wartungsarme Energieversorgung bewerk-
stelligen lässt.

Contents

Abbreviations

CSP Concentrated Solar Power.

DAE Differential Algebraic Equation.

DNI Direct Normal Irradiation.

DSG Direct Steam Generation.

FLH Full Load Hour.

HTF Heat Transfer Fluid.

IEA International Energy Agency.

IIR Infinite Impulse Response.

ISG Industrial Solar GmbH.

LFC Linear Fresnel Collector.

LTI Linear Time-Invariant.

MIMO Multiple Input Multiple Output.

MPC Model Predictive Control.

PID Proportional–Integral–Derivative.

POR Peak Overshoot Ratio.

PV Photovoltaic.

RMSE Root Mean Square Error.

SD Steam Drum.

SISO Single Input Single Output.

WMS Wire Mesh Sensor.

Nomenclature

A_{act} Active area of the solar field $[m^2]$. 17, 22

C_{abs} Overall thermal mass of the absorber tube $[kJ/K]$. 66

$C_{m,sd}$ Effective heat capacity of the steam drum metallic body $[kJ]$. 28

D_i Pipe internal diameter $[m]$. 82

E_{abs} Energy stored in the absorber tubes $[kW]$. 65

E_{sd} Energy storage capacity of the steam drum $[kJ]$. 28

$G(s)$ Plant transfer function in the s-domain. 7, 32

$G_c(s)$ Controller transfer function in the s-domain. 7

$H(s)$ Measurement system transfer function in the s-domain. 7

IAM Incidence Angle Modifier. 15, 16, 67

K_d Derivative gain of a PID controller. 111

K_i Integral gain of a PID controller. 111

K_p Proportional gain of a PID controller. 8, 93, 111

L_{sd} Liquid level in the steam drum $[\%]$. 4, 25

M_d Mass of fluid in the steam drum $[kg]$. 78, 79

M_r Mass of fluid in the absorber $[kg]$. 78, 79

M_{sd} Mass of steam in the steam drum $[kg]$. 73, 77

M_{sr} Mass of steam in the absorber $[kg]$. 74, 77

M_{wd} Mass of liquid water in the steam drum $[kg]$. 73, 77

M_{wr} Mass of liquid water in the absorber $[kg]$. 74, 77

O_{steam} Steam valve opening in percent of maximum $[\%]$. 4, 54, 118

T_{abs} Absorber mean temperature [^oC]. 18

T_a Ambient temperature [^oC]. 18

T_{fm} Mean fluid temperature [^oC]. 92

T_f Temperature of the feed water [^oC]. 25

T_i Solar field inlet temperature [^oC]. 22, 64, 66, 90, 99

T_{load} Load operating temperature [^oC]. 22

T_o Solar field outlet temperature [^oC]. 3, 4, 22, 31, 64, 66, 87, 88, 94, 99

T_r Setpoint temperature [^oC]. 90, 100

T_{sat} Saturation temperature [^oC]. 28

V_d Total volume of the steam drum [m^3]. 28

Φ Mass velocity or mass flux [$kg.s^{-1}.m^{-2}$]. 82

α Mass vapor quality. 62, 81, 82

α_d Mass vapor quality in steam drum. 78, 79

α_m Mean mass vapor quality in the absorber. 47, 76, 79

α_o Mass vapor quality in the absorber inlet. 76

α_r Mass vapor quality in the absorber outlet. 75, 76

α_s Absorptivity in the solar spectrum. 18

$\dot{Q}_f$ Net heat transfer to the fluid [kW]. 92, 93, 96, 99

$\dot{Q}_l$ Heat loss from the absorber [kW]. 17, 22, 25, 65, 66, 68, 79, 96

$\dot{Q}_{net}$ Net heat transfer across the absorber [kW]. 17, 66, 68, 74, 75, 79, 80, 92, 104

$\dot{Q}_{solar}$ Available solar power [kW]. 22, 25, 65, 66, 68, 79, 96

$\dot{m}_e$ Evaporation mass rate [kg/s]. 75

$\dot{m}_{fw}$ Feedwater mass flow [kg/s]. 4, 73, 79, 80

$\dot{m}_{rec}$ Recirculation mass flow through the solar field [kg/s]. 4, 22, 31, 54, 64, 66, 73, 75, 80, 87, 113

$\dot{m}_r$ Mass flow exiting the absorber and entering the steam drum [kg/s]. 25, 73, 79

$\dot{m}_s$ Steam mass flow to the load or the consumer steam network $[kg/s]$. 25, 54, 73, 79, 80, 118

$\dot{q}_l$ Thermal loss from the absorber to the environment through the metal wall per unit length $[kW/m]$. 18

ϵ_{IR} Emissivity in the infra-red spectrum. 18

η_{opt} Optical efficiency of the collector. 15, 17

γ Void fraction. 62, 84

$\hat{\eta}_{opt}$ Optical efficiency of the collector at normal incedince. 15

κ Plant dead time $[s]$. 65, 67, 68, 70, 88, 115, 116

$\mathbf{h}$ Model predictive control prediction horizon. 132

μ_f Dynamic viscosity of liquid $[Pa.s]$. 83

μ_g Dynamic viscosity of vapor $[Pa.s]$. 83

ω_{rec} Recirculation pump speed in percent of maximum $[\%]$. 4, 54

ϕ_c Collector azimuth angle $[degree]$. 15

ϕ_s Solar azimuth angle $[degree]$. 15

ρ_f Density of saturated liquid $[kg/m^3]$. 28, 82

ρ_g Density of saturated vapor $[kg/m^3]$. 82

σ Surface tension $[N/m]$. 83

τ Plant time contant $[s]$. 65, 66, 68–70, 87, 115, 116

τ_s Transmittance in the solar. 18

θ_l Incidence angle in the longitudinal plane $[degree]$. 15

θ_s Solar zenith angle $[degree]$. 15, 17

θ_t Incidence angle in transversal plane of the collector $[degree]$. 15

c_p Liquid water specific heat at contant pressure $[kJ/kg.K]$. 66

g Gravitational acceleration $[m/s^2]$. 82

h_f Specific enthalpy of saturated liquid $[kJ/kg]$. 28

h_g Specific enthalpy of saturated vapor $[kJ/kg]$. 73

h_{fg} Specific enthalpy of evaporation $[kJ/kg]$. 83

p System Pressure $[bar_g]$. 77, 79

p_r Pressure setpoint $[bar_g]$. 112, 113, 118

p_{load} Steam pressure at the load or consumer network $[bar_g]$. 4, 25, 28, 112, 113, 118

p_{max} Maximum operating pressure $[bar_g]$. 28

p_{sd} Steam drum pressure $[bar_g]$. 4, 54, 112

t Time $[s]$. 66, 92

t_d Derivative time of a PID controller $[s]$. 8, 93

t_i Integral time of a PID controller $[s]$. 8, 93

v_f Specific volume of saturated liquid $[m^3/kg]$. 47, 75

v_g Specific volume of saturated vapor $[m^3/kg]$. 47, 49, 74

w Fluid velocity $[m/s]$. 62

$P_{nominal}$ Nominal output power of the system $[kW]$. 28, 40, 42

Chapter 1

Introduction to the Control of Solar Thermal Plants

On 12.December 2015, 195 nations have signed a historic agreement in Paris to combat climate change [60]. The universal agreement's main aim is to keep the global temperature rise this century well below 2^oC and to drive efforts to limit the temperature increase even further to 1.5^oC above pre-industrial levels [60]. According to the agreement nations are required to reduce their greenhouse emissions as soon as possible to achieve the set temperature goal [60]. Being the chief contributor to greenhouse gases emissions, the energy sector should be the center of all efforts to achieve this ambitious undertaking.

According to the International Energy Agency (IEA), the 2040 outlook expects that 30% of our total energy consumption will be for industrial use [35]. A significant amount of this demand is for thermal energy.

Although this sector represents a major portion of our global energy consumption, it did not receive similar amount of attention given to other sectors like transportation, or that given to other energy forms like electricity.

Over the past years, the main focus in the renewable energy arena was finding ways to generate electricity using different technologies, whether it was wind, hydro, solar Photovoltaic (PV) or concentrated solar power. The main reason for this attention is that electricity is the most wisely used form of energy, and generating electricity means dealing with the energy problem from the source side and not having to deal with complexities of the consumer processes.

If we limit our discussion to industrial applications, designing and installing a solar PV system for a factory for example, is considerably a much easier process compared to designing and installing a solar steam generation system. In solar thermal systems, each system is custom made to fit customer requirements and normally demands several interfaces to oper-

ate properly. This added complexity of thermal systems is one of the main reasons that shifted attention to other renewable energy technologies.

This lack of attention to solar thermal technologies comes in spite of the fact that solar thermal systems provide several advantages in comparison to the main competitor, solar PV systems. Mainly the increased conversion efficiency of solar thermal systems compared to PV systems, which results in both reduced space usage for installations and potentially reduced investment costs. Secondly the ability to use cost effective storage solutions. This is important in light of the intermittent nature of renewable energy sources in general and solar energy in particular.

At present day, the vast majority of low and medium temperature thermal energy demand is provided through the combustion of fossil fuels, both an expensive venture and a threat to environmental stability. To combat the status quo and increase the share of solar derived thermal energy, the technical and socio-economic issues must be solved to provide end-users confidence in the technology. This can be promoted by mitigating the intermittent nature of solar resource and other disturbances that reduces availability.

The complicated nonlinear dynamics of a solar thermal plant require advanced control techniques in order to provide energy in a controlled, stable and reliable manner. This will largely help increase the acceptance of solar energy systems and stimulate their integration especially in industrial settings.

The main objective of the control system of a solar thermal plant is to compensate for temporal changes in energy supply, demand and performance variations of the conversion system. This results in a control problem which can be described as "nonlinear, time variant with pure time delays" [15].

Compared to a standard fossil-fueled heat source, which can be managed by controlling the combustion cycle to reach steady state conditions, a solar plant may never reach steady state, simply because of the ever changing sun position, solar irradiation and other disturbances.

Therefore, control stability is essential in the control of a solar thermal plant. Abrupt disturbances (e.g. from clouds) can cause undesirable/dangerous conditions where the plant would have to be shutdown wasting precious energy. This can also call for extra components like thermal inertia and buffer storages to meet the requirements of the process and therefore increasing investment costs [11] .

A stable control system can help minimize downtimes and enhance plant availability. This is especially relevant in an industrial settings where a stable, highly available source of heat at specific set-points is not only standard requirement but also taken for granted.

1.1 Problem Description and Objectives

This dissertation addresses the control problem of solar thermal systems for industrial process heat in the medium temperature range above 120^oC and below 400^oC. The main objective is to come up with a stable control system with good tracking, reliability and robustness at various operating conditions and with minimum operator intervention.

The subject of the study is a solar thermal Linear Fresnel Collector (LFC) plant designed for process heat applications. In this system, the solar collector field converts solar irradiation into heat that is passed onto the Heat Transfer Fluid (HTF). The HTF then transfers the useful energy to the consumer process.

Figure 1.1 depicts the hydraulic configuration of the LFC plant. The plant has two possible configurations, each of which has different control requirements. In configuration (a), the HTF is liquid water which remains all the time in liquid phase. This system is called single phase mode. The cold water exits the load and is pumped by the recirculation pump to the collector field inlet. The water heats up in the solar field as it passes through. The water exits the solar field with the temperature needed for the load.
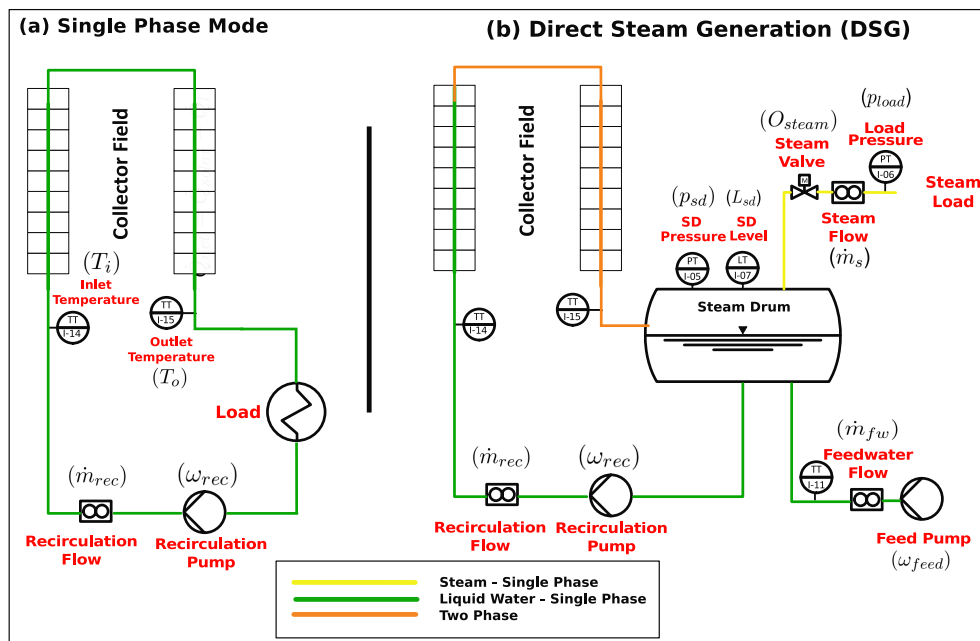
Figure 1.1: Overview of Single Phase and Direct Steam Generation Systems depicting important control parameters for each system.

The objective in this mode is to keep collector field outlet temperature (T_o) as close as possible to the setpoint. To do that, the controller adjusts

3

the recirculation mass flow rate ($\dot{m}_{rec}$).

In control terms, T_o is called the controlled variable and $\dot{m}_{rec}$ is called the manipulated parameter. All other variables and boundary conditions like solar irradiation or fluid inlet temperature are called system disturbances. (see Figure 1.2).
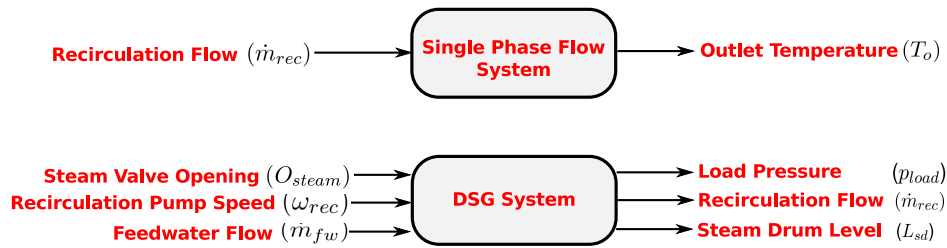
Figure 1.2: Summary of input and output variables for Single Phase and Direct Steam Generation Systems.

In configuration (b) of Figure 1.1, the system runs in Direct Steam Generation (DSG) mode. The recirculation pump pushes liquid water coming from the steam drum to the solar collector field. As the water heats up in the solar field part of it is evaporated, producing a two-phase flow. The flow continues towards the steam drum, where liquid water is separated from the steam. The produced steam is then passed to the consumer process through the steam valve at the required pressure (p_{load}). The feed pump makes up for the mass of fluid lost as the steam exits the system.

The DSG system consists of three control loops instead of one (see Figure 1.2). The first control loop is the one that regulates the mass of fluid inside the system. The controlled variable here is the steam drum liquid level (L_{sd}) and the manipulated parameter is the feedwater flow ($\dot{m}_{fw}$). The second controller regulates the recirculation mass flow rate ($\dot{m}_{rec}$) by manipulating the recirculation pump speed (ω_{rec}). The third and most important controller is the load pressure controller. This controller adjusts the steam valve opening (O_{steam}) in order to maintain the load pressure (p_{load}) at the required setpoint. The control of load pressure is the main objective in this configuration. In some configurations the controlled pressure is the steam drum pressure (p_{sd}).

The main objective of this research work is to develop a control system of LFC plant in both single phase and Direct Steam Generation (DSG) modes. The thesis addresses a topic rarely discussed in the literature available for solar thermal plants. Especially when it comes to plants designed for process heat applications and not power generation. In fact, the Ram-Pharma DSG system discussed in this work is perhaps the worlds first process heat, commercial, non-demonstration, LFC plant that is still in operation.

1.2 Methodology

In order to find the best control strategy for the system in its both configurations an iterative solution approach is adopted as depicted in Figure 1.3. First an initial model is developed, then a controller is designed based on the developed model, lastly system performance is experimentally tested to check if the proposed controller/model combination is adequate. The process is repeated several times until the required performance is achieved.

Other approaches found in the literature involve controller design based on simulation models. This requires the use of detailed models of the system which are not available.
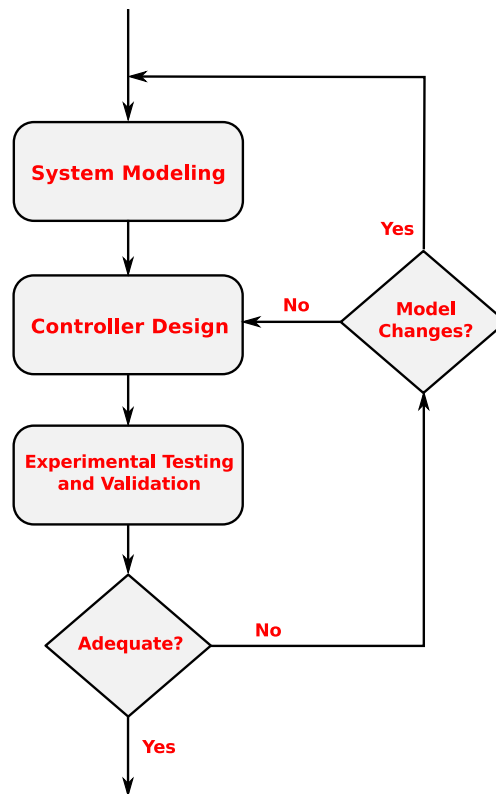
Figure 1.3: Iterative solution approach to finding the best control strategy for the solar thermal Linear Fresnel Collector (LFC) system. This approach is applied for both system configurations: single phase and DSG.

The control of the system in either of the two possible configurations in Figure 1.1 involves the control of non-linear systems with ever changing boundary conditions. Such systems are difficult to control using generic PID controllers.

Literature review on the topic reveals that advanced Model-based control methods (e.g. Feed-Forward Control or Model Predictive Control) are seen to enhance the performance of such systems significantly especially in response to measured disturbances and modeled dynamics. This implies developing accurate but yet simplified models of the controlled system. [14, 15]

Feed-forward control is a method to account for measured disturbances and include it in the control action before its effects appear on the output. This is typically done using a simplified model of the disturbance on the plant and suitable reaction to it. Typically Feed-forward is combined with classic PID controllers resulting in an enhanced overall controller.

In this work, several feed-forward models are used to enhance the performance of PID controllers used to control the system in both single phase flow and DSG modes.

The other control method used in this work is Model Predictive Control (MPC). MPC uses dynamic models based on fundamental mass and energy balances on the system which result in a robust control law. Run-time optimization of a suitable cost function is used to provide future control law based on current states and historical data. Model-based Control intrinsically corrects for dead time in the plant and also introduces feed forward control to compensate for measured disturbances [14]. MPC is used in this work to control the system in DSG mode.

In addition to the control strategies, two LFC plant models have been also developed. These models can be used to develop other control strategies or for simulation purposes. Moreover unique experimental measurements have been conducted on the plant in DSG mode to study several dynamic phenomena and flow patterns in the absorber tube. These experimental results are helpful for system designers and control engineers. Moreover, two-phase flow pattern maps for the LFC plant have been developed based on models in the literature.

1.3 Basics of process control systems

In order to understand complex systems, mathematical representation of the interactions between system inputs and outputs is needed [25]. A system of differential equations provides an adequate representation of system dynamics. When these equations are linearized, the Laplace transform can be used to simplify the solution [25]. Consider a system described by a second order differential equation as follows:

$$a\ddot{y}(t) + b\dot{y}(t) + cy(t) = r(t), \tag{1.1}$$

where a, b and c are constants, y is system output in the time domain, and r is system input in the time domain.

Assuming zero initial conditions, Equation 1.1 can be transformed into the frequency domain using the Laplace transform as follows:

$$as^2 Y(s) + bsY(s) + cY(s) = R(s), \tag{1.2}$$

where s is the Laplace variable.

Equation 1.2 can be rearranged in transfer function form as follows:

$$G(s) = \frac{Y(s)}{R(s)} = \frac{1}{as^2 + bs + c}, \tag{1.3}$$

where $G(s)$ is the transfer function.

The transfer function of a system or sub-system is defined as the ratio of the Laplace transform of the output variable to that of the input variable [25]. The transfer function derived in Equation 1.3 is called the plant or process transfer function. Similar transfer functions can be derived for other system parts, such as the controller for example.

1.3.1   Closed Loop Feedback Control System

The control system developed here is a closed-loop feedback control system. It consists of three main components (blocks) as seen in Figure 1.4. First, the process or plant block ($G(s)$) which represents the system to be controlled. Second, the controller block ($G_c(s)$), and lastly the sensor or measurement system block ($H(s)$).
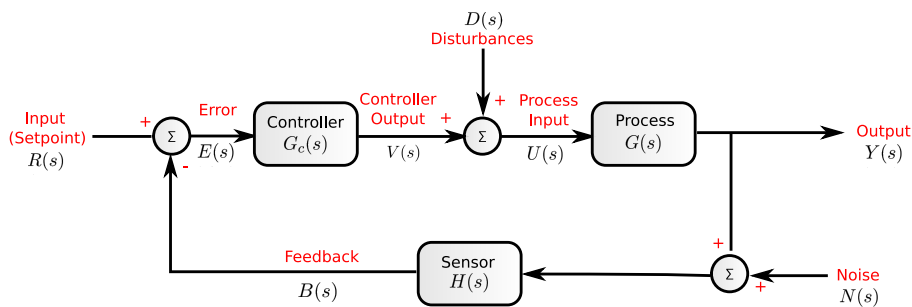
Figure 1.4: Block Diagram of a typical closed loop feedback control system.

1.3.2 The PID Controller

As seen in Figure 1.4, the controller uses the error[1] signal $E(s)$ to generate a correction action that is fed into the process.

PID controllers are controllers that provide a tunable combination of proportional, derivative and integral control action based on the error signal.

PID controllers are among the most widely spread controllers, in fact more than half of the industrial controllers utilize PID or modified PID schemes [51]. The advantage of PID control lies in the general applicability to most control systems. In particular when the model of the plant is unknown [51]. In the field of process control, it is well established that PID controllers provide adequate control although in many situations they might not provide optimal control [51].

The transfer function of a PID controller is given by:

$$G_c(s) = \frac{V(s)}{E(s)} = K_p\left(1 + \frac{1}{t_i s} + t_d s\right), \tag{1.4}$$

where K_p is the proportional gain, t_i is the integral time and t_d is the derivative time. Often t_i is replaced by the integral gain K_i, where $K_i = \frac{K_p}{t_i}$. And t_d is replaced by the derivative gain K_d, where $K_d = K_p t_d$.

1.3.3 Performance Evaluation of Control Strategies

The objective of any control strategy is to provide a stable operation, fast response, low overshoot and good setpoint tracking accuracy. These qualities can be quantified using several performance indicators. The acceptable range for each performance indicator is defined by application. Below is a list of the most common performance indicators.

- Rise time : which is the time needed by the controlled variable to rise from 10% to 90% of the setpoint value. This is a measure of response speed of the system.

- Settling time : which is the time needed by the controlled variable to remain within 5% of the setpoint value.

- Decay Ratio : is a measure of how quickly the system reduces oscillations, which is a measure of system stability. Figure 1.5 defines the decay ratio as the ratio C/B. A Decay Ratio of more than 1.0 means that the system is unstable.

---

[1]Notice that the word "error" is used as a control theory term and not as a statistical term (referred to as uncertainty). In control theory error refers to the deviation of the controlled parameter from the setpoint.
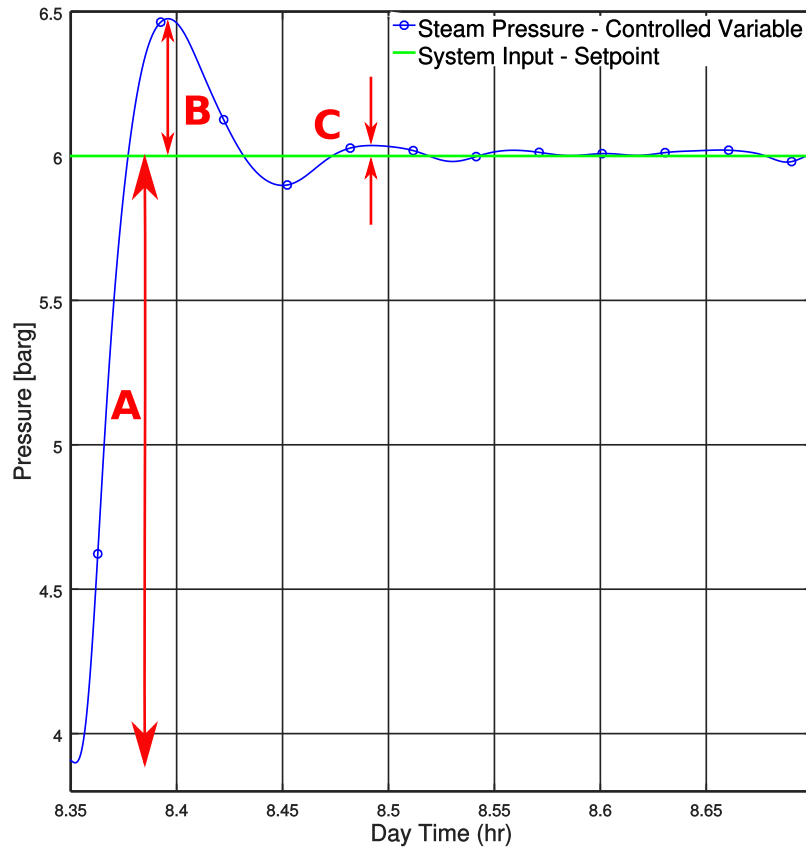
Figure 1.5: Performance evaluation of control systems.

- Peak overshoot : is a measure of how far does the controlled variable deviate from the setpoint after it crosses it for the first time. The Peak Overshoot Ratio (POR) is another measure for peak overshoot and is defined the ratio of B/A in Figure 1.5.

- Setpoint tracking (Error) : is a measure of how close does the controlled variable remain around the setpoint. This is defined as the root mean square error between the controlled variable and the setpoint.

$$RMSE = \sqrt{\frac{\Sigma e^2(k)}{n}}, \tag{1.5}$$

where RMSE is the root mean square error, $e(k)$ is the setpoint tracking error series, and n length of the series.

1.3.4   Overview of Time Scales for Different System Components

The system under study consists of several components with varying response times, from slow thermal processes with long time constants to very quick events like pressure shocks. Figure 1.6 provides an overview of the time scales for several system components and/or events in log scale.
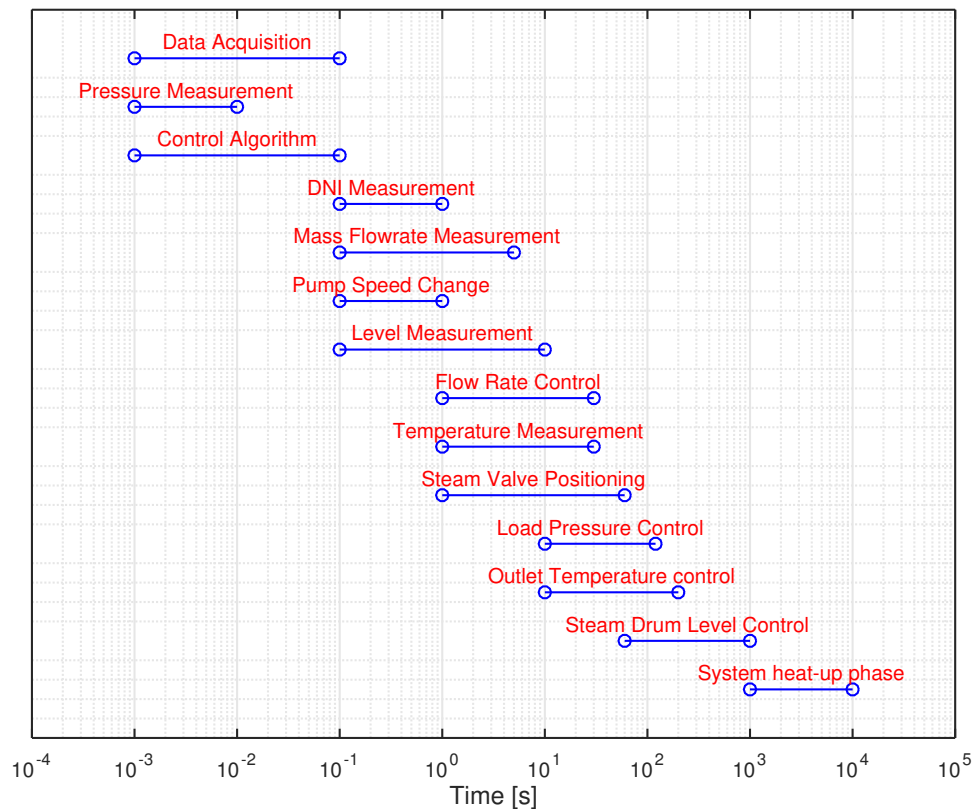
Figure 1.6: Overview of response time spread for several system components and/or events.

From the figure one can see that the control algorithm and the data acquisition system time scales are smaller than the time scale of the controlled processes, namely: Outlet temperature, load pressure, flow rate control and steam drum level control. Moreover all of the measurement systems have a smaller time scale compared to the corresponding controlled processes. This indicates that there are no controllability issues from time scales perspective.

1.4   Organization of the Thesis

The thesis deals with the control problem of solar thermal plants for process heat applications. This requires both theoretical modeling work in addition to experimental testing. The upcoming Chapter 2 presents the Linear Fresnel Collector plant, the subject of this study. First, fundamentals of Linear Fresnel Collectors are discussed, then single phase flow operation and two phase flow operation or DSG are introduced. Lastly a literature review of control strategies for both modes is presented.

Chapter 3 describes the experimental testing facilities used in this thesis. It discusses the hydraulic and instrumentation setup of both plants studied, the Hochdorf plant and the RamPharma plant.

The chapter also presents a detailed and unique experimental study of several phenomena observed during DSG operation. It also features results from the measurements done on two phase flow in the outlet of the solar field using a wire mesh sensor.

Chapter 4 is dedicated for physical modeling of the plant. The models developed in this chapter are later used in the development of the control strategies in both modes of operation. Moreover, flow pattern maps for the Linear Fresnel Collector plant are developed based on two phase flow models found in the literature.

Chapter 5 and chapter 6 present several control strategies developed for single phase flow and DSG modes, respectively. The chapters also present test results of the developed control strategies under varying operating conditions and in different test setups.

Chapter 2

Operation Principle of Linear Fresnel Collector Plant

2.1 Fundamentals of the Linear Fresnel Collector

The LFC converts concentrated solar irradiation into heat that is transferred to the Heat Transfer Fluid (HTF) that passes in the absorber tube. The LFC used in this work is manufactured by Industrial Solar GmbH (ISG) in Freiburg, Germany (see Figure 2.1)[37].

The collector consists of eleven mirror lines (primary mirrors) each of which tracks the sun individually and reflects solar irradiation towards an absorber tube. Each of the mirror lines is made of a slightly curved mirror section of $2.0m$ length and $0.5m$ width. These mirror sections are mounted next to each other on a single axis. The absorber tube is topped by a secondary reflector which is designed to reflect the solar irradiation that did not hit the absorber tube directly.

LFCs offer several advantages compared to other concentrating and non concentrating solar technologies [33, 31, 26]. These are mainly reflected in cost and the efficiency of land usage.

1. Low wind load.

2. Low weight.

3. High ground usage area.

4. Possibility of process integration at source level.

5. Stationary receiver.

6. Power adjustment using variable mirror combinations.
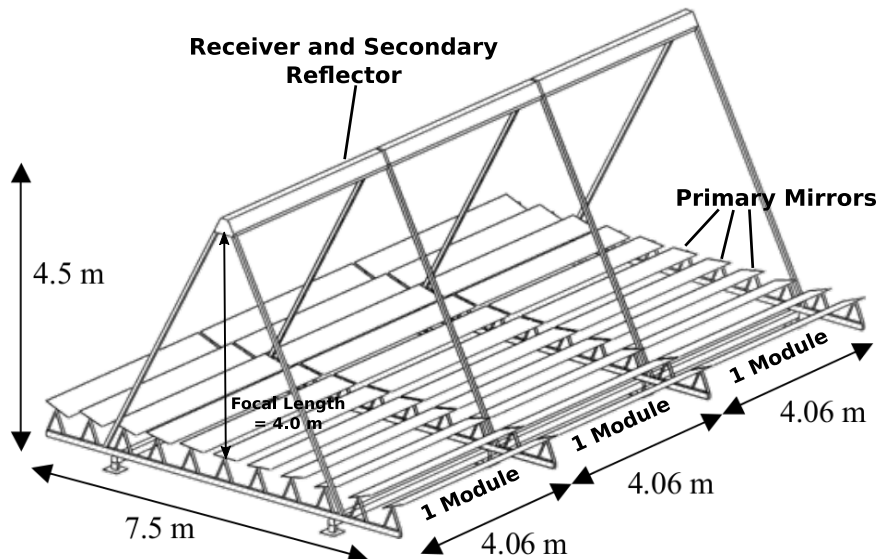
Figure 2.1: Geometric dimensions of the Linear Fresnel Collector of Industrial Solar GmbH. Adapted from [72]

In contrast to collectors used for power generation applications, this particular LFC is designed with industrial process heat and solar cooling applications in mind. The collector has been used in several commercial and demonstration projects all over the world including:

1. Solar cooling using absorption chillers [70, 72, 6].

2. Solar refrigeration [24, 8].

3. Solar drying using Direct Steam Generation for pharmaceutical applications [49, 30, 7].

4. Solar drying in the automobile industry [71, 36].

2.1.1   Optics of the Linear Fresnel Collector

The primary mirror field of the LFC traces the profile of a parabola that has its focal line at the absorber. Compared to a parabola however, the reflecting surface is arranged in one plane close to ground level. This results in a more compact design, increases land usage and decreases wind loads. [32, 72]

The LFC design also allows for a fixed absorber configuration in contrast with parabolic trough collectors. This simplifies the hydraulic connections and reduces cost. Moreover, since the absorber is fixed, it is always lit by the primary mirrors from the bottom and only a fraction of the irradiation hits

the absorber from above. This is an important characteristic for two phase operation.

In stratified two phase flow, steam is in the upper section of the absorber pipe and liquid water is in the bottom. If too much power is supplied to the upper section where the steam is situated, large temperature gradient will develop because of the low heat transfer rate through the steam compared to water. This gradient can result in an uneven thermal expansion of the absorber leading to damages in the absorber tube and its glass cover.

The optical efficiency of the LFC is a measure of how much of the available solar irradiation (Direct Normal Irradiation (DNI)) can be converted into thermal energy. There are many factors that degrade the optical efficiency of the collector, the main effects are summarized below.

1. Cosine loss: This is the loss that results from non-normal incident angles on the mirror surface. Due to non-normal incidence, the effective mirror area is reduced (see Figure 2.2 left) by a factor equal to the cosine of the angle between the incident solar irradiation and the mirror surface normal. It is worth noting that in reality, normal incidence can never be exploited. That is because even when the mirror surface would have made a normal angle with sun rays, at that time, the mirror will be shaded by the absorber!

2. Blocking and shading in the mirror field: Blocking loss occurs when one of the mirrors blocks reflected irradiation from reaching the absorber. Shading on the other hand, occurs when a mirror is shaded by a neighboring mirror. Shading and blocking losses are illustrated in Figure 2.2 (middle and right respectively).

3. Mirror reflectivity: Although high reflectivity mirrors are typically used, 100% reflectivity is hardly feasible. The ISG collector uses mirrors with a reflectivity of 93.5%. Mirror reflectivity is further degraded by soiling and dirt accumulation on mirror surface.

4. Effective absorption-transmission of the absorber tube: The optical efficiency is also affected by the transmittance of the glass envelope of the absorber tube and also the solar absorptivity of the coating.

5. End losses: The absorber tube extends along the primary mirror field, however due to changing sun position, the absorber is only fully lit when the relative azimuth angle between the sun and the collector is zero. Otherwise, the solar irradiation moves away from the absorber. That is why linear focusing collectors are typically built in long strings to reduce end losses.

6. Radiation spillage: Radiation spillage can occur in many places in the collector. For example, some of the radiation will not hit the ab-

sorber tube because it is reflected outside by the secondary reflector. Spillage can also occur because of non-perfect tracking or non perfect focal length of primary mirrors. This depends on the overall optical design.

7. Shading by the absorber: At high solar elevation angles, the absorber will shade a part of the mirror field. Some shading will also come from the structure of the collector.
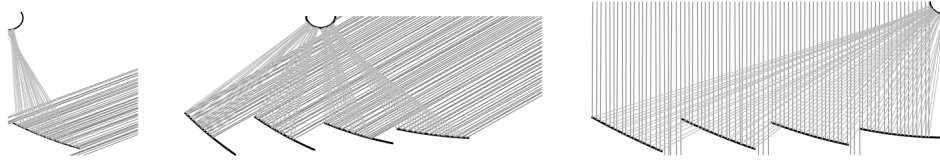
Figure 2.2: Optical Loss Mechanisms. Left: Cosine Loss. Middle: Shading. Right: Blocking. Adapted from [48]

In order to account for the aforementioned optical loss mechanisms and their variation with sun position, ray tracing techniques are employed to create an optical model of the collector. The model typically has the following form,

$$\eta_{opt} = \hat{\eta}_{opt} \, IAM(\theta_s, \phi_s - \phi_c), \tag{2.1}$$

where η_{opt} is the optical efficiency of the collector, $\hat{\eta}_{opt}$ is the optical efficiency of the collector at normal angle of incidence, which is evaluated by ray tracing to be $\hat{\eta}_{opt} = 0.63$, IAM is the incidence angle modifier function, θ_s is the solar zenith angle, ϕ_s is the solar azimuth angle and ϕ_c is the collector azimuth angle. (see Figure 2.3).

In Equation 2.1, the IAM function modifies the optical efficiency of the collector based on the relative sun position. Because of its unique design, the Fresnel collector IAM consists actually of two IAM functions, one in the transversal plane related to the transversal angle of incidence (θ_t), and the other in the longitudinal plane related to the longitudinal angle of incidence (θ_l), these planes are defined in Figure 2.3. Therefore, Equation 2.1 can be rewritten as follows:

$$\eta_{opt} = \hat{\eta}_{opt} \, IAM_t(\theta_t) \, IAM_l(\theta_l), \tag{2.2}$$

where IAM_t is the incidence angle modifier in transversal plane and IAM_l is the incidence angle modifier in the longitudinal plane.

The IAM functions are calculated using ray-tracing methods. Figure 2.4 depicts the longitudinal IAM for several collector lengths. A single curve for the transversal plane is shown as it is collector length independent. It can be seen in the figure that the transversal IAM rises above unity. This
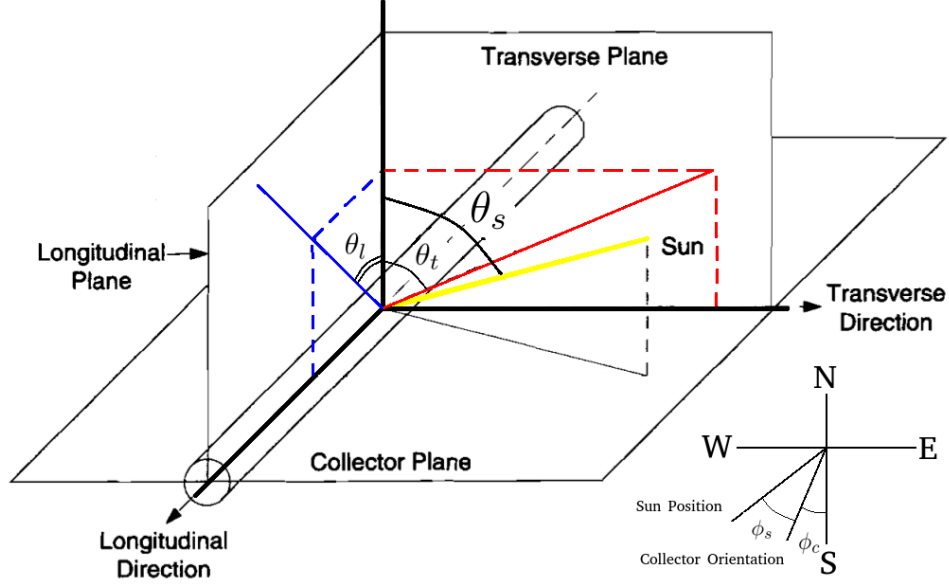
Figure 2.3: Planes of the incidence angle modifiers for the Fresnel collector. Courtesy of [26].

is explained by less blocking at higher angles of incidence. It is also evident from the figure that longer collector strings have better (higher) longitudinal IAM which can be explained mainly by the relative reduction of end losses.

Since IAM functions are hard to implement on an industrial controller as look-up tables, fifth order polynomials are fitted to the IAM data which is available from the manufacturer's datasheet [37]:

$$IAM_l(\theta_l) =$$
$$2.3018 \times 10^{-9}\theta_l{}^5 - 4.2245 \times 10^{-7}\theta_l{}^4 + 2.4445 \times 10^{-5}\theta_l{}^3 \quad (2.3)$$
$$- 5.6779 \times 10^{-4}\theta_l{}^2 - 9,4714 \times 10^{-4}\theta_l + 0.9068,$$

$$IAM_t(\theta_t) =$$
$$1.9671 \times 10^{-9}\theta_t{}^5 - 3.8696 \times 10^{-7}\theta_t{}^4 + 2.3740 \times 10^{-5}\theta_t{}^3 \quad (2.4)$$
$$- 6.0818 \times 10^{-4}\theta_t{}^2 + 5.3207 \times 10^{-3}\theta_t + 1.0102.$$

2.1.2 Linear Fresnel Collector Thermal Models

The mirrors of the LFC concentrate solar irradiation on the absorber tube. The amount of power reaching the absorber is given by Equation 2.5:

$$\dot{Q}_{solar} = \eta_{opt} A_{act} \; DNI \; cos(\theta_s), \qquad (2.5)$$
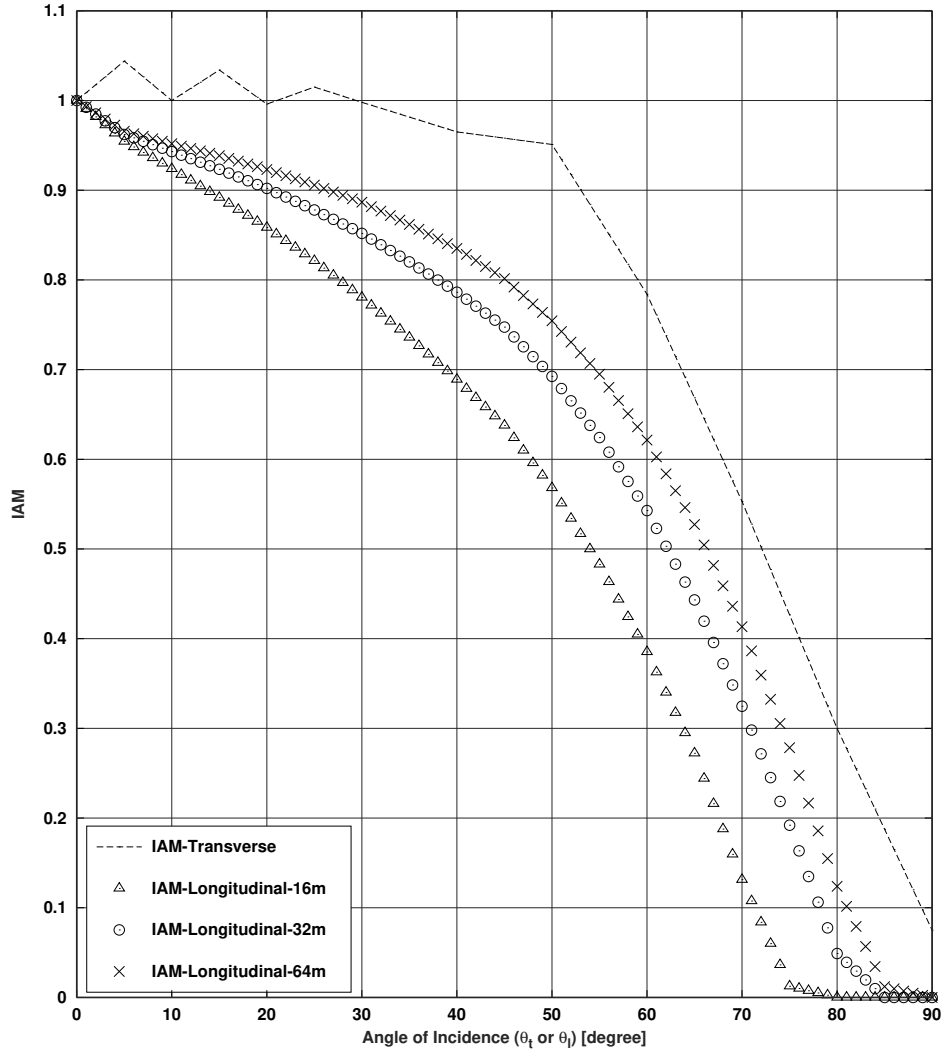
Figure 2.4: Calculated incidence angle modifiers as a function of incidence angle for several collector lengths.

where η_{opt} is the optical efficiency of the collector, A_{act} is the active area of the primary mirrors (m^2), θ_s is the solar zenith angle, DNI is the solar Direct Normal Irradiation (kW/m^2).

The total power reaching the HTF in the absorber is called $\dot{Q}_{net}$ and is given by:

$$\dot{Q}_{net} = \dot{Q}_{solar} - \dot{Q}_l, \tag{2.6}$$

where $\dot{Q}_l$ is the total heat loss from the absorber.

The absorber tube is mounted $4.0m$ above the primary mirror field, which is $4.5m$ from ground level depending on the installation.

The absorber tube is a vacuum tube produced by Schott Solar. In the collectors discussed here the $PTR70$ model is used. This absorber has a $70mm$ outer diameter and a standard length of $4.06m$. The absorber tube consists of a stainless steel pipe which is covered by a selective coating that has high absorption in the solar spectrum ($\alpha_s = 0.95$) and low emission in the infrared spectrum ($\epsilon_{IR} = 0.14 \ at \ 380^oC$). The selective coating greatly reduces radiative losses. The high vacuum maintained by the glass cover around the stainless steel pipe almost eliminates convective heat loss from the absorber tube. The glass cover has an average solar transmittance of $\tau_s = 0.96$.

Due to the complex optical and thermal interactions within the absorber tube, its hard and unpractical to develop analytical models for thermal losses from the absorber. Hence, typically experimental data is fit to polynomial functions of absorber operating temperature.

There are two generations of Schott's $PTR70$ in use. The older version is used in the testing facility in Hochdorf, while the newer one, which has better thermal efficiency, is used in all installations after that. The new generation was tested by both NREL (National Renewable Energy Laboratory) [13] and DLR (German Aerospace Centre) [52]. The resulting fourth order polynomial correlations of heat loss are depicted in Figure 2.5.

The DLR correlation is adapted to be based on the temperature difference between ambient temperature and absorber temperature as follows:

$$\dot{q}_l = 0.18102(T_{abs} - T_a) + 8.1609 \times 10^{-9} \ (T_{abs} - T_a)^4, \qquad (2.7)$$

where $\dot{q}_l$ is the heat loss from the absorber per unit length in $[W/m]$, T_{abs} is the absorber mean temperature in $[^oC]$ and, T_a is the ambient temperature $[^oC]$.

The NREL correlation was derived for constant ambient temperature between 23^oC and 25^oC as follows:

$$\dot{q}_l = 0.141T_{abs} + 6.48 \times 10^{-9} \ T_{abs}^4. \qquad (2.8)$$

Although the correlations are a bit different, they are very close in the region of interest which extends only until 200.0^oC as shown in Figure 2.5.

The correlation used for old generation absorbers is given by the second order polynomial:

$$\dot{q}_l = 2.341 \times 10^{-3} \ T_{abs}^2. \qquad (2.9)$$

Table 2.1 summarizes the heat loss coefficients of the absorber to evaluate the total heat loss in watt per meter of absorber length. The coefficients are substituted in a polynomial fit equation as follows:

$$\dot{q}_l = a_0 T_{abs} + a_1 T_{abs}^2 + a_2 T_{abs}^3 + a_3 T_{abs}^4. \qquad (2.10)$$
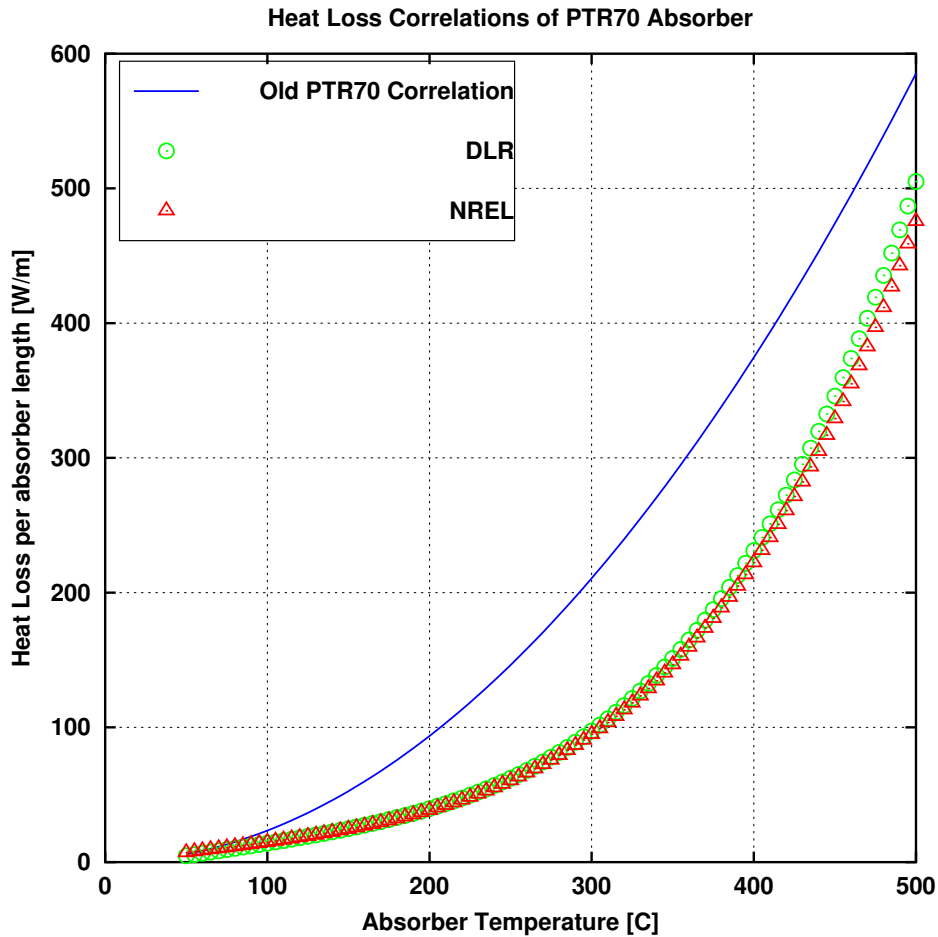
Figure 2.5: Evaluated heat loss correlation of the PTR70 absorber tube as a function of absorber temperature.

2.1.3   Heat Transfer Fluid

The Heat Transfer Fluid (HTF) used in the Fresnel Collector is application dependent. Typically either water or thermal oil are used as the heat transfer fluid in the solar field. When the HTF is compressed water (i.e liquid water) the water is maintained under a pressure which is higher than the saturation pressure of the required temperature. In this case the maximum reachable temperature is restricted by the maximum pressure that the absorber can withstand, which is $120bar$. This corresponds to 330^oC water.

Slightly higher temperature can be archived at a much lower pressure when using thermal oil. Using thermal oil, the collector can reach up to 380^oC. In this case the restriction is actually the stability of the synthetic oil at such high temperature.

Table 2.1: Summary of heat loss coefficients of the PTR70 Schott absorber, in $[W/m]$ **of absorber length**

Correlation	a_0	a_1	a_2	a_3
DLR	0.18102	0	0	8.1609×10^{-9}
NREL	0.141	0	0	6.48×10^{-9}
Old Version absorbers	0	2.34×10^{-3}	0	0

The other option, which is very common in industrial settings, is to use saturated steam as the HTF. Saturated steam is a very popular heat carrier in industrial environments. This is mainly because of the high energy density of steam (latent heat) which translates practically to smaller pipes and cheaper infrastructure.

The LFC is usually integrated into the heat production system as the primary heat source. A secondary heat source is normally present as a backup. The produced heat of the LFC is delivered to the consumer processes through the HTF. The type of the HTF determines the hydraulic configuration and complexity of the overall system. System configurations can be broadly categorized based on the HTF phases present in the solar field.

2.2 Single Phase Flow Systems

In single phase flow systems, the HTF remains liquid during the heating process in the solar field. Figure 2.6 depicts a simplified system configuration. The main pump circulates the fluid in the solar field where it heats up gradually. The HTF mass flow rate in the solar field is adjusted according to the required outlet temperature and the available solar energy. When the HTF exits the solar field it passes through the load, where heat is extracted. The HTF can either directly supply energy to the load or it could charge a thermal storage. After passing through the load the HTF cycles back to the solar field where it collects heat again. During this cycle the heat transfer fluid remains in the same phase. This is accomplished by maintaining system pressure above the saturation pressure of the fluid at the operating temperature.

2.2.1 Control of Single Phase Flow Systems

Temperature control is of prime importance in most solar thermal systems. Most thermal processes operate optimally at a certain temperature range; hence it is essential to keep the collector outlet temperature within

$$\dot{Q}_{net} = \dot{Q}_{solar} - \dot{Q}_l$$
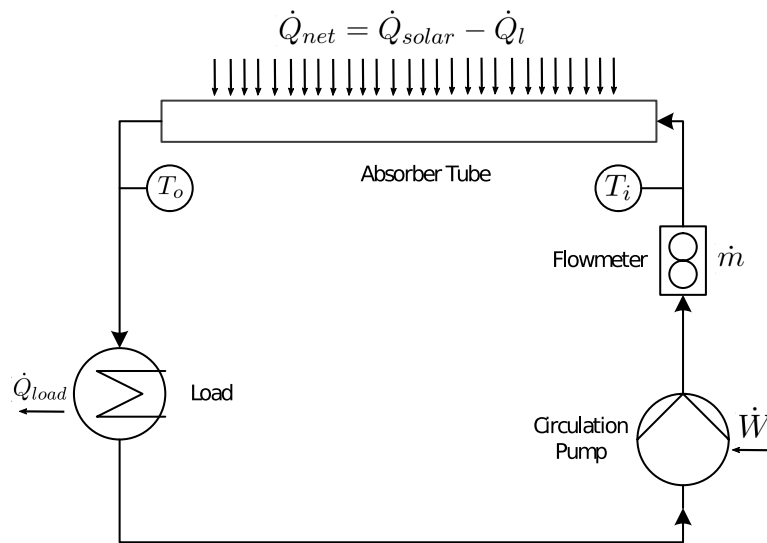
Figure 2.6: Overview of typical single phase flow configuration

the limits of the process. Failing to do so, will result in sub-optimal operation conditions, and in extreme cases, cause damage to some components in case of overheating for example.

Absorption cooling for example, requires a certain temperature to regenerate the solution (180^oC for double effect absorption chillers), under part load operation, the heat input can be reduced but the temperature should be maintained to maintain evaporation.

Industrial processes are most efficient in continuous operation [47]. To achieve this, the solar system should provide a constant supply of energy at the required temperature regardless of disturbances or load variations.

Providing a reliable and accurate temperature control increases the availability of solar systems even at low irradiation levels, this reduces demands on the auxiliary heat sources and saves on equipment costs such as buffer storages. This also keeps the solar field ready avoiding unnecessary shutdown and startup of the process and thereby increasing efficiency and saving operation time. Good control will also allow driving the process close to design limits hence improving productivity. [47]

The main task of the temperature controller, is first to maintain the collector operation in the safe region and second to maintain outlet temperature as stable and as close to the setpoint as possible. In other words provide good stability and tracking performance.

The temperature controller is also supposed to work under varying conditions of solar irradiation, mirror reflectivity, sun position, inlet conditions, flow rates and demand levels.

The controllability of the outlet temperature of the collector is dependent on the heat load variation, heat storage and thermal capacity of the system. If the collector output and the heat load profiles do not match, a sufficient thermal storage should be used or a hybridization with another system becomes necessary to maintain the required temperature.

The control of the solar collector outlet temperature can be described as "nonlinear, time variant with pure time delays" [15]. Because of this, conventional PID control methods result in oscillatory operation and fail to bring the control parameter to stability, especially when the operation conditions change from where they have been tuned at. [16]

From control point of view, in a single phase flow system, the controlled variables can be one or more of the following:

- Solar field outlet temperature (T_o).

- Load operating temperature (T_{load}).

The manipulated parameters are:

- HTF mass flow rate ($\dot{m}_{rec}$).

- Active area of the solar field (A_{act}).

Main system disturbances are:

- Solar field inlet temperature (T_i).

- Available solar power which depends on solar irradiation, sun position ($\dot{Q}_{solar}$).

- Thermal losses of the solar field ($\dot{Q}_l$).

- Soiling of the reflective and glass surfaces.

2.3   Two Phase flow and DSG Systems

In a two phase flow system, two phases of the HTF coexist in the system. Water is the most popular choice, where its evaporated to produce steam for process heat or to feed a steam turbine. When water is evaporated directly in the absorbers of the solar field instead of producing steam using a steam generator, the system is then called a Direct Steam Generation System or DSG.

The system depicted in Figure 2.7 is a DSG system that runs in parallel with a fossil fired steam boiler. In the morning, when solar irradiation is available, the recirculation pump starts pumping liquid water from the steam drum to the solar field inlet. The temperature starts to rise in the absorbers when the mirrors are focused. As the temperature rises above the

saturation temperature, steam generation starts, converting the flow into a two-phase flow.

The two-phase mixture coming out of the solar field is fed into the steam drum. In the steam drum the two phases are separated into liquid and gas. As the steam generation continues in the solar field, the pressure in the system starts to rise. When the pressure in the steam drum (p_{sd}) reaches a value higher than the load pressure (p_{load}), steam can be delivered.
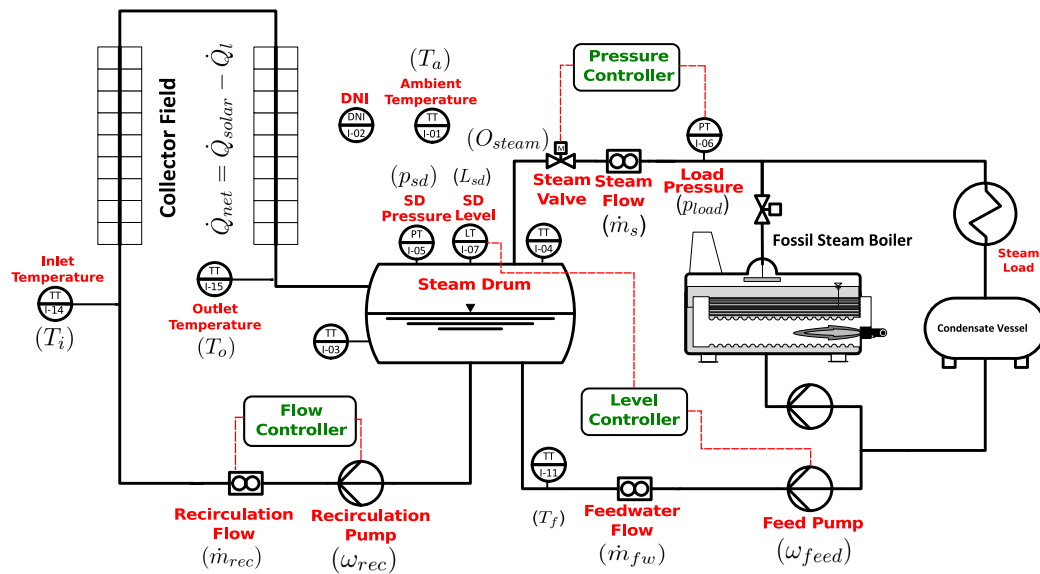
Figure 2.7: Simplified piping and instrumentation diagram of a solar DSG system in recirculation mode. Main PID controllers are also depicted.

Steam feeding to the load network is controlled by the steam valve opening (O_{steam}). The steam valve controls the pressure in the load steam network by manipulating the amount of steam being fed into the network. Meanwhile, as steam is being delivered, make-up liquid water is pumped into the steam drum to maintain the overall water mass within the operation limits.

If the load consumes less steam than is being generated, the steam drum pressure will rise until it reaches the maximum operation pressure. After that the solar field mirrors are moved out of focus to prevent further pressure increase. On the other hand, if the load consumes more pressure than the solar field can generate, the pressure in the steam drum will start dropping until it falls below the load pressure. At that point the backup boiler will start and will compensate for the missing power. This happens every day as the sun starts declining.

When there is no enough solar energy available, the mirrors will be turned out of focus, the pump is kept running for a while to ensure that

no steam is left in the solar field. This is called the flooding procedure. When the flooding procedure is finished the pump is turned off, and the system remains pressurized ready for next day of operation. This is called the Standby state.

2.3.1 DSG System Advantages

DSG has been suggested for solar power plants in order to reduce the number of components of the solar plants and hence bring costs down.

Most commercial solar power plants are operated with synthetic oil or molten salt as the heat transfer fluid (HTF) in the solar field, which is then used in a steam generator to produce steam needed to operate the steam turbine. This configuration is simple from controls point of view and does not involve two-phase flow complications as in (DSG).

In spite of the complications that DSG technology present, several economical and technical advantages offered through DSG encouraged research and investigation in this field. DSG advantages can be summarized in the following main points [73]:

- Avoiding environmental risks associated with synthetic oil usage, like soil contamination for example [1].

- Higher temperature limit compared to oil.

- Simpler overall plant configuration.

- Lower investment and operation and maintenance costs.

2.3.2 Control of DSG Systems

Looking at the DSG plant from controls point of view, it is a more complicated control problem than single phase flow systems. The increased number of inputs and outputs makes DSG more complicated to control. Whereas single phase solar system can be described as a Single Input Single Output (SISO) problem, the DSG plant is a Multiple Input Multiple Output (MIMO) problem.

Moreover, DSG systems are characterized by unique properties due to the two phase flow present in the solar field. The presence of gas-liquid mixtures results in a dynamic system much more sensitive to disturbances in comparison with single phase systems.

Figure 2.7 depicts a typical configuration of a DSG using PID controllers. The controlled parameters of the plant are

- Load steam network pressure (p_{load})

- Steam drum liquid level (L_{sd})

- Recirculation mass flow rate ($\dot{m}_r$)

The manipulated parameters are:

- Recirculation pump speed.

- Feed pump speed.

- Steam Valve opening.

Main system disturbances are:

- Feedwater temperature (T_f).

- Steam mass flow (steam demand) ($\dot{m}_s$).

- Flow pattern in the absorber tubes in the solar field.

- Available solar power which depends on solar irradiation, sun position ($\dot{Q}_{solar}$).

- Thermal losses of the solar field ($\dot{Q}_l$).

- Soiling of the reflective and glass surfaces.

Although there are many similarities between DSG systems for solar power plants and those of smaller size process heat applications, some differences can be still recognized, for example:

- For solar power plants, the power range is often above the $10MW$ mark. This means that the flows involved in the solar field are typically bigger which has a stabilizing effect on the two phase dynamics of the system.

- The pressure levels encountered in industrial process heat systems hardly exceed the $20bar$ level in most cases compared to the power plant range which is often around $120bar$. Lower pressure levels makes the systems easier to handle and cheaper to build. But on the other hand, at lower pressure levels liquid and vapor properties deviate from those at higher pressures. Furthermore water properties at pressure ranges below $20bar$ change in a nonlinear fashion.

- Typically for industrial process heat, saturated steam is needed and not superheated steam. This simplifies the solar system by removing the superheater sections, which typically suffer from controllability issues.

- A solar power plant will typically run at a varying supply (solar resource), but on a more controllable and stable demand. This is not the case for industrial process heat where changes in supply and demand are often the case.

2.3.3   DSG System Components

The Boiler

The solar field acts as a boiler in the DSG system. This solar boiler can be used in hybrid operation with a conventional fossil (or other) heat source as shown in Figure 2.7. The solar field consists of several modules of the linear Fresnel collector LF-11 depicted in Figure 2.1. The modules are arranged in a line to form a long string, then several strings are arranged adjacent to each other in parallel.

The solar field can be thought of as a steam boiler that extends over hundreds of square meters of ground area and can reach kilometers in pipe lengths. In this very large heat exchanger, liquid water enters at one end and gets heated and partially evaporated exiting as a two phase flow mixture at the other end.

During operation, the solar field can be virtually divided into two sections, the preheating section, where the mixture of feedwater and recirculation water is heated up to the saturation temperature. In this section the flow is single phase. The second section is the evaporation section where the liquid starts to boil and the two phase flow starts developing. The location of the interface between the two sections is not constant and it shifts continuously based on operation conditions. The most relevant parameters for that affect operation are solar irradiation disturbances, sun position, flow rate and inlet conditions.

Steam Drum (SD)

The steam drum (steam accumulator, steam buffer, or Ruths storage) is a key component of the recirculation DSG concept. The steam drum performs four main functions in the system, (i) buffer storage, (ii) pressure maintenance system, (iii) phase separation and (iv) Water reservoir. Because of its large thermal mass, it plays a significant role in shaping the dynamic response of the whole system, which makes it of primary interest in control and modeling.

1. **Buffer Storage Function**

   Renewable energy systems suffer from the intermittent nature of energy supply. The steam drum helps in mitigating this problem by providing a buffer against these transients. Since the storage of steam directly is not economically feasible due to its high specific volume, energy is stored as sensible heat in the pressurized saturated liquid and the metallic parts of the steam drum.

   A great advantage of this concept is that the storage media and the working fluid can be the same, which allows for high discharge rates

26

[62].

When steam is needed, the pressure is reduced resulting in flash steam. The produced steam attains the evaporation energy from the liquid sensible heat and the drum body. As the pressure reduces, the steam drum will settle at a reduced saturation temperature and pressure.

The steam drum is considered fully charged when the pressure reaches its maximum and is completely drained when the pressure reaches the load pressure setpoint.

Therefore, reducing the load pressure setpoint, or increasing the maximum operating pressure will increase the storage capacity.

One of the main disadvantages of this storage concept is that the whole system would have to operate at higher pressure than actually required by the process to have any significant storage.

The storage capacity of the steam drum can be calculated by the following simplified formula:

$$
\begin{aligned}
E_{sd} = & \\
& C_{m,sd}[T_{sat}(p_{max}) - T_{sat}(p_{load})] + \\
& \rho_f(p_{max})L_{sd}|_{p_{max}}V_d[h_f(p_{max}) - h_f(p_{load})],
\end{aligned}
\tag{2.11}
$$

where E_{sd} is the storage capacity of the steam drum, $C_{m,sd}$ is the effective heat capacity of the steam drum metallic body, T_{sat} is the saturation temperature at a given pressure, p_{max} is the maximum operating pressure, p_{load} is the setpoint pressure of the load or the steam network, ρ_f is the density of saturated liquid, V_d is the total volume of the steam drum, $L_{sd}|_{p_{max}}$ is the ratio of liquid to the total volume of the steam drum evaluated at p_{max}, h_f is the enthalpy of saturated liquid at a given pressure. Since the mass of saturated steam present at the top of the steam drum is negligible, the enthalpy of saturated steam does not appear in the formula.

Notice that here it is assumed that the mass of liquid inside the steam drum does not change between the two states at p_{max} and p_{load} which is a simplifying assumption. The level ratio will change however and that is why indicating the pressure at which level is evaluated is important. It is also assumed that the enthalpy of steam in the steam drum is negligible compared to the enthalpy of liquid water.

From Equation 2.11 one can infer the important parameters that affect the storage capacity. One often neglected parameter is the liquid fill level of the steam drum which should be maximized to increase storage capacity.

The storage capacity of the steam drum in (Full Load Hour (FLH)) can be calculated using the following formula:

$$FLH = \frac{E_{sd}}{3600 \times P_{nominal}} \tag{2.12}$$

where FLH is the full load hours of the storage, which are the number of hours that the storage can provide nominal power to the load, $P_{nominal}$ is the nominal power of the system.

According to Steinmann et al. [62], such buffer storages are characterized with short reaction time and high discharge rates. Typical capacities being around 5 to 10 full load minutes.

In a typical process heat installation, a buffer between 0.25 FLH and 0.50 FLH is used. 8.0% of which is actually stored in the body of the steam drum. The load pressure is normally in the range of $6.0bar$ and $10.0bar$ and the maximum pressure is $16.0bar$. In this range this storage concept is actually most effective since the change in liquid enthalpy with pressure is the highest in the range up to $20bar$, which can be seen in Figure 2.8.

2. **Phase Separation Function**

The recirculation concept requires a separator for removing the liquid from the two phase mix. The steam drum is partially filled with liquid water and the upper void is occupied by saturated steam. As the two phase flow, enters the steam drum from the side, the steam will stay on top while water drops to the liquid pool because of its higher density. This is further enhanced by metal sheets that reduce the momentum of water droplets carried by the steam forcing them to settle in the liquid pool.

To prevent any liquid carry over with the steam leaving to the consumer network, the steam drum level is maintained below a safe limit.

In some systems the two phase flow is actually fed from the bottom of the steam drum through the liquid. This has the disadvantage of generating liquid level oscillations, and increasing the swell/shrink effect as more vapor is present under the liquid level. However, it does have the advantage of ensuring uniform heating of the liquid pool.

3. **Pressure Maintenance Function**

Any fixed volume hydraulic system which encounters temperature variations needs a means to compensate for volume changes if the used fluid is incompressible. Compressed liquid systems would require a dedicated system for compensating volume changes which are typically in the form of diaphragm vessels or pressure controlled
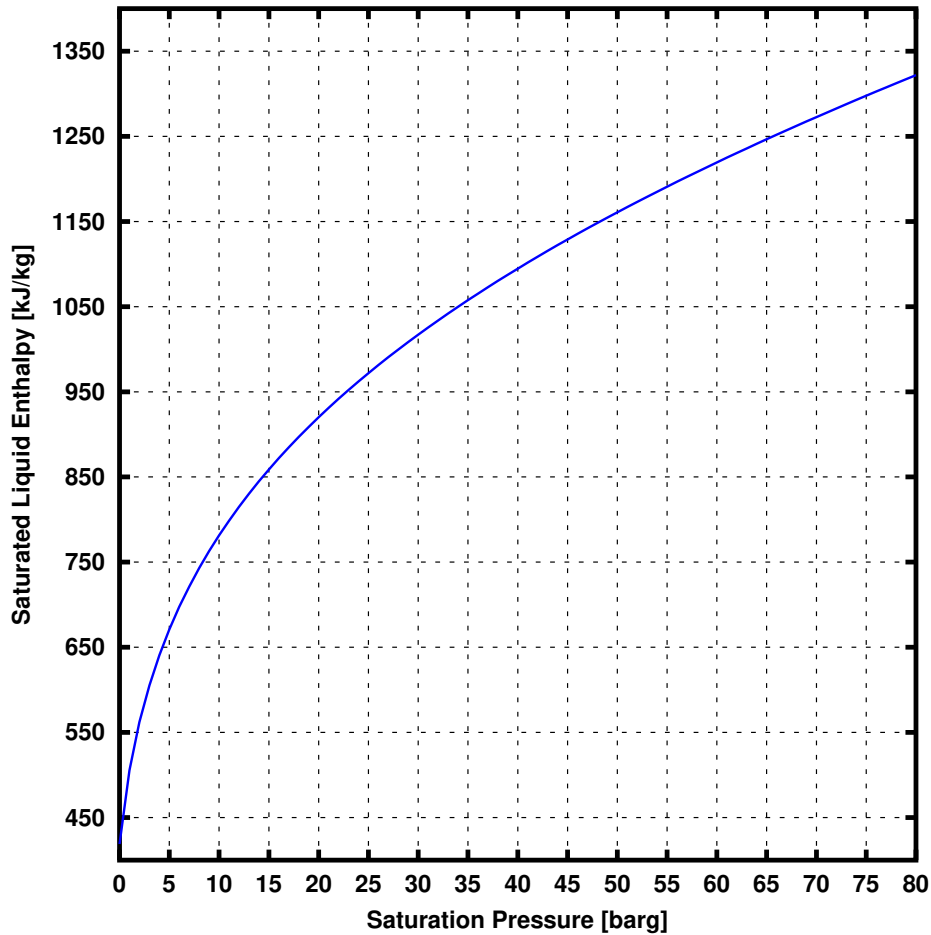
Figure 2.8: Enthalpy of saturated liquid water at different saturation pressures based on IAPWS-IF97.

pump stations. In this DSG system, the compressibility of the steam in the upper part of the steam drum is exploited to provide the needed compensation for changes in the liquid volume. Hence a dedicated pressure maintenance system is avoided.

4. **Water Reservoir Function**

An often overlooked problem is the fact that the solar system has to be shut down and started every day. In the absence of the heating source, all the two phase flow sections will be filled with liquid water. This extra water, which is needed to fill the void left by the condensing steam in those sections, is provided by the steam drum. This can be a significant amount of water accounting for 10% of steam drum total volume. Typically, the steam drum is the only place where the two

phases co-exist after a shutdown.

Steam Valve

The steam valve is a key component in the solar DSG system. The steam valve regulates the pressure on the load side. This requires the steam valve to continuously change its opening to follow the changes in the steam demand and also the changes in the steam supply in order to maintain the set pressure.

The steam valve is also considered a safety component; since the solar system often operates at a higher pressure level than the user pressure level. It is important that the steam valve is able to react fast if the pressure exceeds safety levels. This is normally achieved by either using a fast acting pneumatic valve or using an emergency close feature which is available for electric valves.

Recirculation Pump

The recirculation pump is used to provide continuous flow in the solar field by recirculating the liquid part of the two phase flow after it is separated. The recirculation pump will provide more liquid mass flow than can be evaporated to prevent any overheating in the solar field. The recirculation pump should also have enough head to face the changes in pressure drop across the solar field when the two phase dynamics change.

Feed Pump

The feed pump main task is to replace the mass of steam that is being provided to the user network. Ideally the feed pump mass flow should match the mass of steam leaving the system. The feed pump is characterized as a high head pump since it needs to raise the feed water pressure from almost $0.5bar$ up to $20.0bar$. Here the type of pump needed can vary depending on the system design parameters. Practically achieving high head at low flows is not easily possible. Hence, the choice depends on system size, where multistage pumps are suitable for bigger systems and positive displacement pumps are more well suited for smaller ones. Vane pump can also be used but are typically more expensive.

2.4 Review of Control Strategies of Solar Thermal Plants

2.4.1 Literature Review of Control Strategies for Single Phase Flow

The controlled parameter of single phase flow systems is the outlet temperature of the solar field (T_o). This parameter has a non linear relationship with the mass flow rate ($\dot{m}_{rec}$). It is well established in the literature that conventional PID controllers fail to provide adequate control for such problems. Therefore, research in the field is focused on finding advanced control techniques to control the outlet temperature of the solar field.

In 1996, Meaburn and Hughes [47] presented a predictive controller for the control of large scale parabolic trough collectors. The authors argued that control schemes using fixed or adaptive PI parameters are unsuitable since the process has resonance dynamics at low frequency tending to restrict the bandwidth of the controllers. Hence they devised a simple transfer function representation of the process as seen in Equation 2.13:

$$G(s) = \frac{k_0}{s(1 + s\tau_m)} \left(1 - \frac{e^{-s\tau_d}}{1 + s\tau_1} \right), \tag{2.13}$$

where $G(s)$ is the transfer function of the plant, s is the independent variable in the frequency domain, τ_1 is a variable time constant of the system, τ_m is a time constant to compensate for measurement system lag, τ_d is the time delay and k_0 is a static gain.

The model in Equation 2.13 was then used to develop the predictive controller, which consisted of a parallel compensator similar to a Smith Predictor [69].

The resulting transfer function parameters were identified experimentally. Since a simplified model was used, the resulting controller was easy to implement and computationally efficient. The performance of the controller was demonstrated on the ACUREX parabolic trough collector field in Plataforma Solar de Almeria (PSA) in Spain.[47]

In 1997, Camacho, Berenguel and Rubio published a book dedicated for the problem of temperature control of solar plants in single-phase operation [15]. Most of the control techniques presented were also tested on the ACUREX field in PSA in Spain. The authors also presented two dynamic models of the solar field which were used for both control and simulation purposes. The control methods discussed ranged from simple control methods to advanced ones like robust control, adaptive control, model-based control and artificial intelligence control methods. Later in 2013, applied on the same ACUREX plant, Andrade et al. [2] presented a Non-Linear Model Predictive Control (NMPC) strategy which they used to

control the outlet temperature of oil. The strategy suggested does not need
model parameter identification or adaption.

Cirre et al. [19] presented a model-based feedback linearization control
technique. The control law takes into account the transport delay by using a
numerical approximation. The linearization is achieved by a nonlinear map-
ping between a linear controller and the required flow rate. The mapping
explicitly included the effect of disturbances mainly coming from changes
in solar irradiation and inlet temperature.

In 2007, Camacho et al. [16, 17] presented a two part extensive survey
of automatic control techniques used to control the outlet temperature of
solar plants. The survey discussed several control methods including PID
control, Feed forward control, robust control, adaptive control, gain schedul-
ing, neural networks, fuzzy logic, model-based predictive control, time delay
compensation, optimal control and nonlinear control [16, 17]. The authors
argued that because of the nonlinear effects in the solar plant, fixed param-
eter PID controllers won't be able to cope with the control problem. Hence
they have to be tuned with low gains producing sluggish responses. Other-
wise, tightly tuning them will result in high oscillations when the dynamics
of the process vary. The authors did not recommend a certain control tech-
nique, however, they suggested that the "ideal" controller should be high-
order and nonlinear, keeping in mind the trade-off between commissioning
time and performance [17].

In this thesis, model based feed forward control is used in combination
with a PID controller to control the Linear Fresnel Collector plant designed
for process heat applications. It is shown that several models can be used
with feed forward control depending on the operation conditions and the
available instrumentation. This makes the suggested control strategy us-
able for different applications. Using experimental data, it is shown that very
accurate control of outlet temperature can be achieved using the suggested
control strategy.

Alternative control methods are also suggested for different applications
including solar field power manipulation which is a unique feature of the
Linear Fresnel Collector studied in this work.

2.4.2 Literature Review of Control Strategies for DSG

There are a few solar thermal plants currently operating using the DSG
concept around the world [5]. And there are much fewer (if any other than
the one presented here at all) that are designed for process heat applica-
tions. Most DSG plants, are built for power generation and not process heat
applications. Aurousseau et al. [5] presented an extensive review of DSG
control strategies for different configurations designed for power generation.
A more recent review of DSG systems using linear solar concentration is
presented by Bittencourt de Sá et al. [22].

There are several possible hydraulic configurations for DSG systems. Three of them were mostly investigated by workers in the field, namely: Once-Through, Recirculation and Injection concepts. See Figure 2.9.

In the once through concept, water is fed into the solar field from one end and exits as superheated steam at the other end in one pass only, hence the name. This concept is the least complex from hydraulic design view point and requires the least investment cost. However the dangers associated with thermo-mechanical stresses in the superheater section [28] and the questionable controllability of this concept, challenge its development.[73, 28, 74, 66]

In the Injection concept, water is injected at several points along the absorber tube to control the temperature of the superheated steam and prevent overheating. This concept has a relatively increased cost and complexity level. [73, 28, 74, 66]

In Recirculation mode, more water than can be evaporated is circulated through the solar field. The exit of the solar field is hence a water-vapor mixture. The water is recirculated again with feedwater and the steam is either used as saturated steam or then superheated after separation. Compared to the Once-Through concept, the recirculation concept is less complex and is more controllable, however the extra cost incurred by the additional recirculation pump and the steam separator is a clear cost disadvantage [66].
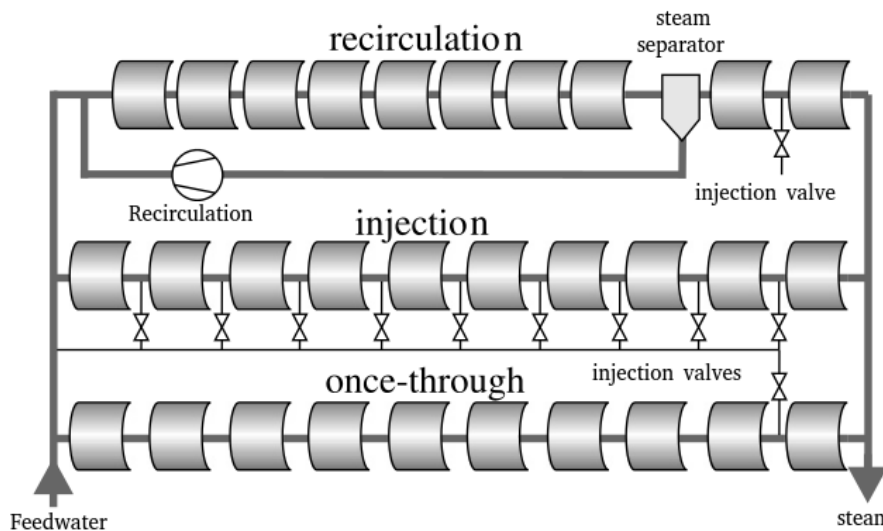
Figure 2.9: Flow arrangement of three different direct steam generation concepts. Adapted from [27].

The DIrect Solar Steam (DIIS) project was a research and development project aimed at developing solar systems for direct steam generation using parabolic trough collectors [73]. Within the DIIS project, PID controllers

are used in the control of the recirculation mode. Linearized transfer functions of the process were used to tune controller parameters using pole-placement techniques, followed by further final optimizations. Performance data showed good results for the controllers in maintaining static steam conditions at the exit, however unfortunately the published data was only for relatively clear days with no strong changes in solar irradiation [28].

In 2005-2006 more detailed data was published for the control concepts of both recirculation and once through concepts using PID controllers and feed-forward techniques [66, 67]. According to the authors, the PI control structure used in the recirculation mode was adequate to maintain stable operating conditions. This was not the case for the once through concept where a more complex control method using feed-forward and cascade control had to be used.

In the recirculation mode the DISS plant control consisted of five main PID-based controllers. A recirculation flow controller which is used to maintain the recirculation flow, a feed pump controller which is used to maintain a certain pressure drop across the feed valve, a steam separator level controller which controls the feed valve, a steam temperature controller using water injection, and finally a steam pressure controller using a steam exit control valve. For the tuning process of the controllers, the step response data of the different controllers were fit on first-order with dead time models and then the tuning parameters were found using the process reaction method. [66]

In comparison, the system studied in this work uses three controllers only. A recirculation flow controller, a feed water flow controller and a steam pressure controller. Moreover, feed water flow is controlled using feed pump manipulation and not using a control valve.

The published results in [67] described the operation and control of the system at different pressure and temperature setpoints. It was clear from the results that the changes in input parameters (i.e solar irradiation and inlet conditions) affected system performance. Although the system showed overall stability, this came at the cost of conservatively tuned PID controllers with long settling times [67].

Valenzuela et al. suggested that future development of the control theory should target more advanced control methods like MPC to achieve better dynamic performance in terms of settling time, overshoot and setpoint tracking.[67]

In 2007 Eck and Hirsch [27] described the dynamics and controls of direct steam generation for parabolic trough plants in recirculation mode. Simulations were conducted to assess system response to variations in feedwater mass flow and solar irradiation [27].

Authors also described a unique problem related to DSG systems related to irradiation disturbances. During low irradiation periods, liquid water starts to accumulate in the absorber as steam production drops. When

solar irradiation is restored to its original state, steam production is also restored and liquid which accumulated in the absorber is then blown out causing a high water flow at the absorber outlet. [27]

Depending on the location in the solar field where irradiation disturbance occurs (e.g. due to small cloud that partially shade the solar field), the situation can be escalated. If the shading occurs in the beginning of the evaporation section, saturated steam starts to condense in this section, the void left by condensing steam is filled with liquid water coming from upstream and hence results in reduced water reaching the downstream sections [27]. As irradiation is restored water is blown out with high velocity as evaporation starts almost immediately, while the downstream sections might overheat during that time.

The overheating of the absorber sections in the absence of liquid water to remove the heat is of course to be avoided at all costs, if the heating of the absorbers continue while there is no enough cooling, the circumferential temperature difference can become high resulting in a deflection of the absorber tubes and eventually damage the glass envelope. The effect of temperature gradients in the absorbers was perhaps first experienced by Almanza et al. during their experiments with parabolic trough collectors for DSG [1].

Regarding the control of the feedwater, Eck and Hirsch suggested basing the control on steam production rather than steam separator liquid level. This is because PI controllers of liquid level would have to be de-tuned for stability resulting in sluggish and unsatisfactory performance. Alternatively, a PI controller on steam production is used with some sort of gain scheduling. [27]

Data for the performance of the suggested controller however does not show the changes in steam pressure against disturbances and only shows changes in the level of the steam separator.

In 2017, Guo et al. [29] presented a nonlinear dynamic model for a parabolic trough DSG plant operating in the recirculation mode. The model is used in the development of a multi-model switching generalized predictive control scheme. The authors reported that proposed control strategy offers robust and safe operation over a wide range of operating conditions.

Unlike the aforementioned studies The focus of this thesis will be on DSG systems for process heat applications which means that the system operates in significantly lower pressures (around $20bar$) unlike the aforementioned systems which operate at much higher pressures exceeding $100bar$. This means that although the control concepts are similar, different outcomes are expected. Differences between DSG systems designed for process heat applications and those designed for power generation are discussed in Section 2.3.2.

The first control strategy developed is based on PID controllers with feed forward control. Test results from the testing facility in addition to oper-

ational data from a commercial system are presented to illustrate the performance of the control strategy.

The second control strategy is based on Model Predictive Control, which provides a universal control law of the system including all of its inputs and outputs. Test results of the control strategy in the testing facility in Hochdorf are also presented in this work.

The available literature on DSG systems misses a study of the unique dynamic phenomena that occur during operation. Therefore a detailed discussion of several phenomena are presented for the first time. This is supported by experimental data from real life situations. This data can be used by other researchers to aid in the design process of DSG systems and their control strategies. The data is especially helpful when detailed simulation models are not available for the designing engineers.

Chapter 3

Description and Experimental Identification of the Test Plants

3.1 Plants Setup and Instrumentation

The work in this thesis has been developed, tested and implemented in several plants around the world. While most of the development and testing was conducted in the company testing facility in Freiburg-Hochdorf, many of the results come from other installations. Figure 3.1 presents the plants in which the control system has been implemented and/or developed.

Plant Name	Location	Type	Operating Mode	HTF
Hochdorf	Germany	Testing Facility	DSG / Single Phase	Water
Duerr	Germany	Drying	Single Phase	Water
Umkirch	Germany	Solar Cooling	Single Phase	Water
Fischer	Germany	Solar Cooling/Heating	Single Phase	Water
QSTP	Qatar	Research	Single Phase	Water
MTN	SouthAfrica	Solar Cooling	Single Phase	Water
RamPharma	Jordan	Process Heat	DSG	Water
JTI	Jordan	Process Heat	DSG	Water

Figure 3.1: A list of the plants where the control system, described in this thesis, has been implemented and/or developed.

The two main plants where most of the development and testing work has been done are Hochdorf and RamPharma. In the Hochdorf plant (Figure 3.2) most of the initial testing and research was done. The plant is able to run in both single phase and Direct Steam Generation (DSG) modes. The RamPharma plant (Figure 3.3) represents the first commercial plant in which the DSG control system developed here was implemented. Hence, the data acquired from the plant's operation during first year was very valuable for further development of the control system.

Figure 3.2: Hochdorf testing facility near Freiburg, Germany.

Figure 3.3: RamPharma DSG plant near Amman, Jordan.

3.1.1 Hochdorf Plant

The Hochdorf plant was constructed in 2005. The plant is located in the industrial area of Hochdorf near Freiburg in Germany. The plant serves as a testing facility for the linear Fresnel collector and has ever since been used in many funded research projects to test and develop new technology related to concentrated solar thermal energy.

The plant consists of a six module Fresnel collector (see Figure 2.1) with a total area of primary mirrors of $132m^2$ and a maximum output power of $73.0kW_{th}$. Figure 3.4 depicts a simplified piping and instrumentation diagram of the plant. The operator can switch the plant to operate either in single phase mode or in DSG mode using the 3-way diverting valve shown in the figure. Notice that some details are omitted from the piping and instrumentation diagram for simplicity.
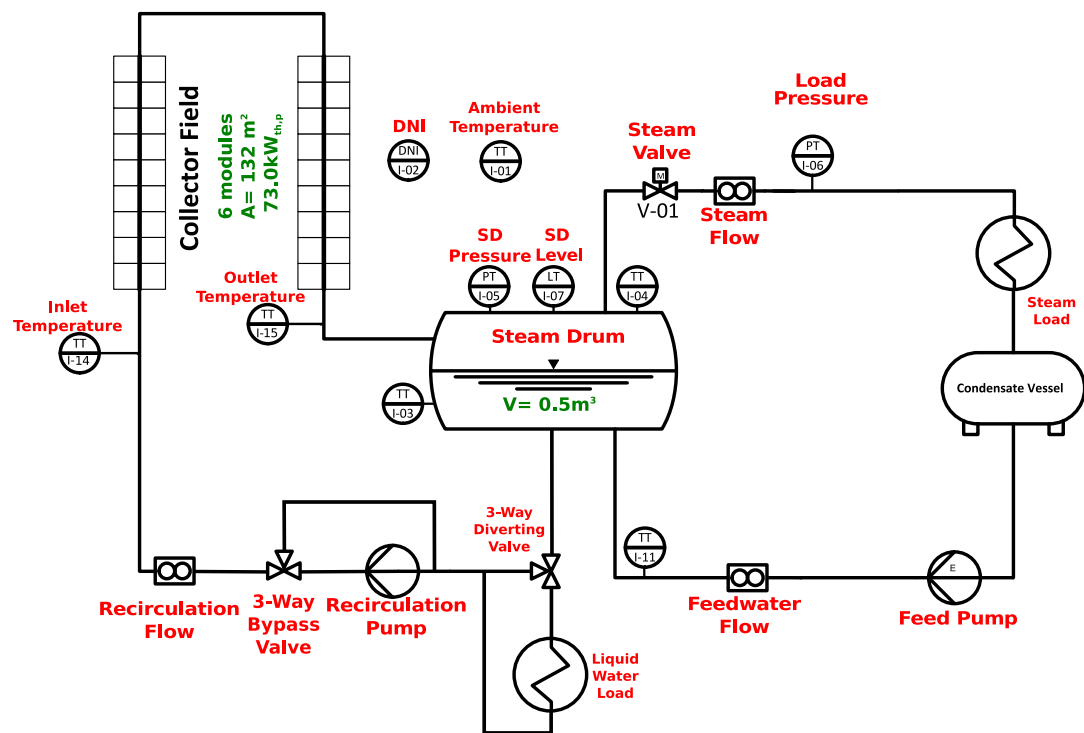
Figure 3.4: Simplified piping and instrumentation diagram of the testing facility in Hochdorf, Germany.

Table 3.1 provides full plant specifications. The main sensors used for measurements and control in the plant are summarized in Table 3.2 along side with their measurement ranges and accuracy.

Table 3.1: Hochdorf plant specifications

Item	Value
Nominal output power ($P_{nominal}$)	$73.0kW_{th}$
Total area of tracking mirrors	$132.0m^2$
Maximum operating temperature	204.0^oC
Maximum operating Pressure	$16.0bar_g$ $(1.6MPa)$
Nominal recirculation mass flow (DSG)	$0.30kg/s$
Nominal recirculation mass flow (single phase mode)	$1.0kg/s$
Nominal steam drum level (DSG)	50%
Nominal load steam pressure (DSG)	$10.0bar_g$ $(1.0MPa)$
Nominal load steam mass flow (DSG)	$100.0kg/h$
Nominal feed water mass flow (DSG)	$100.0kg/h$

Table 3.2: Hochdorf plant instrumentation

Sensor	Range	Accuracy	Type
Outlet temperature	$-50^oC..250^oC$	$\pm0.15^oC$	Class A Pt-100
Inlet temperature	$-50^oC..250^oC$	$\pm0.15^oC$	Class A Pt-100
Ambient temperature	$-50^oC..250^oC$	$\pm0.3^oC$	Class B Pt-100
Recirculation volume flow rate	$0l/s..2.5l/s$	$\pm0.25\%$	Magnetic-Inductive
Steam mass flow rate	$0kg/h..600kg/h$	$\pm12kg/h$	Target (Force on plate)
Feedwater mass flow rate	$0kg/h..150kg/h$	n/a	Orifice (test sensor)
Steam drum liquid level	$0mm..700mm$	$\pm3mm$	Guided Radar
Steam drum pressure	$0..16bar(1.6MPa)$	$\pm0.16bar$	Gauge Pressure
Load steam pressure	$0..25bar(2.5MPa)$	$\pm0.25bar$	Gauge Pressure
DNI	$0W/m^2..1400W/m^2$	$\pm14W/m^2$	Pyrheliometer Alone
DNI	$0W/m^2..1400W/m^2$	$\pm50W/m^2$	Pyrheliometer plus Tracker

3.1.2   RamPharma Plant

The RamPharma plant was constructed in 2014 and was commissioned in March 2015 [49]. The plant is located in King Abdullah II industrial near Amman, Jordan. The plant is constructed to supply saturated steam to the Ram Pharmaceuticals factory. The steam delivered by the solar system is fed into the existing steam network of the customer which is then used in the manufacturing process. [49, 9, 44]

The plant consists of an 18 module Fresnel collector (see Figure 2.1) with a total area of primary mirrors of $396m^2$ and a maximum output power of $222.0kW_{th}$. Figure 3.5 depicts a simplified piping and instrumentation diagram of the plant. The system runs automatically in hybrid operation with the existing steam boiler. The control system is designed to ensure full automatic operation without operator intervention. Table 3.3 provides the plant specifications.
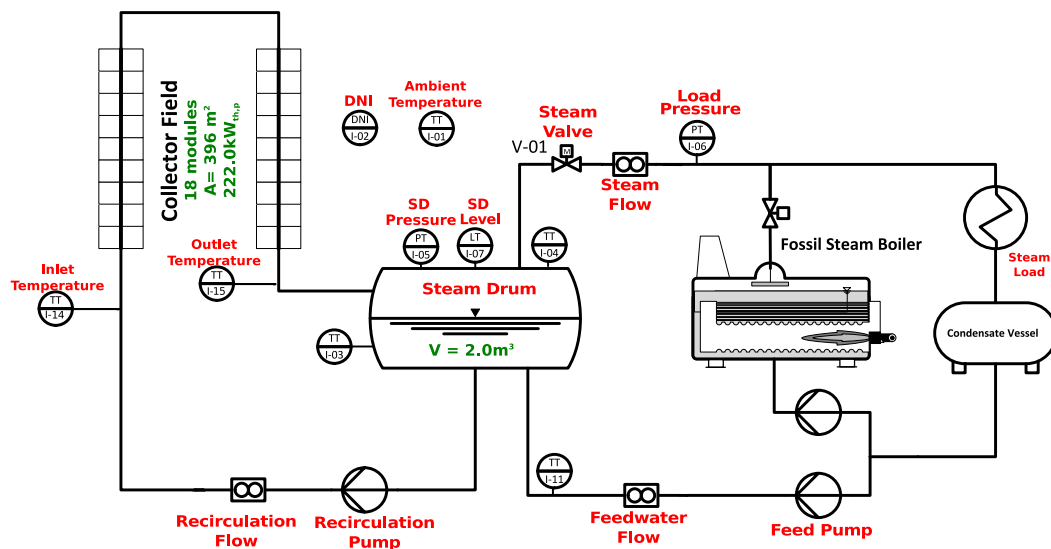
Figure 3.5: Simplified piping and instrumentation diagram DSG plant designed to provide process steam for the RamPharma pharmaceuticals factory near Amman, Jordan.

The main sensors used for measurements and control in the plant are summarized in Table 3.4 along side with their measurement ranges and accuracy.

Table 3.3: RamPharma plant specifications

Item	Value
Nominal output power ($P_{nominal}$)	$222.0kW_{th}$
Total area of tracking mirrors	$396.0m^2$
Maximum operating temperature	204.0^oC
Maximum operating Pressure	$16.0bar_g(1.6MPa)$
Nominal recirculation mass flow (DSG)	$2.0kg/s$
Nominal steam drum level (DSG)	70%
Nominal load steam pressure (DSG)	$6.0bar_g(0.6MPa)$
Nominal load steam mass flow (DSG)	$300.0kg/h$
Nominal feed water mass flow (DSG)	$300.0kg/h$

Table 3.4: Ram plant instrumentation

Sensor	Range	Accuracy	Type
Outlet temperature	$-50^oC..250^oC$	$\pm0.15^oC$	Class A Pt-100
Inlet temperature	$-50^oC..250^oC$	$\pm0.15^oC$	Class A Pt-100
Ambient temperature	$-50^oC..250^oC$	$\pm0.15^oC$	Class A Pt-100
Recirculation volume flow rate	$0l/s..2.5l/s$	$\pm0.25\%$	Magnetic-Inductive
Steam mass flow rate	$0kg/h..1000kg/h$	$\pm20kg/h$	Target (Force on plate)
Feedwater mass flow rate	$0kg/h..3250kg/h$	$\pm0.2\%$	Magnetic-Inductive
Steam drum liquid level	$0mm..1400mm$	$\pm3mm$	Guided Radar
Steam drum pressure	$0..16bar$ (1.6MPa)	$\pm0.04bar$	Gauge Pressure
Load steam pressure	$0..16bar$ (1.6MPa)	$\pm0.08bar$	Gauge Pressure
DNI	$0W/m^2..1250W/m^2$	$\pm15\%$	Shadow pattern pyranometer

3.2   Phenomena Observed in DSG Operation

The control system development started by an extensive experimental campaign in summer of 2014 aiming at studying the unique dynamics of the two phase flow system. These experiments became the backbone for control system development later on.

DSG systems rarely operate in steady state. They are characterized by the ever changing dynamics. Several special transient behaviors and non-linearities of DSG systems are described and studied based on experimental data. Control remedies for these unique dynamics are proposed and used in the development of the controller.

The experimental study presented here, gives a detailed insight into solar steam systems that is not readily available in the literature. This helps researchers in the field better understand DSG systems and design suitable controllers.

3.2.1 Nonlinearity of Load Pressure Control

The steam valve (see Figure 2.7) is used to maintain the pressure on the load side (downstream) at a specified setpoint. Under normal operation conditions, when the steam drum pressure is higher than the load pressure, the pressure controller reacts normally and regulates the pressure on load side. As the steam drum pressure drops approaching the load side pressure, the pressure controller increases valve opening to maintain the steam flow to the load. This is only possible up to the point where the steam drum pressure equals the load side pressure.

At this point, the valve is fully open and should now completely close to avoid any back flow of steam from the load side when the backup boiler is turned on.

This nonlinear action of jumping from completely open to completely closed cannot be handled by a basic PID controller and should be handled separately as an exception rule.

The exception rule should close the valve before the steam drum pressure drops below either the load pressure setpoint or the measured load side pressure. The exception rule should also prevent the controller from opening the valve again after it has been shut with an exception. The valve should only be opened when the steam drum pressure rises above both the load side pressure and its setpoint.

3.2.2 Overheating and Dry-outs Caused by Reduced DNI

Irradiation induced dry-outs can be dramatic, especially for large collector fields. If the collector field is shaded during steam production, saturated steam will start to condense. The void left by the steam will then have to be filled with the water coming upstream. This results in much less water reaching the downstream section of the absorber. At this time, if irradiation is restored downstream section is likely to overheat. Moreover the condensed water will be blown out with high velocity as the evaporation starts almost immediately. [27]

Figure 3.6 depicts several situations, where the temperature measured by the outlet temperature sensor indicated a temperature higher than the saturation temperature. As illustrated in Figure 3.8, this shows that the liquid level has dropped at the collector outlet supporting the hypothesis.

3.2.3 Stratified and Low Flow Causing Overheating

If the flow rate through the absorber is low enough, the liquid and gas phases stratify inside the absorber. The higher density liquid phase settles in the bottom and the gas phase goes on top. Compared to parabolic trough collectors the absorber receives heat from below, which is where
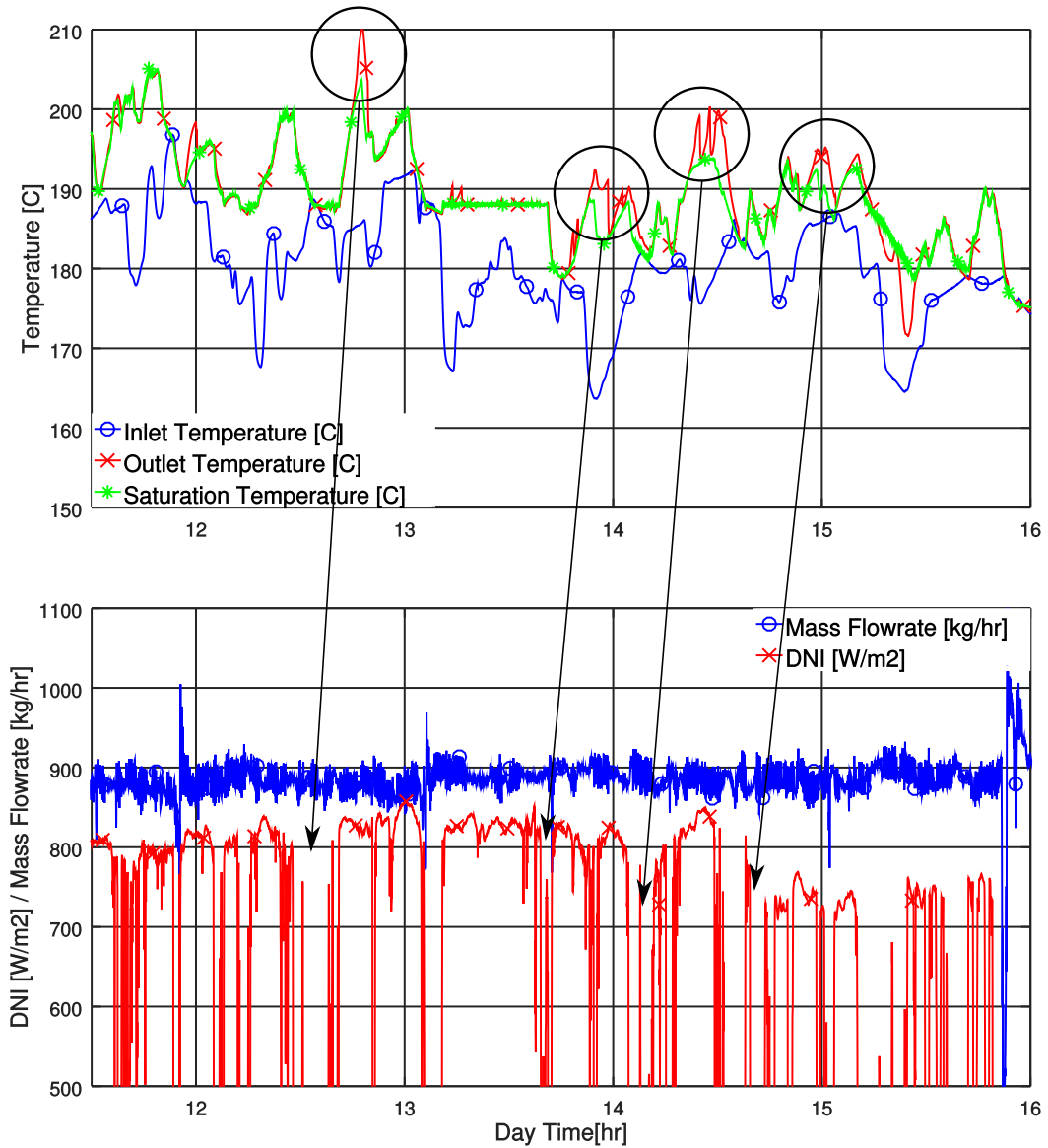
Figure 3.6: Measured response of the DSG system during sudden changes in irradiation levels causing overheating at collector outlet. Overheating events are associated with the reduced levels of DNI. (Testing facility : Hochdorf)

the liquid water is. Liquid water has both better heat transfer coefficient to the metal and also much higher heat capacity (heat of evaporation) which helps preventing overheating.

However, some of the solar irradiation does reach the top of the absorber when reflected by the secondary reflector. Since the heat transfer

to the steam on top is not high, combined with the relatively small energy needed to superheat the steam (sensible heat), the metal temperature can rise quite high during stratified and low flow situations.

Figure 3.7 depicts such a situation. Just before $t = 13.0hr$ the recirculation flow rate (bottom graph in blue) is reduced from $900kg/hr$ to $650kg/hr$. As can be seen the, the temperature measured by the outlet temperature sensor (top graph in red) rises above the saturation temperature (top graph in green) by up to 13.5^oC.

Because of the small size of the testing collector, the flow will be most of the time in the stratified flow regime. When the flow is high enough ($900kg/hr$, in this case), the liquid level in the absorber will immerse the temperature sensor which will then be measuring the saturation temperature. This case is depicted in Figure 3.8b. When the flow rate is lowered (to $650kg/hr$, in this case), the liquid level will fall below the sensor and it will then measure the superheated steam temperature as shown in Figure 3.8a.

This goes on to show that although the heating in Fresnel collectors mostly come from below, stratified flows can still result in overheating of the collector. The flow controller should aim to minimize stratified flows.

3.2.4 Steam Drum Fill Level Disturbance after Low Irradiation Events

Direct solar irradiation drops suddenly when a cloud passes above the solar field as seen Figure 3.10. Figure 3.9 presents such a situation. Due to the drop in DNI (bottom graph in red) at $t = 14.2hr$, heating is interrupted resulting in the steam drum pressure (top graph) to decrease.

Meanwhile steam inside the absorber starts to condense in the absence of any heat input. Since the volume originally occupied by steam should now be replaced by liquid water, water is provided from the steam drum through the recirculation pump. This is seen as a drop in steam drum level (middle graph) from 50% down to 40%.

Reacting to the steam drum level drop, the feed water pump controller will push water to the steam drum to raise the level. However, as solar irradiation is restored and steam regenerates in the absorber, all the extra water is pushed out of the absorbers and ends up in the steam drum resulting in an increase in water level by that very 10% reaching 60%.

This situation is undesirable since an increase in steam drum fill level can result in water carryover (water droplets being carried within the steam flow) as the liquid water level approaches the steam exit. This also increases the amount of time needed for the system to reach the operating temperature and pressure again as more cold water is injected by the feed pump.
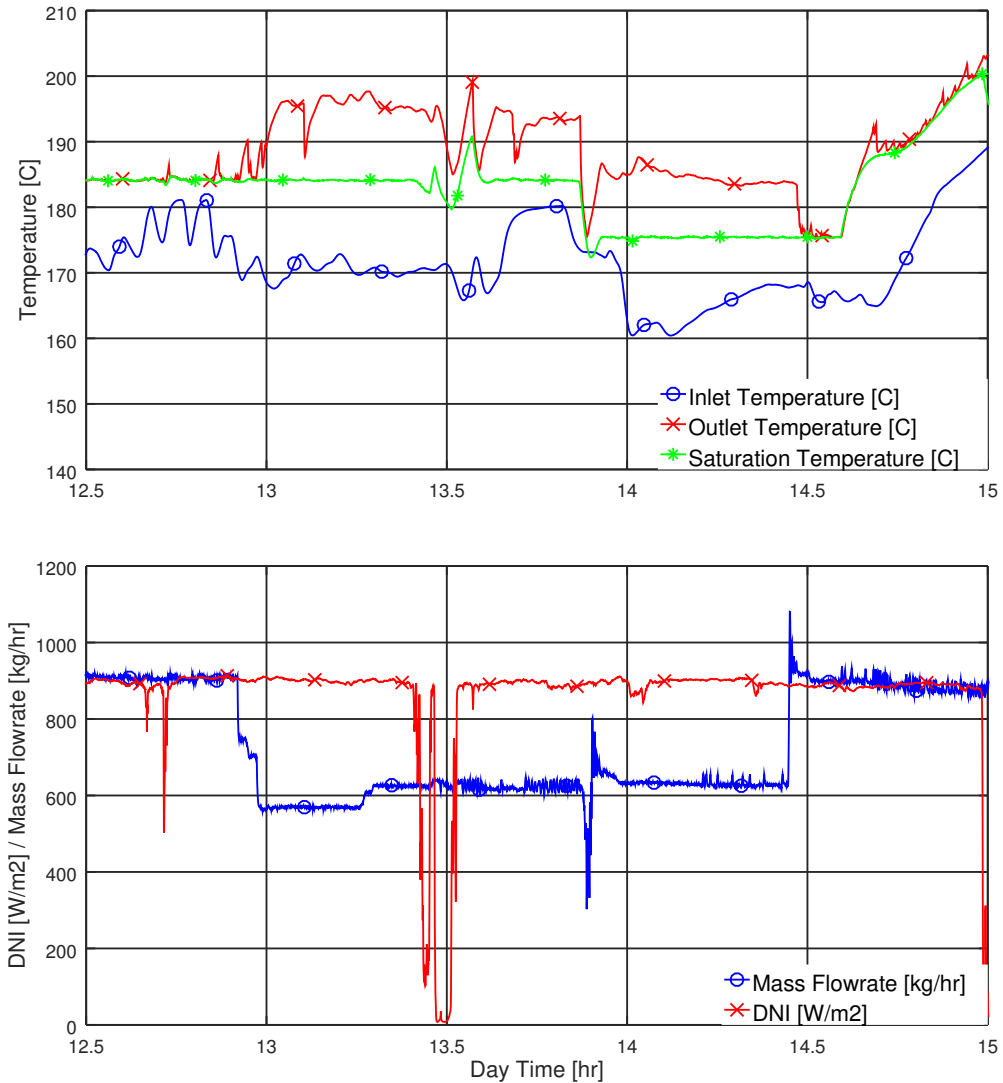
Figure 3.7: Stratified flow combined with a low flow rate causing steam over-heating at collector outlet. Steam overheating is identified by the rising of collector outlet temperature (red) above the saturation temperature (green) calculated from the steam drum pressure. (Testing facility : Hochdorf)

The situation can be mitigated by firstly detecting changes in DNI that can result is such behavior and then reducing the response of the feed water controller during those times. Or in control terms, using gain scheduling for the feedwater controller. This is further discussed in section 6.
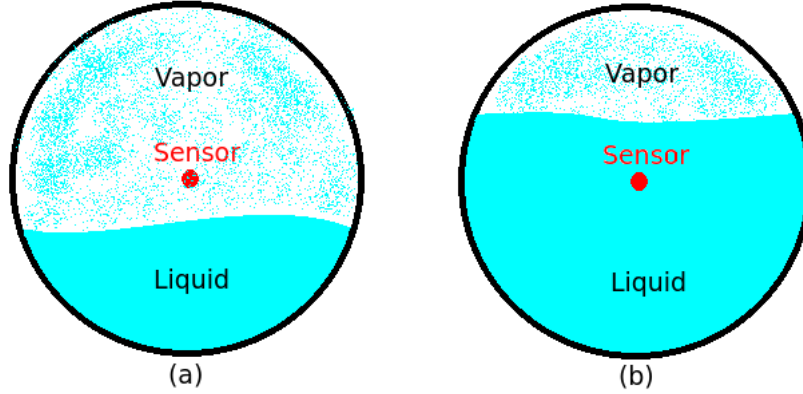
Figure 3.8: Depiction of absorber tube cross-section showing outlet temperature sensor. Liquid level in the absorber affects the temperature measurement.

3.2.5 Effects of Abrupt Pressure Changes on Steam Drum Level

Sudden changes in system pressure affects the actual and apparent water level of the steam drum. Interestingly, a positive or negative pressure change affects the steam drum level in different ways.

A pressure increase causes the steam drum liquid level to drop in two ways:

- A steady state drop.

- A transient drop.

The steady state drop is explained by the fact that the absorber tube will contain more liquid at higher pressure than at a lower pressure due to the increased density of vapor at higher pressure. Figure 3.11 illustrates the situation when the pressure increases at $t = 14.9hr$.

To explain what happens, let's assume that the water entering the absorber is at saturation. Then the average void fraction in the absorber can be calculated using Equation 3.1 in steady state,

$$
\begin{aligned}
\alpha_m &= \frac{h_{rec} - h_f + 0.5\dot{Q}_{net}/\dot{m}_{rec}}{h_{fg}}, \\
\gamma_m &= \frac{\alpha_m v_g}{v_f + \alpha_m(v_g - v_f)},
\end{aligned}
\tag{3.1}
$$

where α_m is the average steam quality in the absorber, h_{rec} is the inlet enthalpy, $\dot{Q}_{net}$ is the net power to the absorber, $\dot{m}_{rec}$ is the mass flow through the absorber, γ_m is the average void fraction in the absorber, v_g is saturated vapor specific volume and v_f is saturated liquid specific volume.
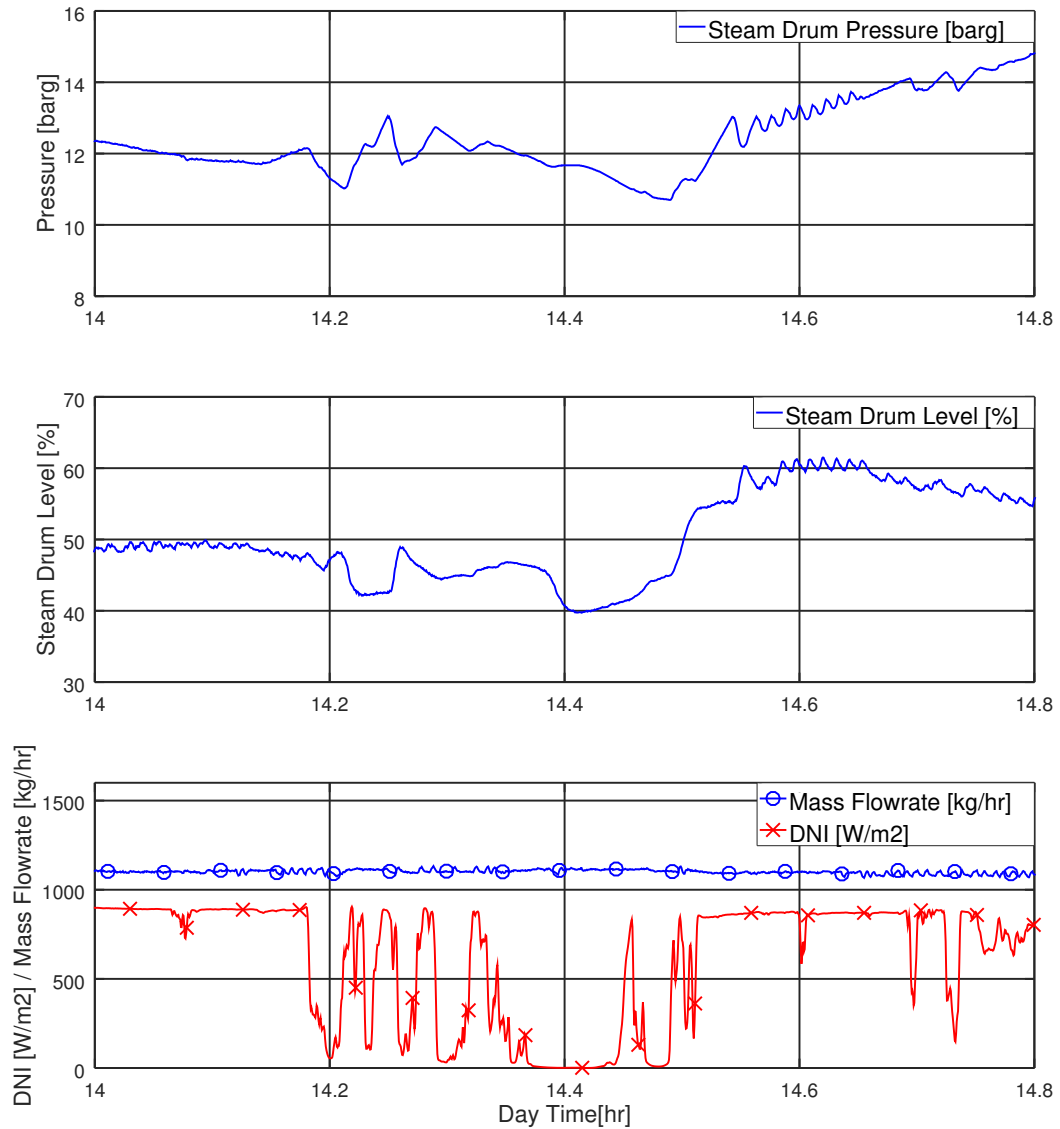
Figure 3.9: Measured response of steam drum level and pressure during a sudden dip in DNI. The drop in DNI results in a drop of steam drum pressure. In addition, one can notice a change in steam drum level from 50% **down to** 40% **and then up to 60%. (Testing facility : Hochdorf)**

Using Equation 3.1, the void fraction at $10bar_g$ is then 87.2% and the void fraction at $12bar_g$ is 85.4%, both being calculated assuming that the net input power to the absorber at that time did not change and remained at $51kW$, and so did the mass flow remain at $0.305kg/s$.

Figure 3.10: Cloud passing blocking the sun and causing a sudden drop in DNI

This reduction in the void fraction γ_m is mainly promoted by the reduction in specific volume of steam v_g at higher pressure, which in this case is reduced by 14.8% when moving from $10bar_g$ to $12bar_g$.

Knowing that the absorber volume is $83Litres$, this means that at higher pressure, the absorber has an extra $1.2kg$ of liquid inside. This explains why the level of the steam drum does not exactly return to its original level (at 50.2%) in Figure 3.11 when the pressure stabilizes at the new value of $12bar_g$ (level at 49.5%).

Note that the level change is too small to accurately measure it with the level sensor used which has a measurement accuracy of $\pm3mm$ in height, which corresponds to $\pm0.34\%$ measurement accuracy in volume percentage.

The transient drop in steam drum level is much larger than the steady state drop as seen in Figure 3.11. The level drops 47.1% before it starts increasing again to the steady state value of 49.5%.

To explain this we have to consider the fact that the inlet temperature to the absorber which comes from the steam drum changes slowly as the pressure increases to the new value. In the extreme case, if we assume that the inlet temperature remains at the saturation temperature of $10bar_g$, then the void fraction will be 64.1% instead of the steady state value of 85.4%. This translates to a reduction of steam drum level of 7.8%.
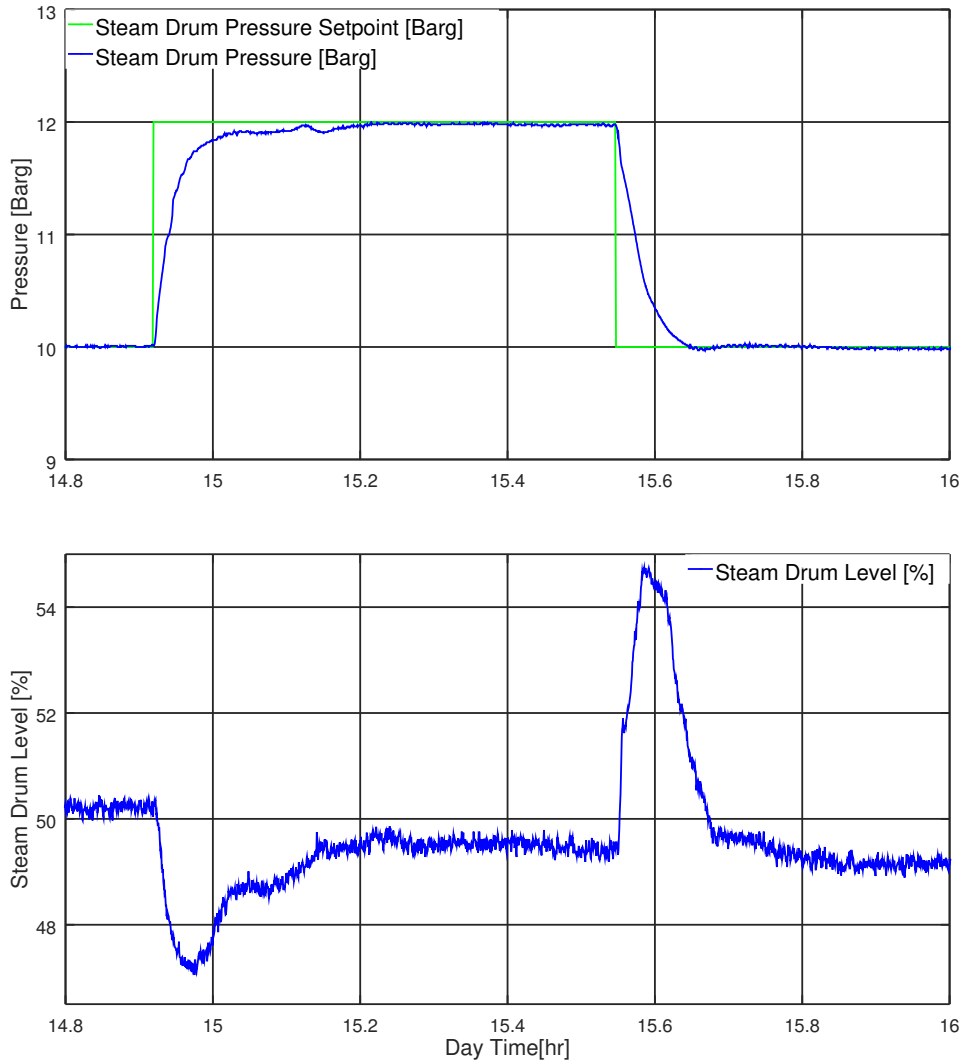
Figure 3.11: Measured response of steam drum level as a result of steam drum pressure change. (Testing facility : Hochdorf)

One would expect the opposite behavior when the steam drum pressure decreases. It is expected that the steam drum level will increase because the extra liquid which was added to the absorber is now forced out and back to the steam drum as a result of expanding steam . This is what happens indeed, as seen in Figure 3.11 at $15.5hr$ the pressure of the steam drum drops back to $10.0bar_g$, meanwhile the steam drum level increases. This time however the change in the steam drum level is 75% more than

the change induced by a pressure increase. While the pressure increase of $2bar$ resulted in a change of -3.00% in steam drum level, a pressure decrease of also $2bar$ resulted in a $+5.25\%$ change.

This additional change comes from another phenomena. As the pressure decreases, steam bubbles start forming under the liquid level in the steam drum. The volume of these bubbles will displace the liquid and result in an increased steam drum level. This is referred to as the swell effect which is common also in regular steam boilers.

The swell effect depends on how low does the system pressure drop below the saturation pressure of the liquid in the steam drum, which in turn affects the rate of bubble generation and flash steam production.

The swell effect depends on the amount of steam present under the liquid level. This in turn depends on where the solar field exit is connected to the steam drum. Having the two-phase flow pipe above the liquid level will be advantageous to reducing the swell-shrink effect induced by the steam bubbles since bubbles will mainly be present during flashing. This however results in noticeable stratification in the steam drum between the vapor and liquid phases, which can be as high as 10^oC, this reduces the effective storage capacity of the steam drum. Having the two-phase flow going under liquid level using special injectors will ensure homogeneous temperature distribution but will also significantly increase the amount of steam under the liquid surface and hence making the swell-shrink effect more frequent.

3.2.6 Dynamics of Steam Accumulation and Flash Steam

It is common in solar DSG systems to have a steam drum which provides several essential functions. Namely, it acts as a steam storage for brief periods of time when there is no irradiation, it operates as a pressure maintenance system making use of the steam cushion on top of the liquid, it provides phase separation for the two phase flow coming from the solar field and last but not least it provides a water reservoir to compensate the changes in water content in the solar field.

The steam drum has a relatively large thermal mass compared to the solar field, hence it plays a significant role in shaping the dynamic response of the whole system. This makes it of primary interest in control and modeling.

The steam drum acts as a steam accumulator that can provide flash steam to the load when solar irradiation is reduced because of a cloud for example, or when the load exceeds the generation capacity. The steam drum will typically have enough storage capacity to provide full nominal power for 5 to 30 minutes.

Figure 3.12 depicts such a situation. When the amount of steam generated by the solar field is less than the steam flowing to the load, steam drum pressure (top graph in blue) drops rapidly from $14.0bar_g$ until it reaches the

saturation pressure of the liquid in the steam drum at $12.3bar_g$ (top graph in red). At that point the pressure drop slows down, and flash steam is generated. During flashing, the steam drum pressure remains slightly below the saturation pressure of the liquid in the steam drum, i.e the liquid in the steam drum is a slightly superheated liquid.
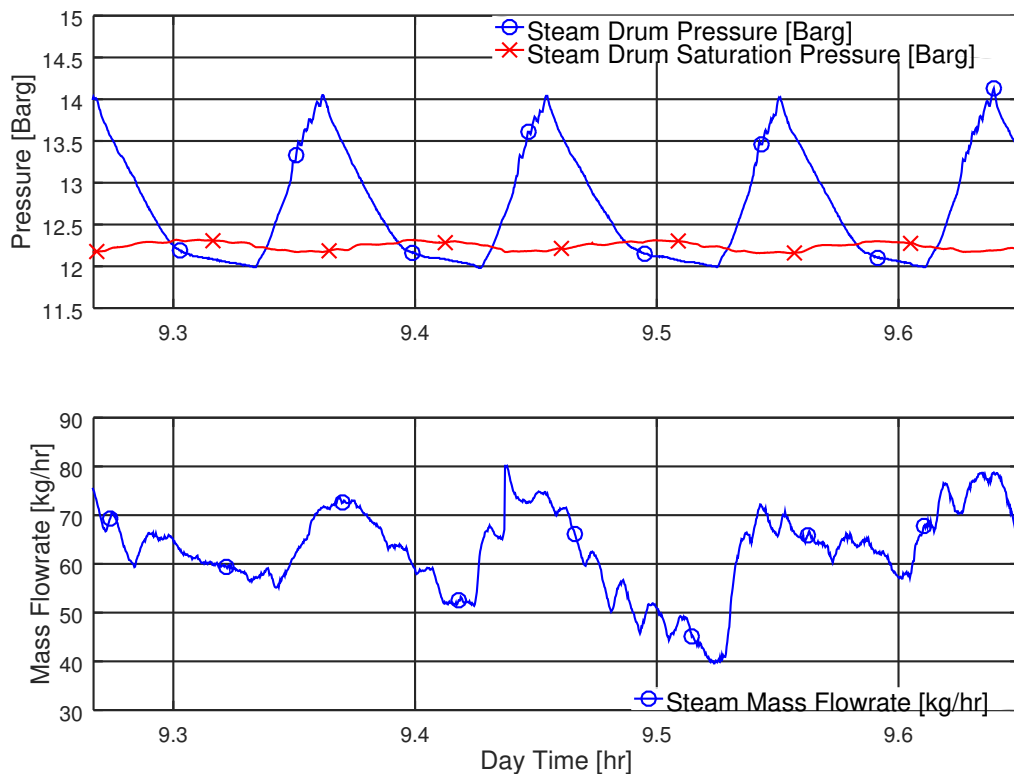
Figure 3.12: Measured response of the DSG system. Steam drum pressure (top in blue) drops rapidly when heating in the solar field is interrupted. The steep drop in pressure continues until it reaches the saturation pressure of the liquid inside the drum (top in red). The pressure drop rate decreases significantly as flashing starts. Steam flow (bottom in blue) correlates with the steam drum pressure. (Testing facility: RamPharma)

Figure 3.13 illustrates how the steam drum functions as a steam storage during periods of no solar irradiation. At the beginning of the test period at $t = 14.75hr$, the steam drum pressure (top graph in blue) is greater than the calculated steam drum saturation pressure(top graph in green). This means that the steam provided to the load is generated in the solar field.

Just before $t = 15.0hr$ a cloud passes reducing DNI. Since the steam demand continues as noticed from the steam mass flowrate (middle graph), the steam drum pressure drops sharply just below the saturation pressure.
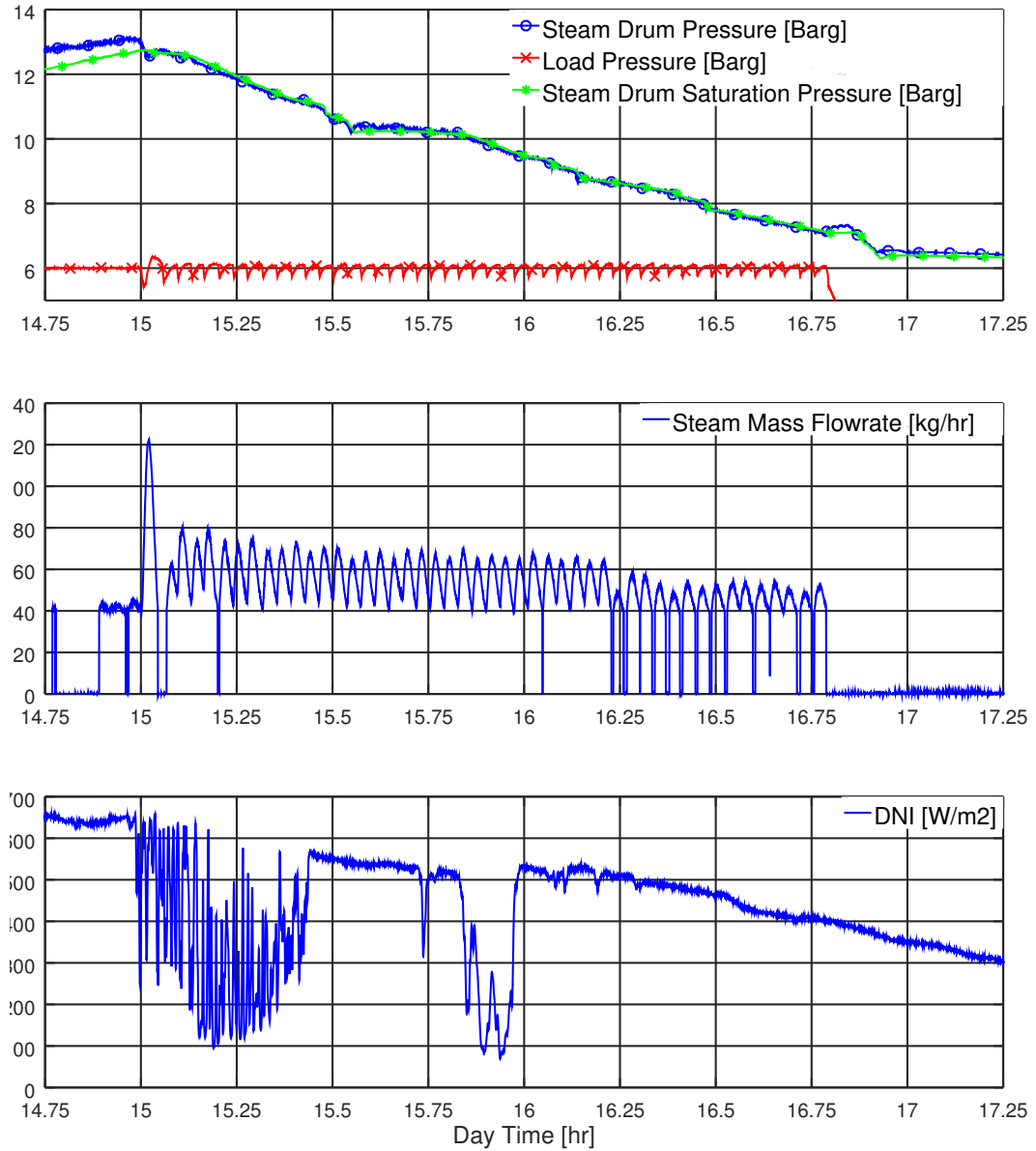
Figure 3.13: Measured response of the DSG system during low power situations. Steam drum providing flash steam to the load when solar irradiation is interrupted and when collector power is low at the end of the day. (Testing facility: RamPharma)

At that point flash steam is generated to supply the load. Afterwards, both steam drum pressure and the saturation pressure start dropping slowly. During this time, the pressure at the load side (top graph in red) is main-

tained at the setpoint of $6.0bar_g$.

As the cloud clears after at $t = 15.45hr$, the pressure of the system starts leveling and the steam drum pressure rises above the saturation pressure by $0.15bar_g$.

Another cloud passes at $t = 15.75hr$ causing flashing once again. The flashing continues even when the cloud clears because the collector power drops rapidly at the end of the day because of sun position. Flash steam however continues to supply the load maintaining it close to the setpoint of $6.0bar_g$ until $16.75hr$. At that point the pressure of the steam drum is only one bar above the load setpoint, thus the steam valve closes to prevent any steam flow from the load side to the solar system.

3.2.7 Recirculation Flow Dynamics and Nonlinearities

The control of recirculation flow in a solar system in single phase operation can be accurately achieved by linear controllers. The flow controller has only to account for changes in fluid density at different temperatures, changes which are very slow. In two-phase flow, however, the changes in the flow regime induced by varying operating conditions result in quick changes in the recirculation flow.

Figures 3.14 and 3.15 depict such a situation where the recirculation flowrate ($\dot{m}_{rec}$) drops as a consequence of pump cavitation during steam drum flashing.

In Figure 3.14, the steam flowrate to the load ($\dot{m}_s$) starts increasing at $t = 830s$. The steam flow increases from $180kg/hr \pm 20kg/hr$ up to a maximum of $250kg/hr \pm 20kg/hr$. Meanwhile, the pressure of the steam drum (p_{sd}) (middle graph in blue) starts dropping below the steam drum saturation pressure (middle graph in red) indicating that flash steam is being generated. Shortly after, at $t = 900s$ the recirculation pump inlet pressure (bottom graph in blue) drops below the saturation pressure (bottom graph in red) which indicates cavitation at the pump inlet.

This results in a reduction of recirculation mass flow rate ($\dot{m}_{rec}$) from the setpoint value of $1.2kg/s$ to $0.85kg/s$ (see Figure 3.15 top graph). The mass flowrate controller responds by increasing the pump speed (ω_{rec}) (middle graph) to restore the flowrate.

To prevent dangerous reduction in recirculation mass flow caused by abrupt flashing of liquid in the steam drum, flashing rate is limited by the control system. When a flashing induced reduction in flow is detected the steam valve controller will make an exception and reduce the steam flow rate to the load and hence limit the flashing rate. This is illustrated in the bottom graph of Figure 3.15 where the steam valve opening (O_{steam}) is reduced at $t = 950s$ in order to limit the flashing rate.
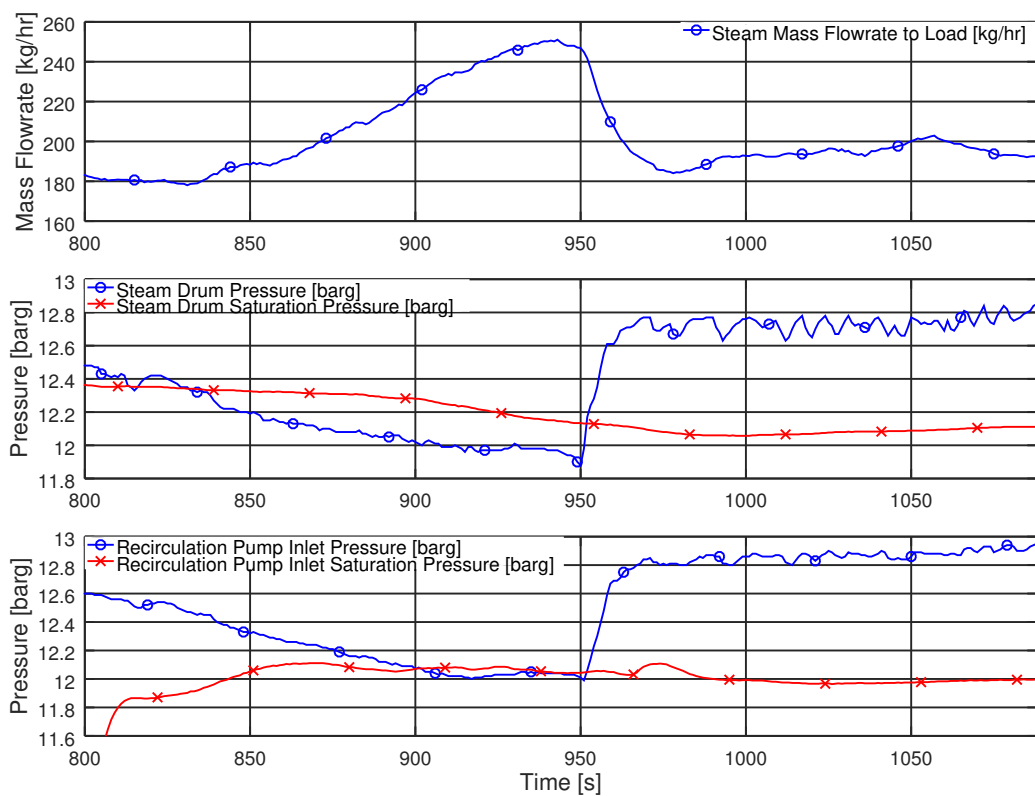
Figure 3.14: Measured response of the control system responding to an abrupt change in recirculation mass flowrate. Part 1: Steam mass flowrate increases (top) resulting in flashing at the steam drum (middle) and cavitation at the recirculation pump inlet (bottom). (Testing facility : RamPharma)
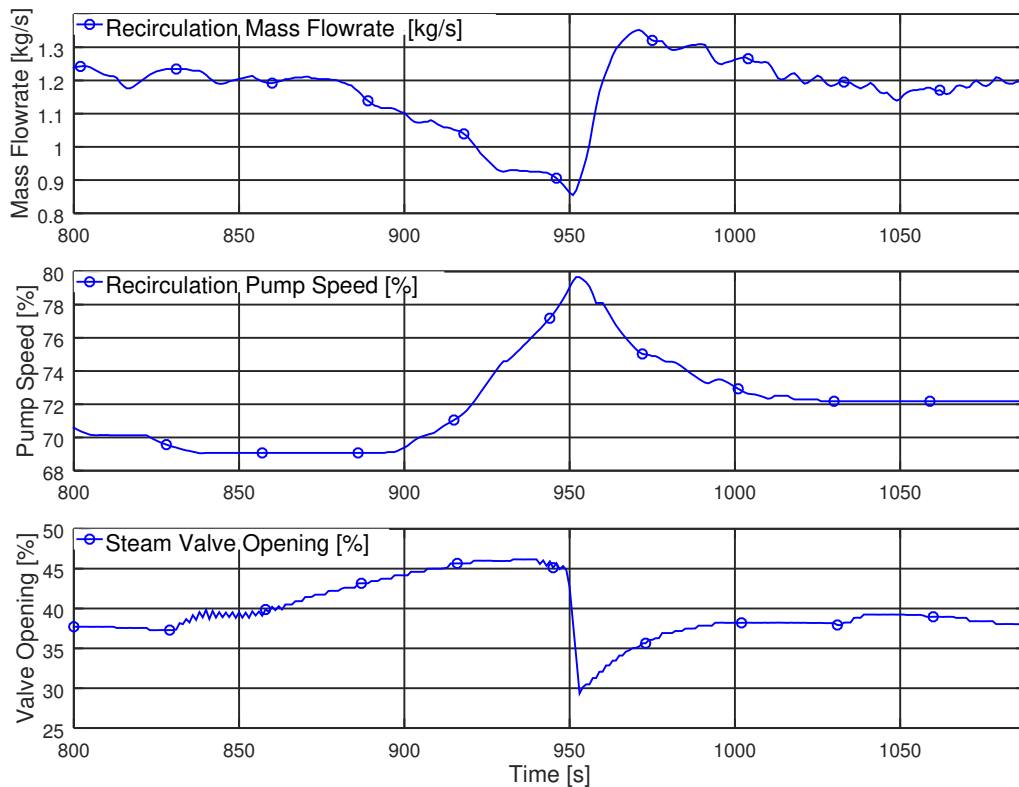
Figure 3.15: Measured response of the control system responding to an abrupt change in recirculation mass flowrate. Part 2: Recirculation mass flowrate drops below setpoint at $1.2kg/s$ **because of pump cavitation resulting from flashing in the steam drum (top). The recirculation mass flow controller responds by increasing pump speed (middle). In addition, the steam valve opening is reduced to limit flashing rate. (Testing facility : Ram-Pharma)**

3.3 Measurement of Flow Patterns During Typical Operational Transients

To better understand the flow variation in the solar field, a Wire Mesh Sensor (WMS) (see Appendix A) is used to measure flow pattern at the solar field exit in the testing facility in Hochdorf. This data is acquired using the WMS developed by the Helmholtz-Zentrum Dresden-Rossendorf (HZDR). The measurement campaign has been done within the SoProW project funded by the German Federal Ministry for Economic Affairs and Energy (BMWi) (Funding reference number:FKZ0325999B)[10].

The WMS provides a two dimensional matrix ($M(x, y)$) of void fraction distribution at the solar field outlet. Combining several cross-sectional measurements from the sensor, one can obtain a time series of void fraction distributions that represent the flow regime ($\hat{M}(x, y, t)$). The three dimensional matrix ($\hat{M}(x, y, t)$) can be averaged in the x-axis to yield a two dimensional representation of the flow regime as seen in Figure 3.16.

During direct steam generation the flow pattern in the absorber tube changes depending on operation conditions. The change of flow pattern in the absorber affects the stability and safety of the DSG system . Using the WMS the change in flow regimes at the collector outlet can be observed. This gives a better understanding of the transient effects that occur during direct steam generation operation. In this section, experimental data of the observed flow patterns during different DSG operation conditions are presented.

Sudden Reduction of Solar Field Power

Sudden reduction of solar power can result from a drop in DNI because of clouds for example, or from mirror defocusing triggered by a safety event like overheating for instance.

Figure 3.16 depicts the experimentally observed flow pattern just before mirror defocusing. The flow pattern is stratified as seen in the figure. As the mirrors defocus and the evaporation rate reduces, the amount of liquid inside the absorber increases raising the level and creating waves as can be seen in Figure 3.17. Defocusing also results in system pressure reduction promoting flash steam generation. Moreover, the increased liquid level in the absorber reduces the available area for steam which increases its speed. However this increase is counteracted by a reduced amount of steam flow caused by the reduction in power.

For bigger systems with longer loops, it is actually expected that the liquid level will first drop before it rises creating a danger of dryout as described by [27]. This is not the case here as the system is too small to see such effect.
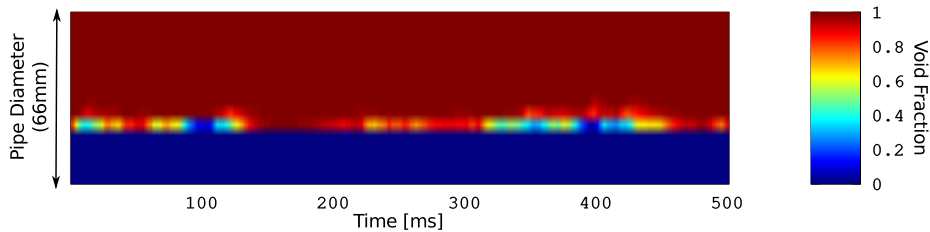
Figure 3.16: Two phase flow pattern in the absorber tube exit reconstructed from the WMS measurement. Sudden Reduction of Solar Field Power (a): Stratified slightly wavy flow observed just before defocusing the mirrors to create a sudden solar field power reduction (Steam Drum Pressure $5bar_g$**, Recirculation Flow** $1.29m^3/hr$**, Steam Flow** $26kg/hr$**, DNI** $849W/m^2$**) (Testing facility : Hochdorf).**
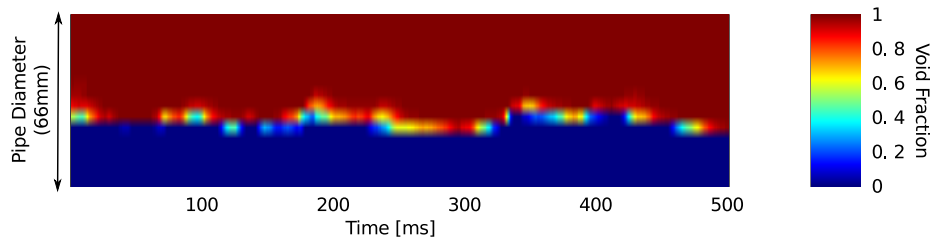
Figure 3.17: Two phase flow pattern in the absorber tube exit reconstructed from the WMS measurement. Sudden Reduction of Solar Field Power (b): Waves start to develop with an amplitude smaller than the pipe diameter as the flow transitions to a wavy flow. (Steam Drum Pressure $5bar_g$**, Recirculation Flow** $1.29m^3/hr$**, Steam Flow** $26kg/hr$**, DNI** $849W/m^2$**) (Testing facility : Hochdorf).**

Sudden Increase in Solar Field Power

A sudden increase in solar field power results from DNI changes caused for example by a passing cloud or by refocusing of the mirrors after a safety event. Both the WMS measurements as well as practical experience show that sudden increase in the power results in instabilities and flow induced vibrations that are stressful for the system.

Before the increase in solar field power, the flow has been measured by the WMS and stratified flow is detected as shown in Figure 3.18.

As the power is increased, the flow transitions quickly to intermittent flow as shown in Figure 3.19. When the power is suddenly increased the saturated liquid starts boiling and the vapor content in the absorber increases. With increased steam velocity and probably also bubble induced turbulence, liquid high waves are generated which reach the top of the tube.

As the waves reach the top of the tube, steam path way is blocked forming a steam plug. As the system stabilizes again, the flow regime transforms again to stratified wavy flow as seen in Figure 3.20.
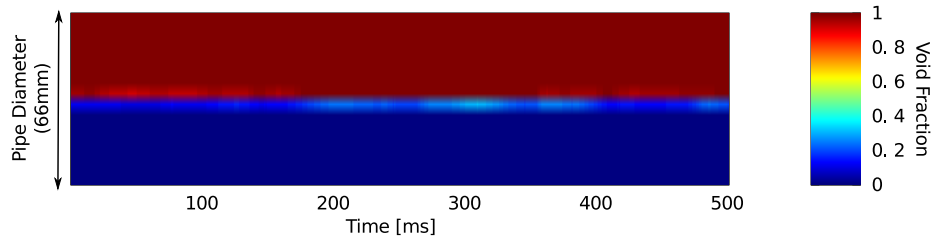
Figure 3.18: Two phase flow pattern in the absorber tube exit reconstructed from the WMS measurement. Sudden Increase in Solar Field Power (a): Calm stratified flow observed just before focusing the mirrors to create a sudden increase in solar field power (Steam Drum Pressure $5.2bar_g$**, Recirculation Flow** $1.52m^3/hr$**, Steam Flow** $62kg/hr$**, DNI** $865W/m^2$**) (Testing facility : Hochdorf).**
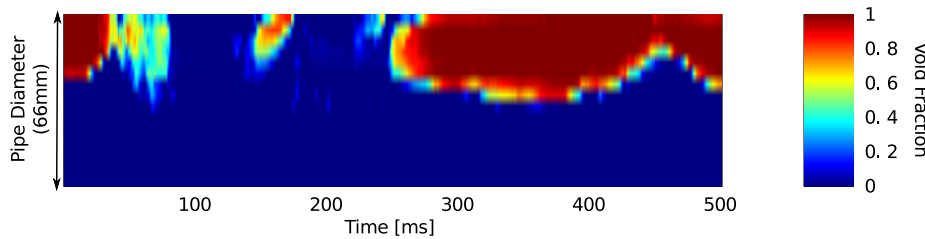
Figure 3.19: Two phase flow pattern in the absorber tube exit reconstructed from the WMS measurement. Sudden Increase in Solar Field Power (b): The flow quickly transforms to intermittent flow as the power is restored and the saturated liquid starts boiling. (Steam Drum Pressure $5.2bar_g$**, Recirculation Flow** $1.52m^3/hr$**, Steam Flow** $62kg/hr$**, DNI** $865W/m^2$**) (Testing facility : Hochdorf).**

Flashing

Flashing occurs in the solar system when the amount of delivered steam exceeds the amount of steam generated in the solar field. This results in a gradual drop in steam drum pressure. When steam drum pressure drops below the saturation pressure of the liquid inside the steam drum, flash steam starts generating in several parts of the system. This increases the amount of steam in the absorber and changes the flow regime to wavy with high wave amplitude, almost transforming to intermittent flow as can be
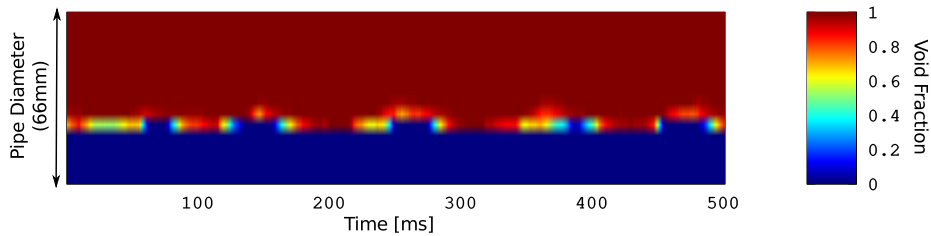
Figure 3.20: Two phase flow pattern in the absorber tube exit reconstructed from the WMS measurement. Sudden Increase in Solar Field Power (c): As the flow stabilizes it restores to stratified-wavy flow pattern (Steam Drum Pressure $5.2bar_g$**, Recirculation Flow** $1.52m^3/hr$**, Steam Flow** $62kg/hr$**, DNI** $865W/m^2$**) (Testing facility : Hochdorf).**

seen in Figures 3.21 and 3.22. As the flashing stops when the steam valve closes, the flow regime restores to wavy-stratified flow.
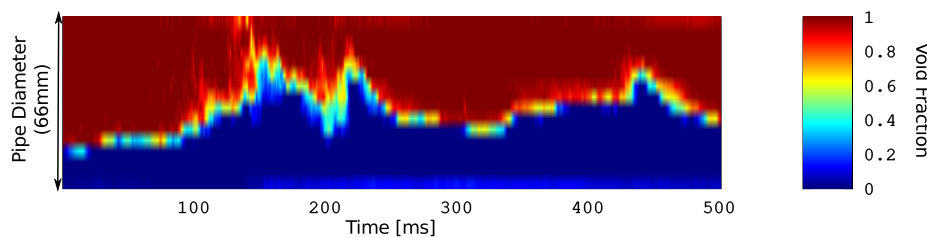
Figure 3.21: Two phase flow pattern in the absorber tube exit reconstructed from the WMS measurement. Flashing (a): High amplitude waves noticed during flashing (Steam Drum Pressure $4.9bar_g$**, Recirculation Flow** $1.19m^3/hr$**, Steam Flow** $86kg/hr$**, DNI** $849W/m^2$**) (Testing facility : Hochdorf).**
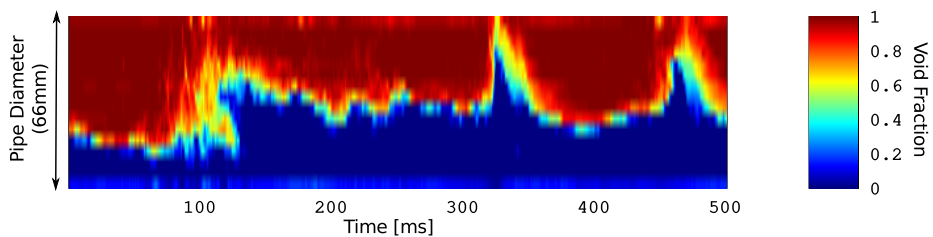
Figure 3.22: Two phase flow pattern in the absorber tube exit reconstructed from the WMS measurement. Flashing (b): High amplitude waves noticed during flashing (Steam Drum Pressure $4.9bar_g$**, Recirculation Flow** $1.19m^3/hr$**, Steam Flow** $86kg/hr$**, DNI** $849W/m^2$**) (Testing facility : Hochdorf).**

Transition from Lower to Higher Flow rate

The transition from lower to higher flow rate has an effect on the flow regime. However, here the flow pattern is mostly stratified or stratified wavy. Hence, the change of mass flow mainly affects the liquid level at the bottom of the pipe as seen in Figures 3.23 and 3.24.

As the steam quality and mass flux increase, it is expected that the change of mass flow will affect the flow regime more clearly.
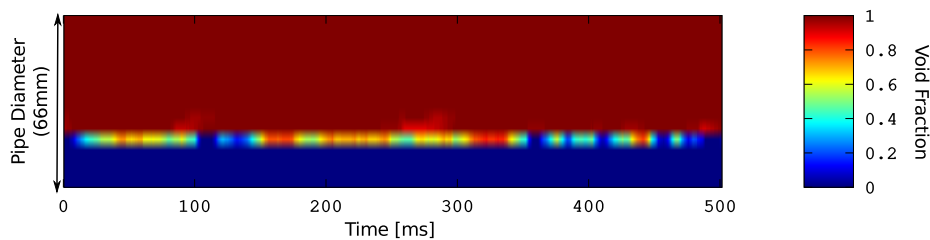
Figure 3.23: Two phase flow pattern in the absorber tube exit reconstructed from the WMS measurement. Transition from Lower to Higher Flow rate (a): Lower flow rate in stratified flow evident from the reduced liquid level compared to Figure 3.24 (Steam Drum Pressure $5.0bar_g$, Recirculation Flow $1.0m^3/hr$ to $2.45m^3/hr$, Steam Flow $73kg/hr$, DNI $805W/m^2$)(Testing facility : Hochdorf)
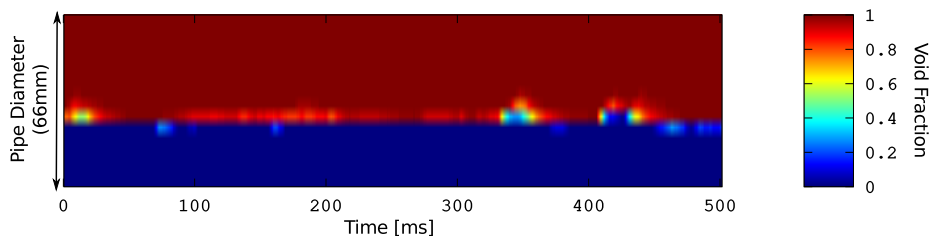
Figure 3.24: Two phase flow pattern in the absorber tube exit reconstructed from the WMS measurement. Transition from Lower to Higher Flow rate (a): Higher flow rate in stratified flow evident from the increased liquid level compared to Figure 3.23 (Steam Drum Pressure $5.0bar_g$, Recirculation Flow $1.0m^3/hr$ to $2.45m^3/hr$, Steam Flow $73kg/hr$, DNI $805W/m^2$)(Testing facility : Hochdorf)

Chapter 4

Physical Models of the Linear Fresnel Collector Plant

4.1 Development of a Physical Model in Single Phase Flow

A lumped element model of the single phase flow system is developed in this section. This modeling effort is needed firstly to understand the main system dynamics and then help developing a suitable control strategy. Generally speaking, simplified models like the lumped element model are usable for model based control.

Figure 4.1 illustrates system layout in single phase operation. The absorber tube represents the heat source, where the heat transfer fluid enters with a temperature of T_i. As the fluid travels across the absorber, it gets heated to the outlet temperature T_o. The mass flow rate in the absorber tube ($\dot{m}_{rec}$) is manipulated using the circulation pump to maintain a constant outlet temperature (T_o). The outlet temperature of the absorber can also be manipulated by changing the amount of solar energy focused on the absorber using the primary mirror.

4.1.1 Development of Plant Lumped Element Physical Models in Single Phase Mode

Most industrial processes can be described by a linear high order system of differential equations. This is because most systems are actually composed of many smaller elements of first order dynamics, the combination of which will result in a high order linear model [14]. In the case of the absorber pipe of the Fresnel collector, these small elements are mass elements distributed along the absorber length.

Since high order models are hard to use for control purposes, it's common to approximate dynamic systems with a first order system and a pure

$$\dot{Q}_{net} = \dot{Q}_{solar} - \dot{Q}_l$$
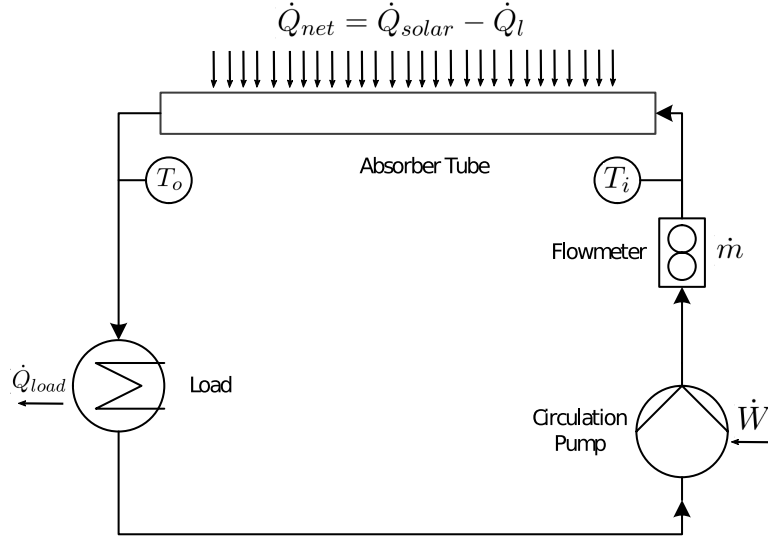
Figure 4.1: Hydraulic flow configuration in single phase mode

time delay [14]. This is especially true when one time constant is dominating system dynamics. The other smaller time constants act together to produce a lag that acts as a pure time delay [14]. The transfer function in the s-domain for such a system ($G(s)$) is given by Equation 4.1,

$$G(s) = \frac{b}{\tau s + 1}e^{-s\kappa}, \tag{4.1}$$

where, τ is system time constant, b static gain, and κ is the dead time.

This model is called the lumped element model. The main simplifying assumption for such a model is considering the absorber tube as one concentrated element and hence neglecting the temperature distribution along its length. Because of its simplicity, it lends itself easily for experimental parameter identification which is a big advantage over higher order models. In this section the derivation of lumped parameter model is presented. Experimental identification of the important model parameters is also shown.

Since the main dynamics of interest from control perspective occur in the absorber pipe, it is suitable to draw the control volume around it. Taking an energy balance as seen in Equation 4.2:

$$\dot{Q}_{solar} = \dot{m}_{rec}c_p(T_o - T_i) + \dot{Q}_l + \frac{dE_{abs}}{dt}, \tag{4.2}$$

where $\dot{Q}_{solar}$ is the solar heat absorbed (W), $\dot{Q}_l$ is the overall heat loss through the absorber tube (W), $\frac{dE_{abs}}{dt}$ is the temporal change in the absorber stored thermal energy (W), E_{abs} is the thermal energy stored in the
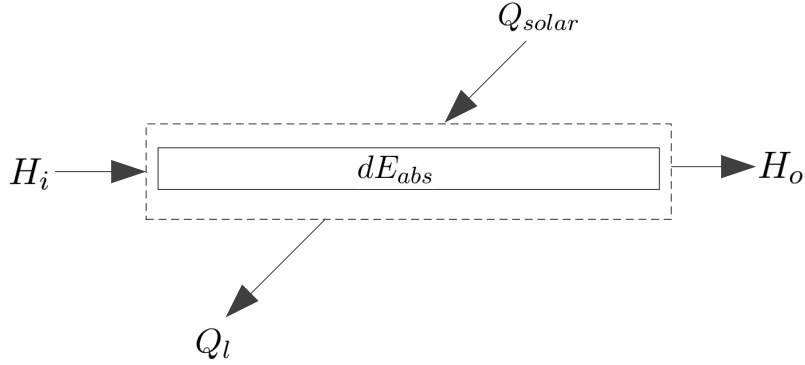
Figure 4.2: Energy balance around the absorber tube

absorber tubes in (W) and t is time in (s), $\dot{m}_{rec}$ is the mass flow rate inside the absorber (kg/s), c_p is the specific heat of liquid water $(kJ/(kg.K))$, T_o is water temperature at the absorber outlet (^oC) and T_i is water temperature at the absorber inlet (^oC).

Since the change in absorber temperature is close to the change of the outlet temperature, and also the change in the absorber stored energy is relatively small (less than %5 when the collector is in operation and zero when in steady state), then the change in the stored energy in the absorber can be approximated by:

$$\frac{dE_{abs}}{dt} = C_{abs}\frac{dT_o}{dt}. \tag{4.3}$$

Here, C_{abs} represents the overall thermal mass of the absorber tube (kJ/K). Rearranging and taking the net heat transfer across the absorber $\dot{Q}_{net}$ = $\dot{Q}_{solar}$-$\dot{Q}_l$.

$$\dot{Q}_{net} = \dot{m}c_p(T_o - T_i) + C_{abs}\frac{dT_o}{dt}, \tag{4.4}$$

where c_p is taken as a constant evaluated at a suitable average temperature.

Now let $\tau= C_{abs}/\dot{m}_{rec}c_p$ and $F = 1/\dot{m}_{rec}$ then,

$$\frac{\dot{Q}_{net}}{c_p}F + T_i = T_o + \tau\frac{dT_o}{dt}. \tag{4.5}$$

Taking Laplace transform [1], Equation 4.5 is transformed into:

$$\frac{\dot{Q}_{net}}{c_p}F(s) + T_i(s) = T_o(s)[1 + \tau s], \tag{4.6}$$

---

[1] Variables in the frequency domain are only differentiated from the time domain by explicitly writing the independent variable (s) after the dependent variable, e.g. $F(s)$.

which can be rearranged to:

$$T_o(s) = \left[\frac{\dot{Q}_{net}}{c_p} F(s) + T_i(s) \right] \left[\frac{1}{1 + \tau s} \right]. \tag{4.7}$$

Because water requires a finite amount of time to pass through the absorber tube from the inlet to the outlet, a pure time delay or dead time is introduced. This time delay depends on the absorber tube length (or precisely its volume) and the volume flow rate. Pure time delay is modeled in the s-domain as $e^{-s\kappa}$, where κ is the dead time. Hence, Equation 4.7 can be modified to include the pure time delay.

$$\underbrace{T_o(s)}_{\text{Output}} = \underbrace{\left[\frac{\dot{Q}_{net}}{c_p} F(s) + \underbrace{T_i(s)}_{Disturbance} \right]}_{\text{Input}} \underbrace{\left[\frac{1}{1 + \tau s} \right]}_{\text{Plant}} \underbrace{\left[e^{-s\kappa} \right]}_{\text{Pure Time Delay}}. \tag{4.8}$$

In this model the inlet temperature of the collector is dealt with as a disturbance since it mainly depends on the load which can not be controlled. The input in this model is F or the reciprocal of the mass flow rate which can be controlled by changing the pump speed.

4.1.2 Analysis of Model Uncertainty

The control system uses the model to calculate the necessary mass flow rate to achieve a certain outlet temperature. For purposes of uncertainty analysis, consider the steady state form of Equation 4.2:

$$\dot{Q}_{solar} = \dot{m}_{rec} c_p (T_o - T_i) + \dot{Q}_l. \tag{4.9}$$

The equation can be rearranged to evaluate $\dot{m}_{rec}$ as follows:

$$\dot{m}_{rec} = \frac{\dot{Q}_{solar} - \dot{Q}_l}{c_p (T_o - T_i)} = \frac{\dot{Q}_{net}}{c_p (T_o - T_i)}. \tag{4.10}$$

The calculation of $\dot{m}_{rec}$ then requires the calculation of $\dot{Q}_{solar}$ and $\dot{Q}_l$. The solar energy reaching the absorber ($\dot{Q}_{solar}$) is calculated using Equation 2.5. The sources of uncertainty based on Equation 2.5 are:

1. Overall Optical Efficiency: the optical efficiency of the collector is a combination of several factors (as described in Section 2.1.1). The dominant source of uncertainty in the evaluation of optical efficiency is modeling error. In addition to the errors in determining the IAM functions of the collector and the maximum optical efficiency, some un-modeled physics contribute to the uncertainty. For example, the effect of soiling, reflective surface accuracy, solar field orientation, installation in accuracy, alignment accuracy of collector parts, soiling

and dirt accumulation. The overall uncertainty in optical efficiency is estimated to be $< \pm 10\%$ under normal conditions of clean mirrors and accurate alignment of collector components.

2. Solar irradiation (DNI) measurement uncertainty. This depends on the measurement instrument used. For tracking pyrheliometers measurement uncertainty of $\pm 50 W/m^2$ is expected. This includes the uncertainty of both the pyrheliometers and the tracking device. Using a shadow pattern pyranometer, the uncertainty is much larger at $\pm 150 W/m^2$. Here soling plays an important role again, the uncertainty indicated refers to clean instruments.

3. Area of the reflective surface: the uncertainty in determining the area of the reflective surface is related to the accuracy of the manufacturing process of the individual mirror facets. The overall accuracy in determining the total area is less than $\pm 0.5\%$.

The combined uncertainty for the evaluation of $\dot{Q}_{solar}$ ranges between $\pm 12.3\%$ to $\pm 18.7\%$ based on the DNI measurement used.

The uncertainty in the evaluation of the heat loss of the absorber ($\dot{Q}_l$) is provided in [3] to be less than 10%.

The uncertainty in $\dot{Q}_{net}$ is a combination of the uncertainty in $\dot{Q}_{solar}$ and $\dot{Q}_l$. The uncertainty in $\dot{Q}_{net}$ ranges between $\pm 12.4\%$ to $\pm 18.9\%$. Note that the contribution of $\dot{Q}_l$ to the uncertainty is small because heat losses in the absorber are relatively small.

The temperature measurement uncertainty for the inlet and outlet temperature is $\pm 0.15 K$.

Therefore the overall uncertainty in the calculation of the required mass flow rate ranges between $\pm 12.5\%$ and $\pm 18.9\%$ depending on the DNI measurement used. By far the uncertainty is dominated by the uncertainty in the determination of $\dot{Q}_{solar}$.

The uncertainty in the measurement of the actual mass flow rate combines the uncertainty of volume flow measurement ($\pm 0.25\%$) and uncertainty in evaluating fluid specific volume. The uncertainty in evaluating specific volume is less than $\pm 0.05\%$ according to [34]. Including the uncertainty in measured temperature, the uncertainty rises up to $\pm 0.07\%$. Therefore the overall uncertainty in measuring mass flow rate is $\pm 0.26\%$. As expected the uncertainty is dominated by the uncertainty of volume flow measurement and not the calculation of specific volume.

4.1.3 Plant Experimental Identification using Reaction Curve Model

The plant model is defined in equation 4.1, next step is to identify the model parameters, namely the static gain b, the time delay τ and the dead

time κ. The most commonly used method for such identification process is the step response reaction curve as described in [14].

The idea is to apply an input with a certain magnitude and frequency and record how the process reacts to the input. A step function is very well suited for such a task since it contains a wide range of frequencies and is practically easy to implement.

Figure 4.3 depicts the response of the system to a step change in the flow rate after an amble time of nearly static conditions of inlet temperature (blue) and DNI (green). The positive step input produces a negative response in the outlet temperature as expected.
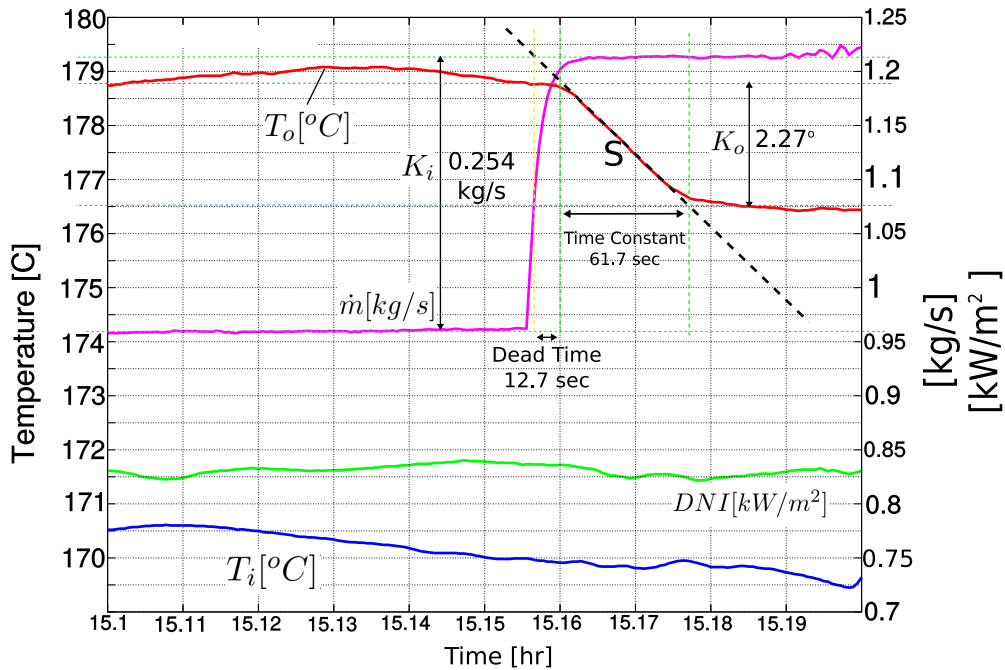
Figure 4.3: Experimental identification of system parameters using reaction curve method in the Hochdorf Plant. Excitation using a step function of mass flow rate. Parameter identification using curve slope at inflection point (denoted as yellow dotted line).

There are two methods for interpreting the reaction curve, the first one is illustrated in Figure 4.3. It depends on drawing a straight line through the inflection point of the response curve. For a first order system, the slope (S in the figure) of the line at the inflection point defines the maximum rate of change in the output. If the system's output continues to change in the same rate, then it would reach steady state in one time constant only.

Based on Figure 4.3, the model parameters are as follows:

- static gain $b = K_o/K_i = -8.9^oCs/kg \pm 0.6^oCs/kg$,

- time constant $\tau = 61s \pm 1s$,

- dead time $\kappa = 12s \pm 1s$.

Another method to interpret the results is shown in Figure 4.4 [14]. In this method the time needed for the system to reach 28.3% at t_1 and 63.2% at t_2 of its steady state is measured. Based on the measurements the model parameters are evaluated as follows:

- static gain $b = K_o/K_i = -8.9^oCs/kg \pm 0.6^oCs/kg$,

- time constant $\tau = 1.5(t_2 - t_1) = 1.5(51 - 30) = 31.5s \pm 2s$,

- dead time $\kappa = 1.5(t_1 - 1/3t_2) = 1.5(30 - 51/3) = 19.5s \pm 2s$.
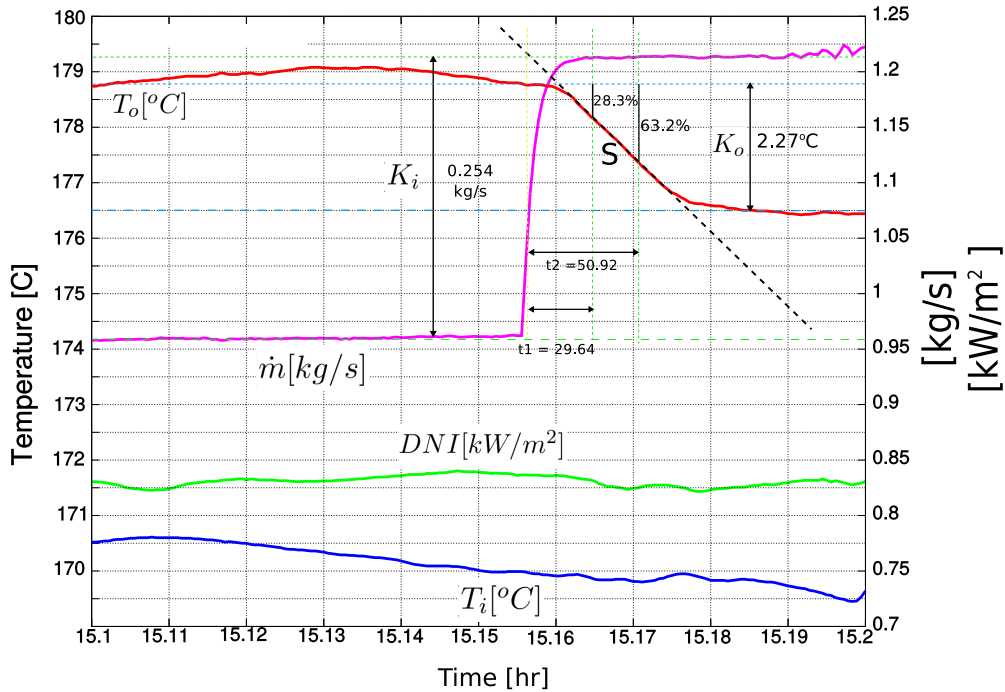
Figure 4.4: Reaction curve method. Excitation using a step function of flow rate. Parameter identification using time measurement.

The two methods provide significantly different outputs in the approximation of time constant and dead time. This is mainly because the system response is not exactly matching a first order system which these methods are estimating. It can be seen from the results that the second method compensated for the smaller time constant with a higher dead time. Since the first method requires the more prone to error line fitting procedure, the results from the second method are to be used further, namely, $\tau = 31.5s$, $\kappa = 19.5s$ and $b = -8.9^oCs/kg$. Hence,

$$G_p(s) = \frac{-8.9}{31.5s + 1}e^{-19.5s}. \tag{4.11}$$

4.2 Development of a Physical Model in DSG Mode

In this section a model for the system in DSG mode is developed. The DSG design considered is the recirculation mode as described in 2.3. In recirculation mode, the steam drum represents a key component in governing the dynamic behavior of the DSG systems. The steam drum is seen as a system stabilizing component. Because of it relatively large fluid mass content, 90% of the fluid mass is normally inside the steam drum, the steam drum has a large effect on the system behavior.

The second important part in determining system dynamics is the solar field. From modeling point of view the solar field can be thought of as uniformly heated pipe with two phase flow. The interaction between the steam drum and the solar field will determine the dynamic behavior of the system.

The main objectives of developing the model are to:

- Deduce a suitable model for model-based control strategy.

- Provide a simulation tool for DSG system behavior and control strategy testing.

Typically the steam drum is partly filled with liquid and the upper void is filled with saturated steam as depicted in Figure 4.5. Steam is taken from the upper part of the steam drum. To ensure that only steam is withdrawn from the steam drum, the liquid level is maintained below the steam outlet.

The two-phase flow coming from the collector field is fed into the drum through a series of metal plates that reduce the momentum of the water droplets and force them to settle in the liquid pool. The steam drum also features a port for recirculation, were saturated water is pumped into the collector field to be partly evaporated. Feed water is pumped into a fourth port in the steam drum which is positioned close to the recirculation port to avoid upsetting the equilibrium inside the drum and to ensure that the coldest water is being pumped to the collector field.

The liquid part can also contain some steam bubbles which can both expand or collapse depending on pressure level. Steam in the bubbles will also condense when feedwater is added releasing the condensation heat and thereby increasing the temperature of the feedwater.[43]

In order to come up with a simple enough model for control purposes, several simplifying assumptions have been introduced:

- The fluid in the solar field is assumed saturated all the time at the same pressure as that of the steam drum. This is not always true when the steam on top of the absorber tube overheats where there is still water in the bottom of the tube. Such condition can happen when the flow inside the absorber tube is stratified. But as the flow mixes in the pipe towards the drum the resulting deviation is marginal.
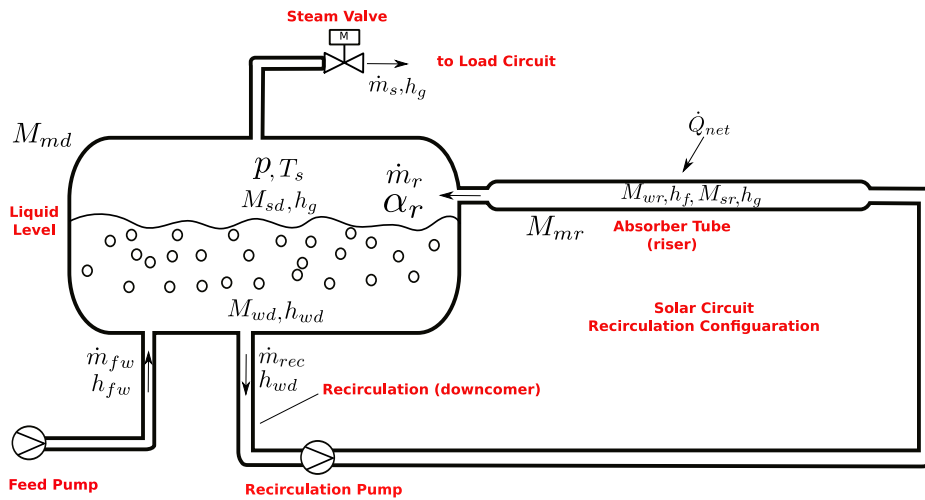
Figure 4.5: Schematic diagram of the DSG system in recirculation configuration depicting the steam drum and the solar circuit. System parameters relevant for the model are assigned.

- A no-slip condition is assumed inside the absorber tubes. That is, the velocities of the liquid and vapor phases are identical. By applying this approach mass conservation is ensured.

- Steam quality inside the absorber tubes changes linearly as the fluid progresses through the field. There it is assumed that the solar heat input on the absorber tube is constant through out the collector field leading to a constant heat flux condition.

- No boiling occurs in the recirculation line (downcomer).

- The steam in the drum is always at saturation.

- There is no temperature gradient within the phases in the steam drum.

- The temperature of the metal is assumed to be always at saturation temperature. It is reported in [4] that the deviation of metal temperature from the saturation temperature is very small during detailed simulations. Hence, the expected inaccuracy from this assumption is considered negligible.

Unlike other models, the model introduced here considers nonequilibrium between the phases in the steam drum and sub-cooled water flowing through the recirculation line. It also includes the thermal heat capacity of the steam drum metal.

In order to build the model an energy and mass balance is made on the control volumes of the steam drum and the absorbers in the solar field. In

70

order to allow for non-equilibrium in the steam drum between the steam and liquid phases, the balance equations are also applied to the steam phase in the drum.

In the following equations, subscripts are used to denote the phase and the location of the property or variable. The subscript s denotes the vapor (steam) phase, w denotes the liquid water phase, m denotes the metal part, g denotes saturated steam, f denotes saturated liquid, r denotes the risers or the absorbers in the solar field, d denotes the steam drum, t denotes the total system, rec denote the recirculation line, fw denotes the feedwater line.

4.2.1 Balance Equations on the Steam Drum

The mass balance on the steam drum is given by:

$$\frac{dM_{sd}}{dt} + \frac{dM_{wd}}{dt} = \dot{m}_{fw} + \dot{m}_r - \dot{m}_s - \dot{m}_{rec}, \qquad (4.12)$$

where M_{sd} is the mass of steam in the drum, M_{wd} is the mass of liquid water in the drum, $\dot{m}_{fw}$ is the feedwater mass flow, $\dot{m}_r$ is the mass flow exiting the absorber and into the steam drum, $\dot{m}_s$ is the steam mass flow out of the steam drum and $\dot{m}_{rec}$ is the recirculation mass flow.

The energy balance on the steam drum is given by the first law of thermodynamic assuming that the only work done in the control volume is $p\Delta V$ work.

$$
\begin{aligned}
dU &= \delta Q - \delta W + \Sigma \dot{m}h, \\
dH - d(pV) &= \delta Q - pdV + \Sigma \dot{m}h, \\
dH - Vdp - pdV &= \delta Q - pdV + \Sigma \dot{m}h, \\
dH - Vdp &= \delta Q + \Sigma \dot{m}h,
\end{aligned}
\qquad (4.13)
$$

$$
\begin{aligned}
&\frac{d(M_{sd}h_g)}{dt} + \frac{d(M_{wd}h_{wd})}{dt} + \frac{d(H_{md})}{dt} - V_d \frac{dp}{dt} \\
&= \dot{m}_{fw}h_{fw} + \dot{m}_r(\alpha_r h_{fg} + h_f) - \dot{m}_s h_g - \dot{m}_{rec}h_{rec},
\end{aligned}
\qquad (4.14)
$$

where h_g is the enthalpy of saturated steam, h_{wd} is the enthalpy of liquid water in the steam drum, H_{md} is the enthalpy of the steam drum metal, V_d is the volume of the steam drum, p is the pressure in the system, h_{fw} is the enthalpy of the feedwater, h_{fg} is the enthalpy of evaporation of water, h_f is the enthalpy of saturated liquid, h_{rec} is the enthalpy at the downcommer, and α_r is the steam mass quality at the exit of the absorber tube.

Expanding the equation and substituting the variables in terms of the state variables results in:

$$
\begin{aligned}
&M_{sd}\left(\frac{\partial h}{\partial p}\right)_{sat,g}\frac{dp}{dt} + h_g\frac{dM_{sd}}{dt} + M_{wd}\frac{dh_{wd}}{dt} + h_{wd}\frac{dM_{wd}}{dt} + C_{md}\left(\frac{\partial T}{\partial p}\right)_{sat}\frac{dp}{dt} - V_d\frac{dp}{dt} \\
&= \dot{m}_{fw}h_{fw} + \dot{m}_r(\alpha_r h_{fg} + h_f) - \dot{m}_s h_g - \dot{m}_{rec}h_{rec}.
\end{aligned}
$$
$$\qquad (4.15)$$

The volume control on the steam drum is given by:

$$V_d = V_{sd} + V_{wd},$$ (4.16)

which can be rewritten as:

$$V_d = M_{sd}v_g + M_{wd}v_{wd}.$$ (4.17)

In order to reduce the index of the Differential Algebraic Equation (DAE) system, we take the derivative of the control volume equation above. Hence the number of algebraic equations involved is reduced.

$$
\begin{aligned}
M_{sd}\left[\left(\frac{\partial v}{\partial p}\right)_h \frac{dp}{dt} + \left(\frac{\partial v}{\partial h}\right)_p \frac{dh_g}{dt}\right] + v_g \frac{dM_{sd}}{dt} + \\
M_{wd}\left[\left(\frac{\partial v}{\partial p}\right)_h \frac{dp}{dt} + \left(\frac{\partial v}{\partial h}\right)_p \frac{dh_{wd}}{dt}\right] + v_{wd}\frac{dM_{wd}}{dt} = 0.
\end{aligned}
$$ (4.18)

where v_g is the specific volume of saturated steam, v_{wd} is the specific volume of the liquid in the drum (not necessarily saturated!). Notice that $\frac{dv}{dt} = \left(\frac{\partial v}{\partial p}\right)_h \frac{dp}{dt} + \left(\frac{\partial v}{\partial h}\right)_p \frac{dh}{dt}$.

Now this equation can be further expanded by substituting $\frac{dh_g}{dt} = \left(\frac{\partial h}{\partial p}\right)_{sat,g} \frac{dp}{dt}$.

$$
\begin{aligned}
M_{sd}\left[\left(\frac{\partial v}{\partial p}\right)_h \frac{dp}{dt} + \left(\frac{\partial v}{\partial h}\right)_p \left(\frac{\partial h}{\partial p}\right)_{sat,g} \frac{dp}{dt}\right] + v_s \frac{dM_{sd}}{dt} + \\
M_{wd}\left[\left(\frac{\partial v}{\partial p}\right)_h \frac{dp}{dt} + \left(\frac{\partial v}{\partial h}\right)_p \frac{dh_{wd}}{dt}\right] + v_{wd}\frac{dM_{wd}}{dt} = 0.
\end{aligned}
$$ (4.19)

4.2.2 Balance Equations on the Absorber Tube

The mass balance in the absorber is:

$$\frac{dM_{sr}}{dt} + \frac{dM_{wr}}{dt} = \dot{m}_{rec} - \dot{m}_r,$$ (4.20)

where M_{sr} is the mass of steam in the absorber, M_{wr} is the mass of liquid water in the absorber. The energy balance on the absorber is:

$$
\begin{aligned}
M_{sr}\left(\frac{\partial h}{\partial p}\right)_{sat,g}\frac{dp}{dt} + h_g\frac{dM_{sr}}{dt} + M_{wr}\left(\frac{\partial h}{\partial p}\right)_{sat,f}\frac{dp}{dt} + h_f\frac{dM_{wr}}{dt} + C_{mr}\left(\frac{\partial T}{\partial p}\right)_{sat}\frac{dp}{dt} \\
= V_r\frac{dp}{dt} + \dot{Q}_{net} + \dot{m}_{rec}h_{rec} - \dot{m}_r(\alpha_r h_{fg} + h_f),
\end{aligned}
$$ (4.21)

where $\dot{Q}_{net}$ is the net power being supplied to the fluid in the solar field, which is equal to the solar energy input minus all the thermal losses in the solar field.

The control volume on the absorber gives the following equation:

$$M_{sr}\left[\left(\frac{\partial v}{\partial p}\right)_h \frac{dp}{dt} + \left(\frac{\partial v}{\partial h}\right)_p \left(\frac{\partial h}{\partial p}\right)_{sat,g} \frac{dp}{dt}\right] + v_g \frac{dM_{sr}}{dt} +$$
$$M_{wr}\left[\left(\frac{\partial v}{\partial p}\right)_h \frac{dp}{dt} + \left(\frac{\partial v}{\partial h}\right)_p \left(\frac{\partial h}{\partial p}\right)_{sat,f} \frac{dp}{dt}\right] + v_f \frac{dM_{wr}}{dt} = 0, \tag{4.22}$$

where v_f is the specific volume of the saturated liquid.

4.2.3 Balance Equations of the Vapor in the Steam Drum

The energy balance on the vapor in the steam drum is given by

$$M_{sd}\left(\frac{\partial h}{\partial p}\right)_{sat} \frac{dp}{dt} + h_g \frac{dM_{sd}}{dt} - M_{sd}v_s \frac{dp}{dt} = \alpha_r \dot{m}_r h_g - \dot{m}_s h_g + \dot{m}_e h_g, \tag{4.23}$$

where, $\dot{m}_e$ is the liquid evaporation mass rate.

4.2.4 Enthalpy of Fluid in the Recirculation Line

The enthalpy of the liquid in the recirculation line h_{rec} is an input parameter just like the flow rate $\dot{m}_{rec}$ is. In a small contained system, like a steam boiler, this enthalpy can be assumed to be equal to the liquid enthalpy h_{wd}. A more realistic assumption should take into account the design of the steam drum. In this system, the cold feedwater is actually fed to the steam drum in a location very close to the recirculation water intake. This means that feedwater will flow into the recirculation loop. Hence it is more reasonable to assume that h_{rec} is a mixture between the feedwater enthalpy and the liquid enthalpy.

$$h_{rec} = h_f - \frac{\dot{m}_{fw}}{\dot{m}_{rec}}(h_{wd} - h_{fw}). \tag{4.24}$$

4.2.5 Steam Mass Quality at the Absorber Outlet

The steam mass quality at the absorber outlet (α_r) depends on the recirculation mass flow rate ($\dot{m}_{rec}$), the enthalpy of the fluid getting into the absorber (h_{wd}), and the net amount of energy supplied to the fluid in the absorber ($\dot{Q}_{net}$).

$$\alpha_r = \frac{h_{rec} - h_f + \dot{Q}_{net}/\dot{m}_{rec}}{h_{fg}}. \tag{4.25}$$

The quality within the absorber can be assumed to develop linearly from α_o to α_r, where α_o is the quality of the fluid entering the absorber. α_o is

typically 0 but can also be negative when the fluid is subcooled, which is normally the case.

Introducing the term α_m proves to be helpful in simplifying the equations. α_m is the average quality across the absorber which is thus used to relate the total mass in the absorber M_r to the mass of the individual phases.

$$
\begin{aligned}
M_{sr} &= M_r \alpha_m. \\
M_{wr} &= M_r (1 - \alpha_m).
\end{aligned}
\tag{4.26}
$$

α_m is related to α_o and α_r by the simple formula which results from integrating the linear trend:

$$
\alpha_m = \frac{1}{2}(\alpha_r + \alpha_o).
\tag{4.27}
$$

α_o is calculated using the following equation:

$$
\alpha_o = \frac{h_{rec} - h_f}{h_{fg}}.
\tag{4.28}
$$

4.2.6 Absorber Outlet Connection to the Steam Drum

The amount of steam present under the liquid level is strongly related to the position of the two-phase flow pipe coming from the collector loop. Having the two-phase flow pipe above the liquid level will be advantageous to limit the swell-shrink effect induced by the steam bubbles. According to [4], the distribution of the steam under the liquid level in the drum will affect the swell-shrink phenomena. Hence, it is necessary to include in the model if a drum level is to be controlled.

Having the two-phase flow pipe above liquid level in the steam drum means that steam under liquid level will be present during flashing. This reduces the complexity of the model as it reduces the swell-shrink phenomena. However, it results in noticeable stratification in the steam drum between the vapor and liquid phases, which can be as high as $10^o C$. This reduces the effective storage capacity of the steam drum.

In conclusion, the position of the two phase flow pipe is an important parameter in the design of DSG systems and for sure is an essential consideration during modeling process.

4.2.7 Note on the application range

It is important to note in the above equations that the derivatives of the fluid properties are calculated for different regions. For example $\frac{dh}{dt} = \left(\frac{\partial h}{\partial p}\right)_{sat} \frac{dp}{dt}$ is evaluated for steam along the saturation boundary and hence is only expressed as function of pressure (for that the partial derivative has

a subscript sat). For other regions, the derivatives appear in pairs of two state variables, for example, $\frac{dh}{dt} = \left(\frac{\partial h}{\partial p}\right)_v \frac{dp}{dt} + \left(\frac{\partial h}{\partial v}\right)_P \frac{dv}{dt}$. Here, the partial derivatives are taken for p at constant v and for v at constant p. The later function is a general one and can be used for all regions, also along the saturation line. The former, however, is only valid on the saturation line. Notice however that $\left(\frac{\partial h}{\partial p}\right)_{sat} \neq \left(\frac{\partial h}{\partial p}\right)_v$.

Since some of the derivatives, for example $\left(\frac{\partial h}{\partial p}\right)_{sat}$, are evaluated along the saturation line, this limits the applicability of the model to that region. If the model is to be used for other purposes these properties should be extended. For example if the steam drum is flooded with liquid, saturation will end, adding more water will logically result in a rapid increase of pressure. In this mode in its current form the result will be that the solver assumes a negative mass of steam to account for the required decrease of specific volume. Hence, the model is limited to the saturation region only.

4.2.8 Numerical Solution

The set of equations: 4.12, 4.15, 4.19, 4.20, 4.21, 4.22, 4.23, 4.24 and 4.25 developed in previous sections represent a system of DAE. In order to reduce the index of the system and eliminate some of the algebraic variables, some equations have been differentiated when possible.

The number of unknowns in this system is 15 unknowns, which are namely: $p, M_{sd}, M_{wd}, M_{sr}, M_{wr}, v_s, v_w, v_{wd}, h_s, h_w, h_{wd}, \dot{m}_r, \alpha_r, \dot{m}_e, T_s$. The inputs to the system are: $\dot{m}_{fw}, h_f, \dot{m}_s, \dot{m}_{rec}, \dot{Q}_{net}$. In addition to the above mentioned 9 equations, 6 additional equations are needed to solve the system. These equations come from fluid state relations and are summarized as follows:

$$v_s = f_1(p), \tag{4.29}$$

$$v_w = f_2(p), \tag{4.30}$$

$$v_{wd} = f_3(p, h_{wd}), \tag{4.31}$$

$$h_s = f_4(p), \tag{4.32}$$

$$h_w = f_5(p), \tag{4.33}$$

$$T_s = f_6(p). \tag{4.34}$$

To simplify the solution, these functions are directly substituted in the aforementioned equations to reduce the system size.

This system of equations can be now solved using any DAE solver, in this work the $daspk$ algorithm has been used which is implemented in `Octave`.

4.2.9 Model Reduction and Simplification for MPC

In order to be able to use the model for MPC, it is simplified so that the optimization problem of the MPC algorithm is solved in a short time.

In the first simplification we assume that equilibrium between the phases inside the steam drum occurs fast enough to be ignored in the dynamics of the model, hence $h_{wd} = h_f$. As reported in [4] this is a reasonable assumption for drum steam boilers. This means that the balance equations of the vapor inside the steam drum are not needed and nor is the evaporated mass approximation.

Secondly we use the assumption of linear quality increase along the absorber. This results in a simplification of the balance equations in the absorber.

Since thermal equilibrium is assumed between the liquid and vapor in the steam, it is beneficial to treat the steam drum fluid mass as one variable called M_d and to introduce a mass vapor quality variable for the steam drum called α_d. Therefore the mass balance in the steam drum is given by:

$$\frac{dM_d}{dt} = \dot{m}_{fw} + \dot{m}_r - \dot{m}_s - \dot{m}_{rec}. \tag{4.35}$$

Equation 4.15 is rearranged to:

$$M_{sd}\frac{dh_g}{dt} + h_g\frac{dM_{sd}}{dt} + M_{wd}\frac{dh_f}{dt} + h_f\frac{dM_{wd}}{dt} + C_{md}\left(\frac{\partial T}{\partial p}\right)_{sat}\frac{dp}{dt} - V_d\frac{dp}{dt}$$
$$= \dot{m}_{fw}h_{fw} + \dot{m}_r(\alpha_r h_{fg} + h_f) - \dot{m}_s h_g - \dot{m}_{rec}h_{rec}. \tag{4.36}$$

The control volume on the steam drum is given by:

$$\frac{dM_d}{dt}\left[v_f + \alpha_d v_{fg}\right] + M_d\left[\frac{dv_f}{dt} + \frac{dv_{fg}}{dt}\alpha_d + dv_{fg}\frac{d\alpha_d}{dt}\right] = 0 \tag{4.37}$$

The mass balance in the absorber tube is given by:

$$\frac{dM_r}{dt} = \dot{m}_{rec} - \dot{m}_r, \tag{4.38}$$

where, M_r is the total fluid mass in the absorbers. The energy balance on the absorber is given by:

$$M_{sr}\frac{dh_g}{dt} + h_g\frac{dM_{sr}}{dt} + M_{wr}\frac{dh_f}{dt} + h_f\frac{dM_{wr}}{dt} + C_{mr}\frac{dT}{dt}$$
$$= V_r\frac{dp}{dt} + \dot{Q}_{net} + \dot{m}_{rec}h_{rec} - \dot{m}_r(\alpha_r h_{fg} + h_f). \tag{4.39}$$

Finally the control volume on the absorbers is given by:

$$\frac{dM_r}{dt}\left[v_f + \alpha_m v_{fg}\right] + M_r\left[\frac{dv_f}{dt} + \frac{dv_{fg}}{dt}\alpha_m + dv_{fg}\frac{\alpha_m}{dt}\right] = 0. \qquad (4.40)$$

The set of Equations 4.35, 4.36, 4.37, 4.39 and 4.40 represent a system of DAE with five variables (states) namely: M_d, M_r, p, α_d and α_m, and two inputs namely: $\dot{m}_{fw}$ and $\dot{m}_s$.

Notice that $M_{wd} = (1 - \alpha_d)M_d$, $M_{sd} = \alpha_d M_d$, $M_{wr} = (1 - \alpha_m)M_r$ and $M_{sr} = \alpha_m M_r$. Also notice that $\dot{m}_r$ is replaced by Equation 4.38.

The system variables can be arranged in a vector called the state vector x:

$$x = \begin{bmatrix} x_0 \\ x_1 \\ x_2 \\ x_3 \\ x_4 \end{bmatrix} = \begin{bmatrix} p \\ M_d \\ \alpha_d \\ M_r \\ \alpha_m \end{bmatrix}, \qquad (4.41)$$

while the system inputs are arranged in the inputs vector u as follows:

$$u = \begin{bmatrix} u_0 \\ u_1 \end{bmatrix} = \begin{bmatrix} \dot{m}_s \\ \dot{m}_{fw} \end{bmatrix}. \qquad (4.42)$$

4.2.10 Analysis of Model Uncertainty

The model developed is used by the MPC controller to calculate actuator actions. In the MPC control strategy the two main control actions are the determination of the suitable feedwater mass flow rate ($\dot{m}_{fw}$) and the steam mass flow rate ($\dot{m}_s$).

For the uncertainty analysis here, steady state conditions are assumed. Therefore the model equation presented before are reduced to their steady state forms.

It can be shown that the steady state model of the system can be boiled down to two main equations, a mass balance on the system:

$$\dot{m}_{fw} = \dot{m}_s, \qquad (4.43)$$

and an energy balance equation:

$$\dot{Q}_{net} = \dot{m}_s h_g - \dot{m}_{fw} h_{fw}. \qquad (4.44)$$

Where $\dot{Q}_{net} = \dot{Q}_{solar} - \dot{Q}_l$. Using Equation 4.43 to substitute $\dot{m}_{fw}$ by $\dot{m}_s$ in Equation 4.44 and then rearranging in terms of $\dot{m}_s$:

$$\dot{m}_s = \frac{\dot{Q}_{net}}{h_g - h_{fw}}. \qquad (4.45)$$

Based on Equation 4.45 the uncertainty in determining $\dot{m}_s$ is related to the uncertainty of the evaluation of $\dot{Q}_{net}$ and the enthalpies h_g and h_{fw}. Since the uncertainty in $\dot{Q}_{net}$ is much larger, the uncertainty in the evaluation of enthalpies is neglected.

The uncertainty in $\dot{Q}_{net}$ was found in Section 4.1.2 to range between $\pm 12.4\%$ and $\pm 18.9\%$ depending on the DNI measurement used, which is also the uncertainty in $\dot{m}_s$ and $\dot{m}_{fw}$.

The uncertainty in the measurement of the actual steam mass flow rate is $\pm 2.0\%$ as given by the manufacturer. While the uncertainty in the measurement of feedwater mass flow rate is $\pm 0.2\%$ for the sensor at the RamPharma plant and it is undetermined for the test sensor used in the Hochdorf facility. The uncertainty in measuring the recirculation mass flow rate ($\dot{m}_{rec}$) is $\pm 0.26\%$ as discussed in Section 4.1.2 .

Pressure measurement uncertainty is less than $\pm 1.0\%$ as given by the manufacturer. While the measurement uncertainty of level measurement is $\pm 3 mm$. Note that the uncertainty in determining the volume of liquid in the steam drum is depending on the fill level.

4.3   Development of Flow Patterns Maps in DSG Mode

In this section flow pattern maps for the LFC plant are produced. The maps are based on literature for flow boiling in horizontal tubes. These maps represent a helpful tool for DSG system designers. Using these maps one can predict the expected flow regime at several points in the solar field and at different power levels.

In direct steam generation a major part of the solar field has a two phase flow. Two phase flows have several possible flow regimes, which depend on the fluid properties, flow velocities of the two phases, and the flow geometry. Depending on the local flow regime, the local heat transfer coefficient and the pressure drop are determined.

The two phase flow pattern in the absorber tube presents a challenge to the stability and safety of the DSG system, that is why it is important to determine the expected flow patterns in the absorber tube. The recirculation flow controller aims at maintaining a favorable flow regime in the absorber whenever possible.

In this section an overview of a method developed at EPFL and used to predict the two phase flow regimes for flow boiling in horizontal pipes is presented. This method is then used to generate a specialized map to predict two phase flow in the absorber tube of the solar field at different locations and at different flow rates and power ranges. These maps are used for the hydraulic design of DSG systems as they present a tool to assess several designs from flow regime point of view.

Two-phase flow in a horizontal tube are similar to vertical tubes but are additionally affected by gravity that tends to stratify the phases, forcing the liquid to the bottom of the tube and the gas to go on top. [64]

At low gas and liquid velocities, there is complete separation between the phases and an undisturbed horizontal interface is present, this is called stratified flow. Stratified flow transitions to Wavy flow if the gas velocity increases. Waves start forming on the interface between the phases. The amplitude of the waves depend on the velocity slip between the phases. As the slip increases, the waves may reach the top of the tube leaving a thin film of liquid. This is called Intermittent flow which includes Plug and Slug flows as subcategories. At even higher gas velocities, the liquid forms a continuous annular film around the inner wall of the tube surrounding a gas core that moves at high velocity. At very high flow velocities all the liquid is stripped from the wall and is entrained as small droplets in the gas phase [64].

Figure 4.6 depicts the development of the flow pattern in a heated pipe as the quality α increases from 0 to 1. Starting from bubbly flow at low α up to mist flow at high α.

The transition between different flow patterns is determined by many factors. Unlike for single phase flow where the flow condition is determined by a single number, there isn't a universal equation to determine the transitions between different flow patterns. Typical flow pattern maps have different equations for different transition boundaries.

Moreover maps are typically developed for particular situations, for example adiabatic flows, or evaporating flows, or condensing flows. Hence the applicability of the flow pattern maps depends on the particular situation.

For example many flow pattern maps developed in the past are made for adiabatic conditions and are often extrapolated to diabatic systems [64].

According to Brennen [12] several points have to be taken into account when using flow pattern maps:

- Many maps are not dimensionless, so the flow patterns might differ for different geometries. And although many workers tried to get dimensionless relations but transitions and boundaries might depend on different and varying dimensionless numbers.

- It is not yet established when does multiphase flow really develop hydraulically. As compared to single phase flow for example which is considered fully developed after an entrance length of 30 to 50 pipe diameters, such a number for multiphase flow does not exist.

- Finally, the implicit assumption that there exists a certain flow pattern for a set of fluids and flow rates and conditions is simply not confirmed.

Here, we adopt a flow pattern map which was suggested by Kattan, Thome and Favrat [41, 42, 40] as they appear in [64]. The map is a modification of the map suggested by Steiner ([61]). This map is developed specifically for boiling flows in horizontal tubes and it also includes the effect of heat flux on the flow pattern. Hence it is very close to this application for use in solar direct steam generation.
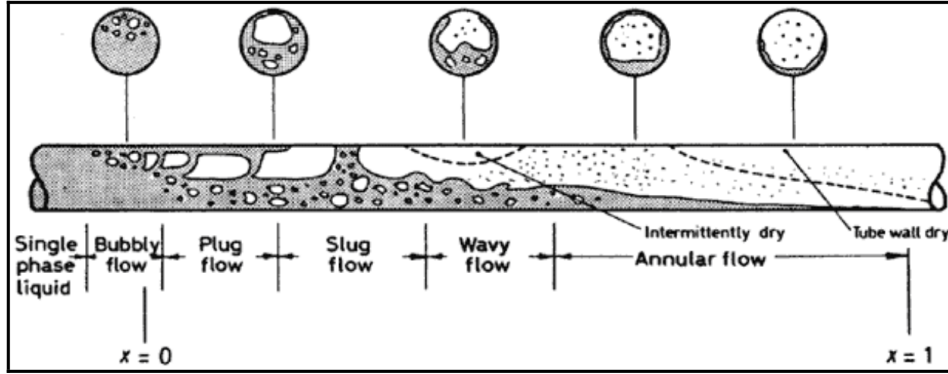
Figure 4.6: Flow patterns during evaporation in a horizontal tube including cross-sectional views of flow structure. Courtesy of [20] cited in [64].

The transition regions between different flow patterns are defined as follows[64] :

$$
\Phi_{wavy} = 50 - 75e^{-\frac{(\alpha^2 - 0.97)^2}{\alpha(1-\alpha)}}
$$
$$
+ \left[\frac{16A_{Gd}^3 g D_i \rho_f \rho_g}{\alpha^2 \pi^2 (1 - (2H_{Ld} - 1)^2)^{\frac{1}{2}}} \left[\frac{\pi^2}{25H_{Ld}^2} (1-\alpha)^{-F_1(q)} \left(\frac{We_f}{Fr_f} \right)^{-F_2(q)} + 1 \right] \right]^{\frac{1}{2}},
$$
(4.46)

where, Φ is the mass velocity or mass flux $(\frac{kg}{m^2 s})$, α is the mass vapor quality, D_i is the inner pipe diameter, g is the gravitational acceleration, ρ_g is the density of vapor, ρ_f is density of liquid.

Here the non-dimensional empirical exponents are $F1$ and $F2$ include the effect of heat flux [64]:

$$
F_1(q) = 646.0 \left(\frac{q}{q_{DNB}} \right)^2 + 64.8 \left(\frac{q}{q_{DNB}} \right),
$$
$$
F_2(q) = 18.8 \left(\frac{q}{q_{DNB}} \right) + 1.023,
$$
(4.47)

where q is the heat flux on the tube $(\frac{W}{m^2})$, and q_{DNB} is the departure from nucleate boiling heat flux given by:

$$
q_{DNB} = 0.131 \rho_f^{\frac{1}{2}} h_{fg} [g(\rho_f - \rho_g)\sigma]^{\frac{1}{4}},
$$
(4.48)

where h_{fg} is the heat of evaporation and σ is the surface tension of the liquid. For the evaluation of the surface tension with respect to temperature we use the equation presented by Vargaftik et al. [68]:

$$\sigma = 235.8 \times 10^{-3} \left(\frac{T_c - T^{1.256}}{T_c} \right) \left(1 - 0.625 \frac{T_c - T}{T_c} \right), \tag{4.49}$$

where $T_c = 647.15K$ and T is in Kelvin.

The transition to mist flow depends on the ratio of the Froude number (Fr_f) to the Weber number (We_f) [64]. Froude number is the ratio of inertia to surface tension while the Weber number is the ratio of inertia to gravity forces.

$$\Phi_{mist} = \left[\frac{7680 A_{Gd}^2 g D_i \rho_f \rho_g}{\alpha^2 \pi^2 \xi_{PH}} \left(\frac{Fr_f}{We_f} \right) \right]^{\frac{1}{2}}, \tag{4.50}$$

$$\Phi_{strat} = 20\alpha + \left[\frac{226.3^2 A_{Ld} A_{Gd}^2 \rho_g (\rho_f - \rho_g) \mu_f g}{\alpha^2 \pi^3 (1 - \alpha)} \right]^{\frac{1}{3}}, \tag{4.51}$$

μ_f is the dynamic viscosity of liquid, μ_g is the dynamic viscosity of vapor

$$\Phi_{bubbly} = \left[\frac{256 A_{Gd} A_{Ld}^2 D_i^{1.25} \rho_f (\rho_f - \rho_g) g}{0.3164 (1 - \alpha)^{1.75} \pi^2 P_{id} \mu_f^{\frac{1}{4}}} \right]^{\frac{1}{1.75}}. \tag{4.52}$$

The Weber-Froude ratio is given by:

$$\frac{Fr_f}{We_f} = \frac{g D_i^2 \rho_f}{\sigma}, \tag{4.53}$$

and the friction factor is:

$$\xi_{PH} = \left[1.138 + 2log_{10} \left(\frac{\pi}{1.5 A_{Ld}} \right) \right]^{-2}. \tag{4.54}$$

Now the transition between intermittent flow and annular flow is assumed to occur, when the Martenelli parameter $X_{martinelli}$ is equal to 0.34, where:

$$X_{martinelli} = \left(\frac{1 - \alpha}{\alpha} \right)^{0.875} \left(\frac{\rho_g}{\rho_f} \right)^{\frac{1}{2}} \left(\frac{\mu_f}{\mu_g} \right)^{0.125}, \tag{4.55}$$

which provides the vapor quality above which annular flow occurs as:

$$\alpha_{annular} = \left(\left[0.2914 \left(\frac{\rho_g}{\rho_f} \right)^{\frac{-1}{1.75}} \left(\frac{\mu_f}{\mu_g} \right)^{\frac{-1}{7}} \right] + 1 \right)^{-1}. \tag{4.56}$$

A modification on the original Kattan-Thome-Favart map has been proposed by Thome and El Hajal [64, 65]. The modified map uses the Rouhani-Axelsson void fraction equation avoiding the iterations needed before to

calculate the transition boundaries. The cross sectional void fraction (γ) is given by:

$$\gamma = \frac{\alpha}{\rho_g}\left[(1 + 0.12(1 - \alpha))\left(\frac{\alpha}{\rho_g} + \frac{1 - \alpha}{\rho_f}\right) + \frac{1.18(1 - \alpha)(g\sigma(\rho_f - \rho_g))^{\frac{1}{4}}}{\Phi\rho_f^{\frac{1}{2}}}\right].$$

(4.57)

Using Equation 4.57 for the void fraction (γ), the values A_{Ld} and A_{Gd} are evaluated using [64] :

$$A_{Ld} = \frac{A(1 - \gamma)}{D_i^2},$$

$$A_{Gd} = \frac{A\gamma}{D_i^2}.$$

(4.58)

The dimensionless liquid height H_{Ld} and the length of liquid interface are expressed as a function of the stratified angle θ_{strat} [64] and read to:

$$H_{Ld} = 0.5\left(1 - cos\left(\frac{2\pi - \theta_{strat}}{2}\right)\right),$$

$$P_{id} = sin\left(\frac{2\pi - \theta_{strat}}{2}\right),$$

(4.59)

where θ_{strat} is given by:

$$\theta_{strat} = 2\pi$$

$$- 2\left[\pi(1 - \gamma) + \left(\frac{3\pi}{2}\right)^{\frac{1}{3}}\left(1 - 2(1 - \gamma) + (1 - \gamma)^{\frac{1}{3}} - \gamma^{\frac{1}{3}}\right)\right]$$

(4.60)

$$- \frac{\gamma}{100}(1 - \gamma)(1 - 2(1 - \gamma))[1 + 4((1 - \gamma)^2 + \gamma^2)].$$

The transition boundaries have been calculated for the two-phase flow in the absorber tubes of the solar field using the above equations. This has been done for several collector powers and volumetric flow rates in the absorber tube, resulting in the flow pattern maps in Figure 4.7 and Figure 4.8.

In these flow pattern maps, the y-axis represents the power absorbed by the fluid up to the point along the absorber section where we wish to know the flow pattern. For example, if we operate at $10bar_g$ and we have a total power of $600kW$, and we wish to know the flow pattern at the exit when flow rate is $2.0m^3/hr$, then it will be annular. To know the flow pattern after the first third of the absorber we have to check the flow pattern at $200kW$ which will then be wavy.

Notice that the total power and the flow rates refer to absorber tubes in series. So if there are hydraulically parallel strings the power is meant for each single one of them.

Figure 4.7 depicts the expected flow pattern map for operation at $10bar_g$, as can be seen, the flow is mostly wavy in the power range up to $400kW$. Annular flow is only achieved above the $400kW$ threshold. Reducing the operating pressure results in a favorable situation as it increases the volume of the vapor and hence increases the velocity. As seen in Figure 4.8 this results in annular flow to appear at powers lower than $400kW$ and also an enlarged mist flow region.

The flow pattern maps in Figure 4.8 and Figure 4.7 have been generated using an `Octave` code which is adaptable for several conditions. These maps are helpful in the design process of DSG systems as they offer a quick insight into the expected flow regimes at different locations of the solar field and at different power levels. The experimental verification of these maps can be achieved using a direct measurement by means of a WMS.
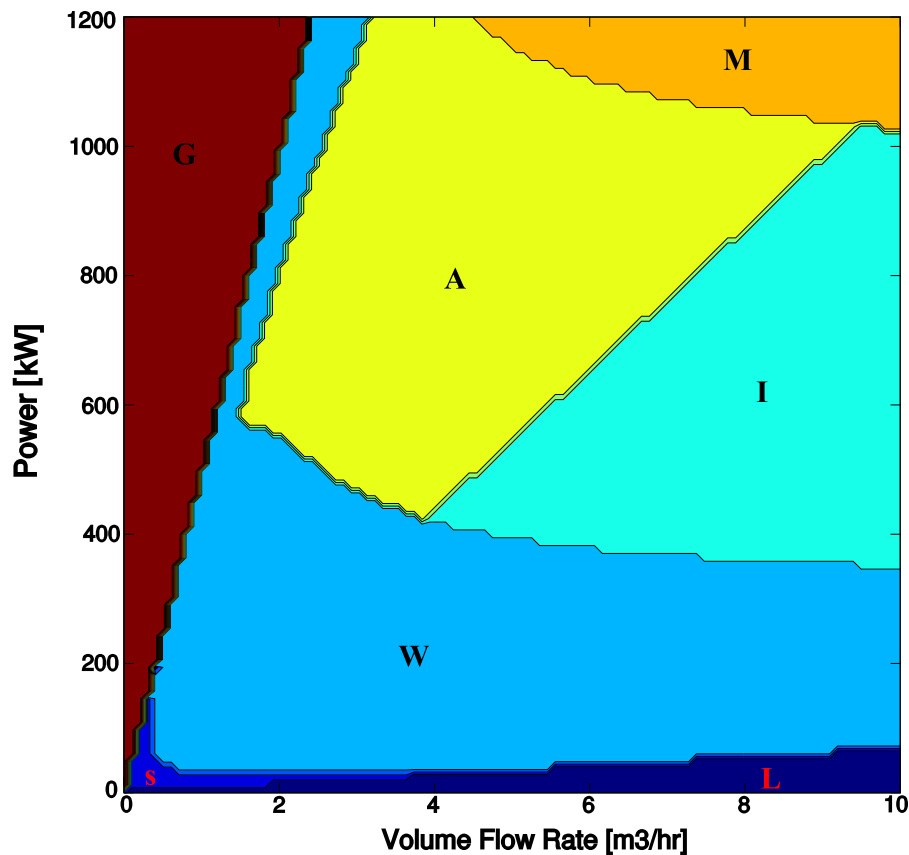
Figure 4.7: Flow pattern map adapted for direct steam generation using Schott PTR70 ($D_i = 66.0mm$) absorber pipes. $T_{in} = 178^oC$, $p = 10.0bar_g$. **Abbreviations are, L: subcooled Liquid flow, S: Stratified flow, W: Wavy stratified flow, I: Intermittent flow, A: Annular flow, M: Mist flow and G: gas, superheated steam flow.**
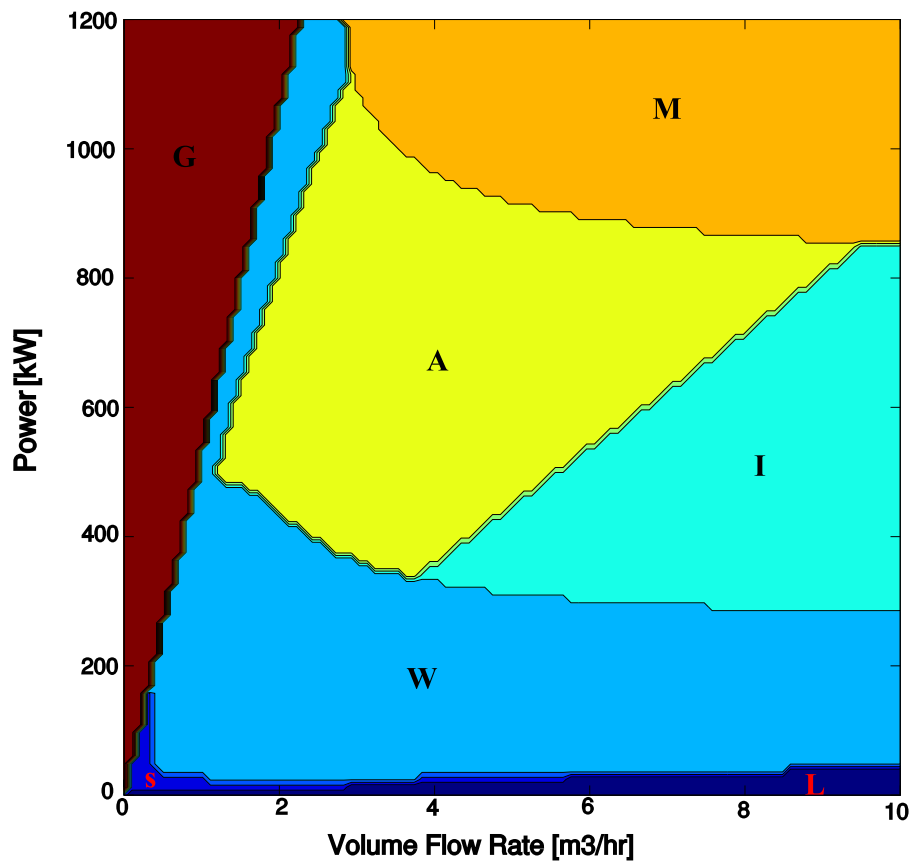
**Figure 4.8: Flow pattern map adapted for direct steam generation using
Schott PTR70 ($D_i = 66.0mm$) absorber pipes.** $T_{in} = 155^oC$**,** $p = 5.0bar_g$**. Ab-
breviations are, L: subcooled Liquid flow, S: Stratified flow, W: Wavy strati-
fied flow, I: Intermittent flow, A: Annular flow, M: Mist flow and G: gas, super-
heated steam flow.**

Chapter 5

Control Strategies for Single Phase Flow

PID control theory is based on the assumption that the system to be controlled is a Linear Time-Invariant (LTI) system. The model in Equation 4.8 provides valuable insight into system dynamics and shows that the system under study is neither linear nor time invariant.

The following properties can be inferred from the model:

- System input and output are not linearly related. The input to the system is F, which is the reciprocal of manipulated parameter, the mass flow rate. This is in violation of the linearity assumption.

- The system time constant τ is defined as $\frac{C}{\dot{m}_{rec}cp}$. This implies that the system time constant is actually varying with the system input. This violates the time-invariance assumption.

- The control system we are dealing with has one control input, which is the recirculation mass flow ($\dot{m}_{rec}$), and one output, which is the outlet temperature (T_o). Any other inputs that affect system output are considered disturbances from control point view. Based on that, several disturbances can be identified. Some disturbances are measurable while others are not:

  1. Solar irradiation (DNI)
  2. Sun position
  3. Primary and secondary mirrors reflectivity change by time due to soiling
  4. Absorptivity of the absorber tube
  5. Angle of incidence effects
  6. Ambient temperature

   7. Inlet temperature

- The system suffers from a pure time delay, or dead time (κ). This dead time changes with the manipulated parameter; the mass flow rate.

- Fluid and material properties like water density, specific heat and absorber heat capacity are functions of temperature at the inlet and the outlet. This can be significant if the whole temperature range is considered (from 20^oC to 200^oC).

- A model for the flow controller that controls pump speed to achieve the desired mass flow rate is not included. Typically the time constant of such controller is an order of magnitude smaller than the main controller, however depending on the type of pump and flowmeter it can be significant.

- Dynamic change of thermal losses of the absorber is not included in the dynamic model, although thermal losses are dependent on the controlled parameter T_o. The combination of thermal losses with solar input as a single parameter (net heat input) can only be justified if thermal losses are small.

- The change in the stored energy in the absorber tube is a function of the mean absorber tube temperature (absorber tube temperature changes from the inlet to the outlet). However, outlet temperature is actually used in the model. This can be justified since the change in mean absorber temperature dT_m is close to the change of the outlet temperature T_o, and also the change in the absorber stored energy is relatively small (less than 5% when the collector is in operation).

- The net solar energy that reaches the absorber is also not constant and changes continuously because of changes of solar irradiation itself, and because of sun position changes.

- Further nonlinearities are added by actuators (pumps and control valves), mainly the operation range of the pump.

The aforementioned properties of the controlled system makes it difficult for conventional fixed-parameter PID controllers to deliver adequate control action. Therefore, the use of a conventional PID controller will require either controller detuning to attain stability, which results in sluggish response, or tight tuning which results in oscillatory operation. [16]

Figure 5.1 presents the results of a test performed at the testing facility in Hochdorf near Freiburg. In the upper part of the figure the outlet temperature of the solar field is depicted, it represents the controlled variable in single phase flow systems. The PID controller tries to maintain the

controlled variable as close as possible to the setpoint (also shown in the figure). The Inlet temperature acts as a system disturbance. The lower part of the figure depicts the mass flow rate which represents the manipulated parameter that the controller uses to adjust the outlet temperature.

During this test the setpoint temperature is changed several times. It can be seen that this controller is not able to provide stable operation. The decay ratio was 1.25 which means that the system is unstable (decay ratio above 1.0 means the system is unstable). This is also evident from the sustained oscillations in the collector outlet temperature. The maximum overshoot of the controlled parameter reached $2.75^oC \pm 0.15^oC$ with a high POR of 91%.

As mentioned earlier, the unsatisfactory performance of the PID controller in this type of problems is expected. PID control analysis is typically applied on LTI systems or systems which can be approximated as such, whereas the system we are dealing with here, is neither linear nor time invariant.
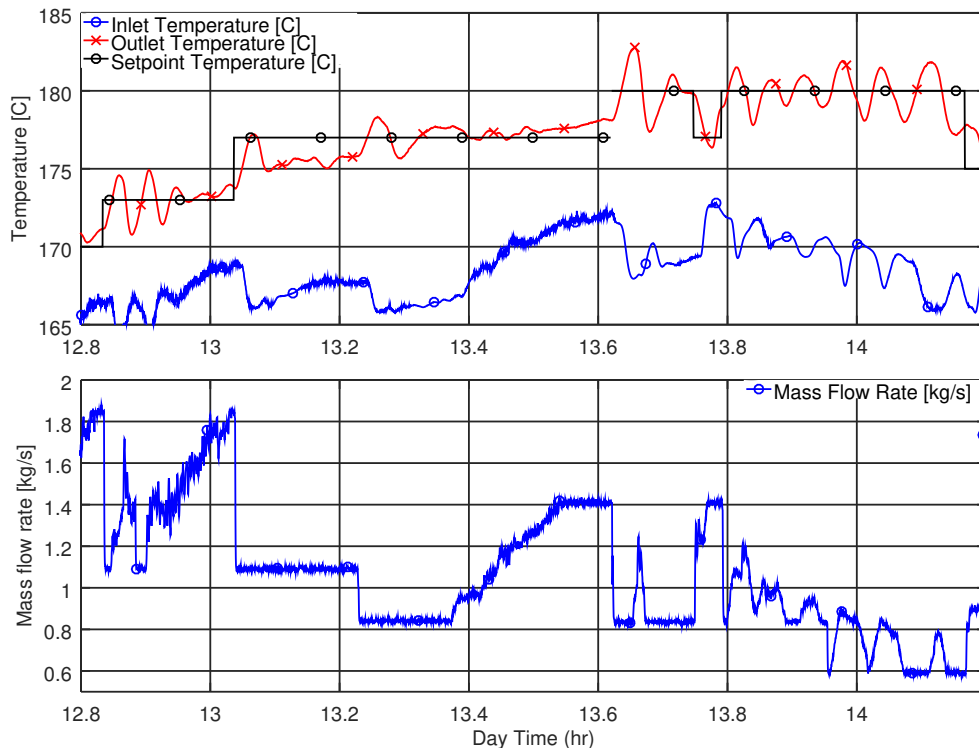
Figure 5.1: Temperature control using a conventional PID controller. (Testing facility: Hochdorf).

5.1 PID Controller with Parallel Feed-forward

Feed-forward control can be classified as a model-based control method since a model is typically used to account for the effects of measured disturbances on the system performance. Feed-forward controllers are extensively used in the industry [15, 16, 51]. Often, feed-forward controllers are combined with feedback controllers, see Figure 5.2. The feedback loop accounts for any deviation that the feed-forward controller fails to account for.

The feed-forward serves two main purposes (i) rejection of measurable disturbances (mainly inlet temperature and solar power) and (ii) linearizing the plant about the operating point. Without feed-forward the feedback controller would have to operate under widely varying conditions. Introducing the feed-forward controller however, the feedback controller will be only required to correct for changes that the feed-forward model failed to account for.

Figure 5.2 depicts the feed-forward compensator in parallel with the PID controller. The outputs of the PID and feed-forward controller are added together to make the control signal as shown in Equation 5.1:

$$\underbrace{\dot{m}_{controller}}_{\text{Controller Output}} = \underbrace{\dot{m}_{FFWD}}_{\text{Feed Forward Term}} + \underbrace{\dot{m}_{PID}}_{\text{PID terms}}, \tag{5.1}$$

where $\dot{m}_{controller}$ is the mass flow rate value sent from the controller to the process, $\dot{m}_{FFWD}$ is the feed forward controller term, and $\dot{m}_{PID}$ is the PID controller term.

The feed-forward controller calculates the required mass flow rate using a system model. From Equation 4.2, the feed forward mass flow rate can be calculated as follows:

$$\dot{m}_{FFWD} = \frac{\dot{Q}_{net} - dE_{abs}/dt}{c_p(T_r - T_i)}. \tag{5.2}$$

The use of this model requires the knowledge of inlet temperature, change in absorber internal energy and the net power transferred to the fluid in the absorber, which is in turn a function of direct solar irradiation (DNI), mirror reflectivity, overall optical efficiency, sun position and thermal losses.

Equation 5.2, in its current form however, often results in unwanted reactions and instability. Looking at the denominator, if the setpoint temperature T_r approaches the inlet temperature T_i then we have a division by a small number resulting in a very high flow rate.

Moreover, unphysical reactions are obtained if T_i is higher than T_r, resulting in negative mass flow in Equation 5.2.

Practically, under these conditions, the system is overheating and the situation is beyond the control of the mass flow controller. The correct action from the mass flow controller is to increase the flow rate to the maximum so that the temperature increase in inlet temperature is driven to a minimum. However, since a negative flow rate is calculated the pump will actually shutdown and the system rapidly overheats. This action from the feed-forward controller is a result of the nonlinearity of the system. To avoid such problems the feed-forward term can be linearized or limited to a suitable safe range.
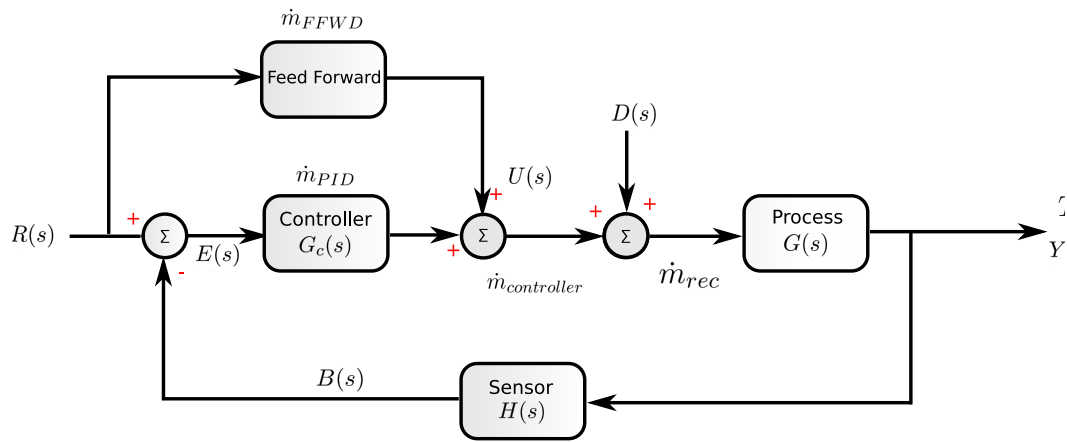
Figure 5.2: Control block diagram of PID controller with parallel feed-forward loop.

Camacho et al. [15] suggested a linearized model with experimentally determined constants to overcome these issues:

$$\dot{m}_{FFWD} = \frac{0.7869I - 0.485(T_r - 151.5) - 80.7}{T_r - T_i},$$ (5.3)

where I is DNI in (kW/m^2).

In the testing facility another formula exhibited good results. Again the coefficients are determined experimentally by trial and error.

$$\dot{m}_{FFWD} = 0.85 \frac{\dot{Q}_{net} - dE_{abs}/dt}{c_p(T_r - T_i)} + 0.15\dot{m}_{rec} + 0.2.$$ (5.4)

In Equation 5.4, the original equation 5.2 is modified to increase stability. The term $0.15\dot{m}_{rec}$ is added. The 0.2 biases the system towards higher flow rate and hence helps in reducing overheating. In situations where the denominator is close to zero, the flow rate calculated from Equation 5.4 is monitored. If the flow is negative, overheating is detected and the flow rate is raised to a high value.

5.2 Using past Data for Calculating the Feed-Forward Term

The term $\dot{Q}_{net}$ in Equation 5.4 represents the net energy absorbed by the absorber tube. Evaluating this term requires an optical model of the collector, a heat loss model and also the knowledge of DNI. DNI measurements are not always available, first because its costly and second since it requires continuous maintenance of the measurement equipment.

To avoid using collector models and DNI measurement, one can use past measurements to infer the $\dot{Q}_{net}$ term. This can be justified since the process is relatively slow (time constants of at least 30 seconds for the smallest systems). The net solar input to the (HTF) can be estimated based on past data of inlet and outlet temperatures and mass flow rate. The result is then used for the current time step to calculate the feed-forward term. This can be further enhanced by taking a weighted moving average of the past data.

$$\bar{\dot{Q}}_f = \sum_{n=0}^{n=k} \omega_n \dot{Q}_f(t - n\Delta t), \tag{5.5}$$

where $\dot{Q}_f = \dot{Q}_{net} - dE_{abs}/dt$, k is the number of time steps, Δt is the time step length, and ω_n is the weight at each time step which can be tuned experimentally. Hence the feed-forward term can be reformulated to:

$$\dot{m}_{rec} = \frac{\bar{\dot{Q}}_f}{c_p(T_r - T_i)}. \tag{5.6}$$

Fluid properties such as density and specific heat are calculated based on the current fluid conditions, typically a mean fluid temperature T_{fm} is used for that purpose.

This method for calculating the feed-forward term although very convenient, can be unstable. This is because the calculation of the feed-forward term depends both on the controlled (T_o) and manipulated ($\dot{m}_{rec}$) parameters. While the first changes slowly (Temperature) the later changes much faster (mass flow rate).

A change in mass flow will result in an instantaneous change in the calculated $\dot{Q}_f$. This error will affect the feed-forward controller and result in unstable control until the flow rate reaches a minimum or a maximum.

This problem is mitigated using longer moving average time windows and some smoothing of the calculated $\bar{\dot{Q}}_f$.

Additionally, the calculation of the feed-forward term is actually also introducing undesirable feedback paths since it uses the controlled parameter as part of the calculation. This can affect the performance of the PID controller.

Figure 5.3 depicts an implementation of the controller in an operational system. In the figure, the top graph presents the measured temperature signals from collector inlet and collector outlet (controlled variable) along with the temperature setpoint. The bottom graph depicts the manipulated parameter, the mass flow rate.

The outlet setpoint temperature of the controller is set to 180^oC. The feed-forward control term is slightly adjusted compared to that in Equation 5.4 and reads to:

$$\dot{m}_{FFWD} = 0.85\frac{\bar{\dot{Q}}_f}{c_p(T_r - T_i)} + 0.1. \tag{5.7}$$

In this controller $\bar{\dot{Q}}_f$ is calculated using a weighted moving average over a 60 seconds time window. The PID parameters for the controller where, $K_p= 0.2$, $t_i= 200s$ and $t_d= 20s$.

The controller presents a good damped response with a maximum overshoot of less than 2^oC and a POR of only 4%. However, the oscillatory response seen in the outlet temperature is undesirable where the decay ratio was high reaching 0.75. The Root Mean Square Error (RMSE) in setpoint tracking between $t = 10.5hr$ and $t = 14.5hr$ was only $\pm0.54^oC$. Note that temperature measurement uncertainty is $\pm0.15^oC$.

Figure 5.4 presents the terms of the PID Parallel feed-forward controller. It can be seen from the figure that the main adjustment is done by the feed-forward term (depicted in blue, bottom graph),which almost coincides with the actual flow rate (depicted in red, bottom graph).

At quasi static conditions of DNI and Inlet temperature, using past data to calculate $\dot{Q}_f$ works well, however, the controller can become oscillatory and unstable under certain conditions as shown in Figure 5.4. The reason for the instability comes from the implicit feedback link between the calculated feed-forward term and the outlet temperature.

A better evaluation of the $\dot{Q}_f$ can be done using a moving-average with longer time window. This, however, results in a slower response and higher overshoot. Another possibility is calculating $\dot{Q}_f$ using an optical model independent of the controlled and manipulated parameters. This is described in Section 5.3.
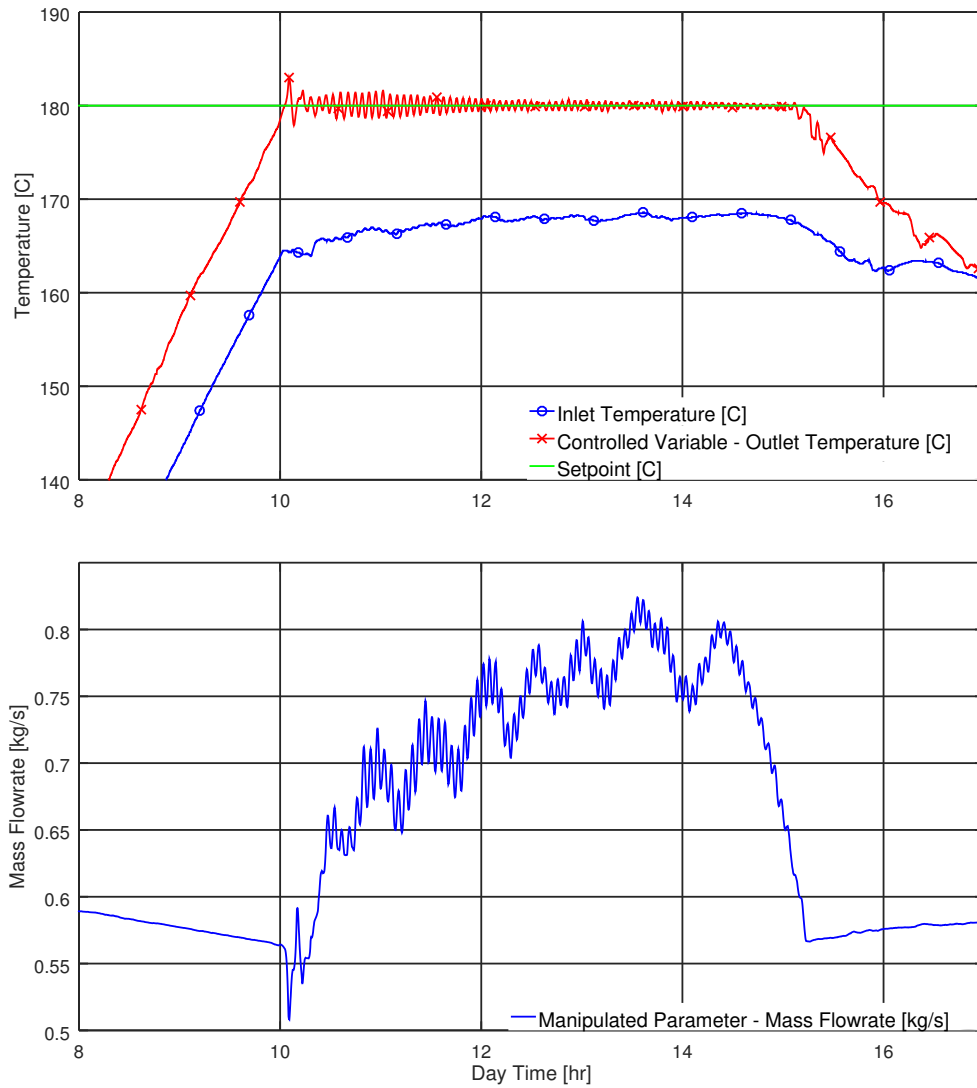
Figure 5.3: Measured temperature control using a PID with parallel feed-forward controller. Feed-forward controller calculated using past data. Top: Temperature evolution at T_o as a function of time. Bottom: The manipulated parameter, mass flow rate. (Testing facility: Qatar Science and Technology Park).
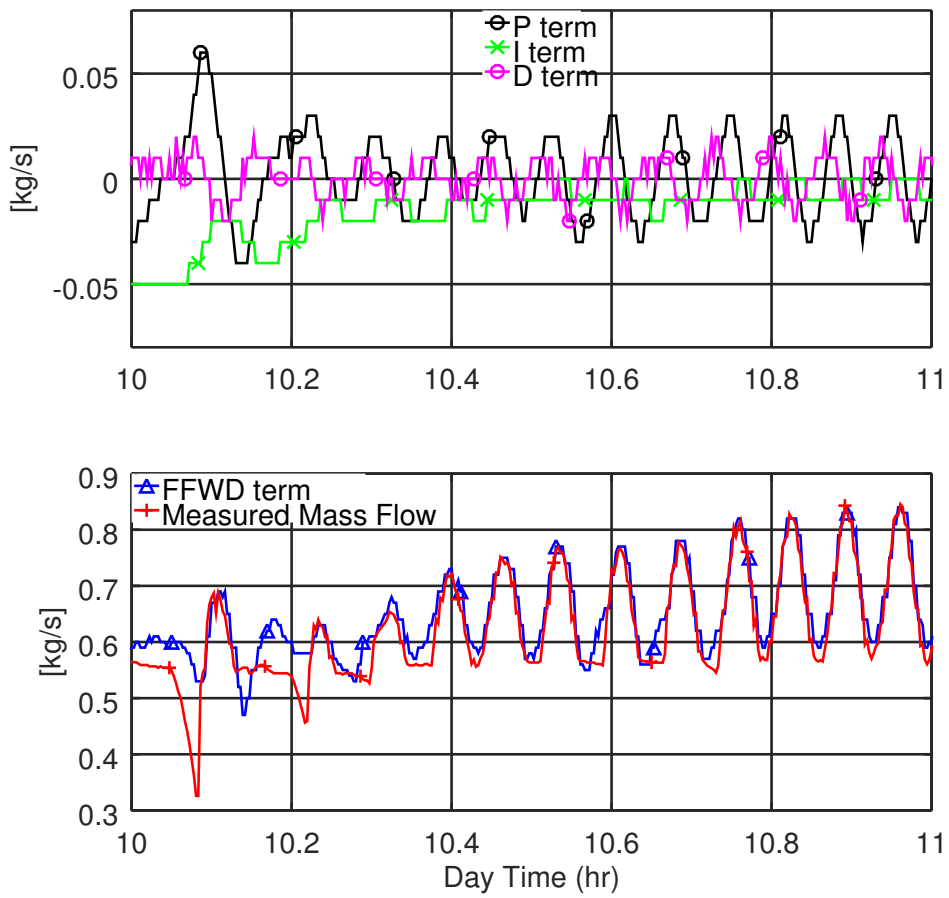
Figure 5.4: Measured temperature control using a PID with parallel feed-forward controller. Controller individual terms are depicted. (Testing facility: Qatar Science and Technology Park).

5.3 Using an Optical Model for Calculating the Feed-Forward Term

Using an optical model for calculating $\dot{Q}_f$ provides two main advantages for the calculation of the feed forward term. Firstly, it eliminates the implicit link between the feed forward term and the controlled parameter and thus enhancing system stability. Secondly, it provides proactive control action since the controller reacts directly when solar irradiation changes before the controlled parameter actually changes.

Practically, however, an optical model requires the measurement of DNI, which can be expensive and also not very reliable. In addition, an optical model assumes perfect conditions of the reflecting surfaces.

In absence of such a guarantee or a way to quantify the degradation in the expected power, the PID controller will have to compensate for the model error.

Here, the feed-forward mass flow rate term in Figure 5.2 is calculated using an optical power model. Similar to the calculation in Equation 5.2, the required flow rate is calculated as follows:

$$\dot{m}_{rec} = \frac{\dot{Q}_{solar} - \dot{Q}_l}{c_p(T_r - T_i)}.$$

(5.8)

The solar power input to the collector ($\dot{Q}_{solar}$) is calculated using Equation 2.5 and collector thermal losses ($\dot{Q}_l$) are calculated using Equation 2.9.

The feed-forward control term is slightly adjusted similar to what was done in Equation 5.7, the adjustment was done during operation:

$$\dot{m}_{rec} = 0.90\frac{\dot{Q}_{solar} - \dot{Q}_l}{c_p(T_r - T_i)} - 0.07.$$

(5.9)

Figure 5.5 depicts the results from using the optical model for calculating the feed forward term. It can be seen that the controller provides fast heat up phase by reducing the flow rate close to the minimum allowable limit at $0.63kg/s$. The maximum overshoot in the controlled outlet temperature is 2.2^oC, corresponding to a POR of 4.4% and a decay ratio of 0.6. The maximum POR reached 5.5%, when the setpoint was changed at $t = 13.5hr$.

After the initial oscillations are damped following a setpoint change, the controller manages to track the setpoint with a small RMSE that ranged from $\pm0.25^oC$ to $\pm0.36^oC$. This is achieved by manipulating the mass flow rate to compensate for disturbances such as the change in solar irradiation as shown in Figure 5.6.

The controller also manages to reject the oscillatory disturbance present in the inlet temperature. For example, the controller responds to severe changes in inlet temperature at $t = 12.7hr$ caused by pumping cold water
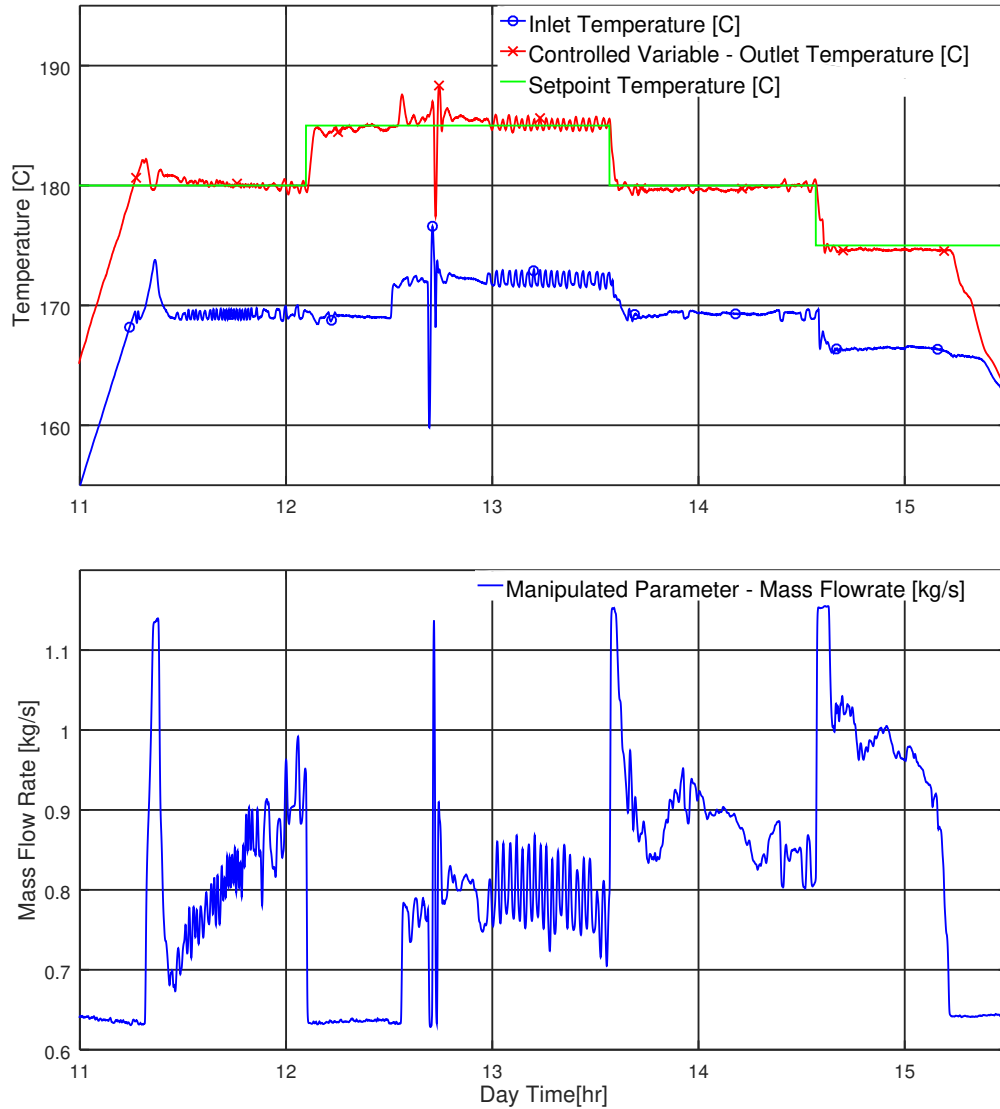
Figure 5.5: Measured temperature control using a PID with parallel feed-forward controller based on the optical model. Sudden dip between $t = 12.6hr$ **and** $t = 12.8hr$ **is caused by pumping cold water into the system. Top : profiles of inlet, outlet and setpoint temperatures. Bottom : Mass flow rate which represents the control action. (Testing facility : Hochdorf)**

into the system. The controller responds by reducing the flow rate immediately and recovers the setpoint tracking as soon as the water pumping stops.

The fast response of the controller during such disturbances is mainly attributed to the feed-forward controller and not the PID controller, as is shown in Figure 5.7. From the figure one can see that the biggest portion
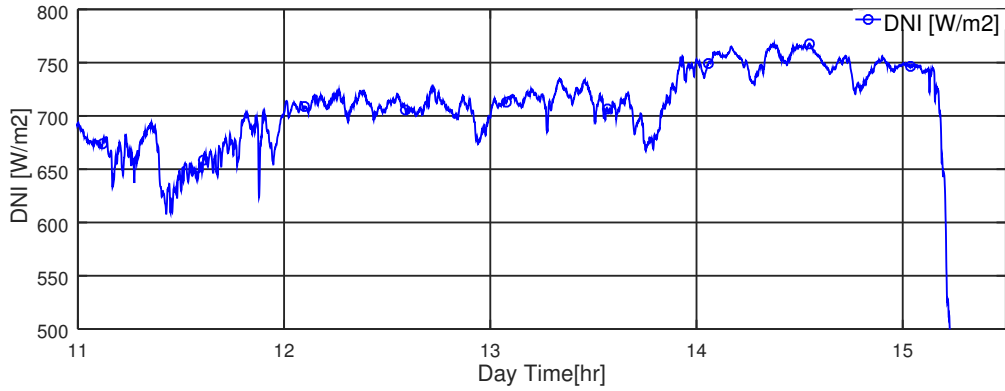
Figure 5.6: Measured DNI during the test day. (Testing facility : Hochdorf)

of the controllers reaction comes from feedforward term compared to other PID terms.
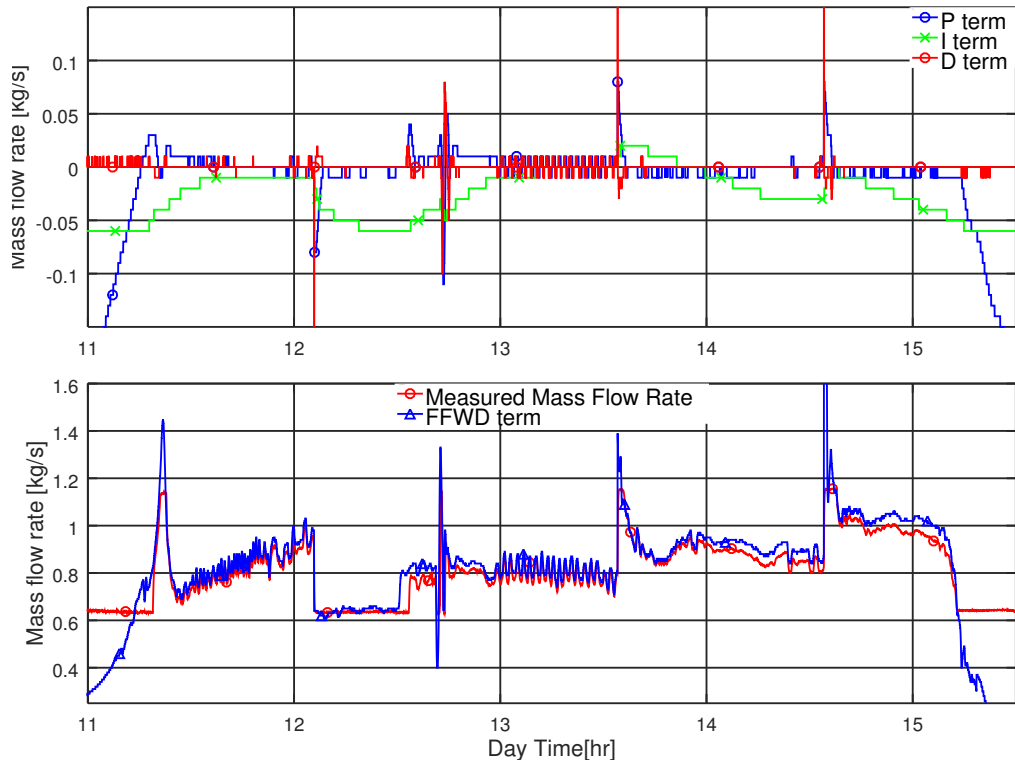
Figure 5.7: Measured temperature control using a PID Controller with parallel feed-forward based on the optical model. Top: individual controller parameters. Bottom: profiles of inlet, outlet and setpoint temperatures. (Testing facility : Hochdorf)

At $t = 12.10 hr$, the outlet temperature setpoint is changed from $180^o C$

to 185^oC, the controller responds by reducing flow rate to a minimum to approach required temperature quickly.

At $t = 12.5hr$ collector inlet temperature changed from 170^oC to 173^oC due to changes in the load circuit. This explains the sudden overshoot in outlet temperature which is corrected by the controller by increasing the mass flow rate from $0.63kg/s$ to $0.78kg/s$.

At $t = 13.6hr$ both inlet and outlet setpoints are changed. In this period, due to the lack of oscillations, it is clear how the mass flow controller tracks the changes in DNI to maintain a constant temperature with an RMSE of only $\pm 0.32^oC$. At $t = 15.2hr$, a big cloud covers the sky and DNI drops to a very low value.

5.4 Alternative Control Strategies for Special Applications

All previous control methods for controlling the outlet temperature of the collector use the mass flow rate as the manipulated parameter. However, this control method is only possible if the mean process load and the mean collector power match. This is true for many processes, where the load can be actually thought of as an infinite sink or when the solar process is hybridized with other sources of fuel. It is worth noting that the load and source (supply and demand) are not required to match instantaneously, rather the mean values should, provided that enough buffer storage is available.

When this is not the case, and there is big discrepancy between collector power and load, the system will either overheat or not reach the required temperature. In case of overheating, the mass flow controller reaches its limit by providing the maximum flow rate, at this point the only way to prevent overheating is to reduce the power delivered to the HTF ($\dot{Q}_f$), i.e. Energy Dumping. Equation 5.10 presents the relationship between collector outlet temperature T_o and power $\dot{Q}_f$. Note that T_i is not controllable as it is a function of the load.

$$T_o = \frac{\dot{Q}_f}{\dot{m}_{rec}c_p} + T_i. \tag{5.10}$$

$\dot{Q}_f$ can be manipulated by changing the number of mirrors which focus solar irradiation on the absorber tube.

The ability to change the active collector area is a desirable characteristic. This characteristic is available for some Fresnel collectors that have separate drives for mirror lines. In Industrial Solar's Linear Fresnel collector (LF-11) mirrors are arranged in 11 lines, each of which tracks the sun separately using a single DC-motor.

It is important to note, that although it is desirable to be able to reduce the collector power by controlling the effective area, it is also desirable to operate the collector at full power to avoid wasting energy that can be harnessed. Hence, it is only recommended to use the power controller to avoid overheating.

When power controller instead of a mass flow rate controller is used, the mass flow rate remains constant and the collector power is adjusted. The amount of power needed to achieve the required temperature at the collector outlet can be calculated as follows:

$$\dot{Q}_f = \dot{m}_{rec} c_p (T_r - T_i), \tag{5.11}$$

which can be rearranged to:

$$\dot{Q}_{solar} - \dot{Q}_{loss} - \frac{dE}{dt} = \dot{m}_{rec} c_p (T_r - T_i), \tag{5.12}$$

$$\dot{Q}_{solar} = \dot{m}_{rec} c_p (T_r - T_i) + \frac{dE}{dt} + \dot{Q}_{loss}, \tag{5.13}$$

where T_r is the temperature setpoint.

Compared to temperature control using mass flow adjustment the control of temperature by changing the delivered power is simpler since the manipulated parameter has a linear relationship with the controlled parameter as can be seen in Equation 5.13.

The problem however lies in the manipulated parameter itself. Since the power is adjusted by changing the number of mirrors focused on the target, then the power can only be changed in steps of one mirror at a time. Since the number of mirror rows per collector is eleven, this means that each step is equal to $1/11 = 9.1\%$.

5.4.1 Power manipulation using varying mirror combinations and a PID controller with Feed Forward Control

Figure 5.9 depicts a block diagram of the system. The controller consists of a PIDcontroller with a parallel feed forward controller. The resulting controller output is given by the following equation:

$$\underbrace{\dot{Q}_{controller}}_{\text{Controller Output}} = \underbrace{\dot{Q}_{FFWD}}_{\text{Feed Forward Term}} + \underbrace{\dot{Q}_{PID}}_{\text{PID terms}}, \tag{5.14}$$

where $\dot{Q}_{controller}$ is the total power required from the collector as calculated by the controller, $\dot{Q}_{FFWD}$ is the feed forward controller term and $\dot{Q}_{PID}$ is the PID term.

The feed forward controller term $\dot{Q}_{FFWD}$ is calculated using Equation 5.13. The mass flow rate $\dot{m}_{rec}$ in this case is a constant, and the manipulated parameter is $\dot{Q}_{solar}$.

The problem in this system however is that the controller output cannot be readily translated into an actuator signal since the collector power can only be changed in steps of 9.1% as was discussed above.

Nevertheless, the contribution of each mirror row to the total power collected is not equal. Because of their relative position between the sun and the absorber, each mirror line will have a different contribution to the total power reaching the absorber tube depending on the time of the day and the relative angle of that line to the sun vector (see Figure 5.8).

Figure 5.8: A photograph of a Fresnel collector consisting of eleven mirror rows. Each of them track the sun separately. This is defined in the figure by three vectors, the sun vector (s), the reflected radiation vector (r) and the mirror surface normal vector (n). Due to their relative position to the absorber tube, each mirror is tilted in a different angle in order to hit the target. The cosine of the angle between the s and n vectors defines the ratio of reflected radiation compared to the maximum when the angle is zero. This is called the cosine loss. (Testing facility: Fischer).

Taking advantage of this fact, an algorithm has been developed to translate the output of the controller into combinations of mirrors that have to be focused to achieve the control action demanded by the controller. Figure 5.9 depicts the system block diagram.

The controller calculates the relative contribution of each mirror at each moment of time based on sun position. Then, it sorts the mirrors based

on their relative power using a bubble sort algorithm. Once the mirrors are sorted, the controller then choses the mirror combinations that results in the closest power to the demanded power. This novel technique for selecting mirror combinations reduces the effect of the discrete nature of the manipulated parameter.
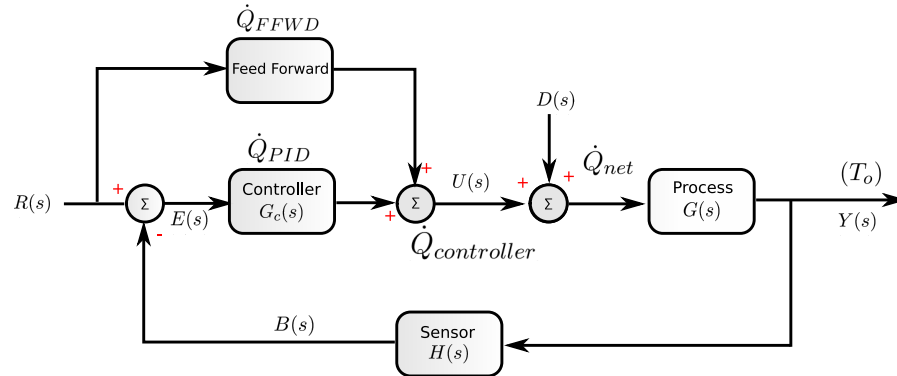
Figure 5.9: Control Block Diagram of the PID controller used to control outlet temperature using power control.

5.4.2 Power Manipulation Using a Hysteresis Controller

Another method can be used to control the outlet temperature of the collector using power manipulation. In this method a two point controller (see [51]) or hysteresis controller is used to increase/decrease collector power depending on the outlet temperature. The controller typically runs within a temperature range around the setpoint, hence oscillations are unavoidable(see Figure 5.10).

The advantage of such controller comes in easy implementation and commissioning. The realization of such a controller requires some experience to choose the controller parameters. Mainly the update cycle (which is the time interval between each correction command) of the controller, the temperature hysteresis and the power manipulation step sizes. These parameters should be chosen well to take into account both system size and transport delay which is a function of the volume flow rate.

Deviations from the nominal flow rate at which the parameters are tuned will result in degraded operation. This is shown in Figure 5.10, the volume flow rate of the system is decreased which results in larger oscillations.
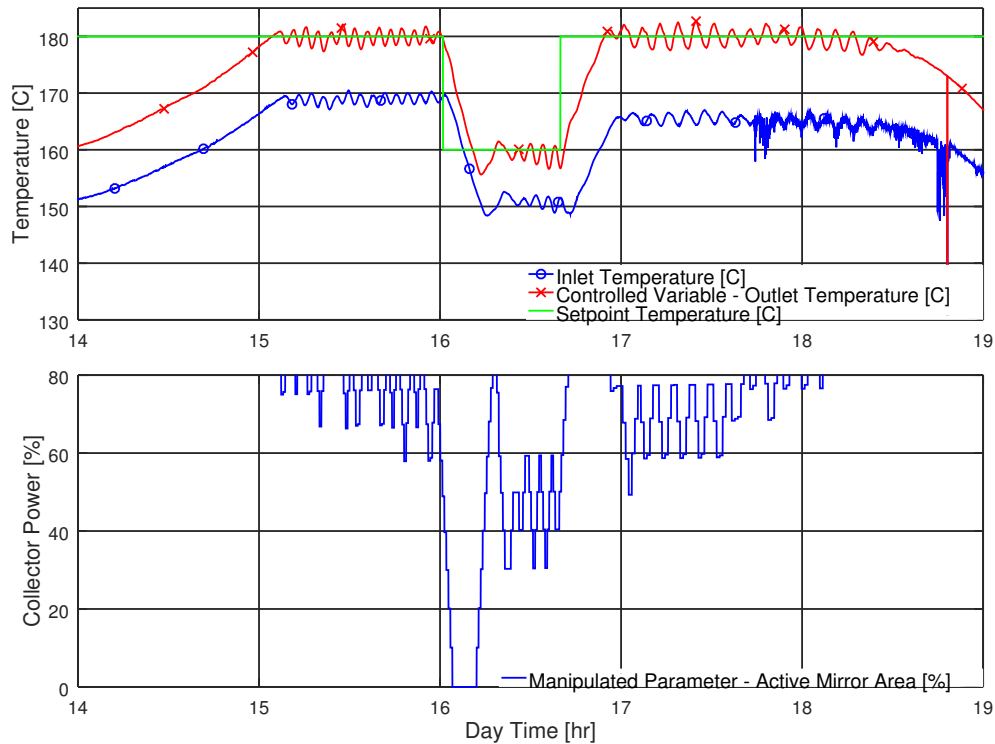
Figure 5.10: Temperature control through power adjustment. Power is manipulated using a hysteresis controller that operates within a 1^oC temperature range and power steps of 10%. (Testing facility: Kramer).

5.5 Summary

Temperature control is important for many industrial applications as many thermal processes operate optimally within a certain temperature range. Hence, the ability of the solar thermal system to maintain constant supply temperature to the load is a big added value.

In this chapter the problem of temperature control in the solar field is addressed by designing and testing suitable controllers.

The lumped parameter system model summarized in Equation 4.8, provides insight about system dynamics. It shows that the system suffers from a variable dead time, that the relationship between system input and output is nonlinear, that the time constant is related to systems input, and finally that some of the systems parameters are time variant. The simplicity of the lumped parameter system model allowed for its use in model based feed forward control. Moreover, the model is suitable for experimental parameter identification. The identified parameters have been used for simulations and in controller development.

Several controllers have been developed for the control of outlet temperature. As has been shown, conventional PID controllers are not adequate for the job and provide unstable operation evident from the high decay ratio of 1.25 and the high Peak Overshoot Ratio of 91%.

Adding a well designed feed forward term to the PID helps in reducing the effect of non-linearity caused by the inverse relationship between system input and output. The feed forward term also accounts for measured disturbances.

The best performing controller in terms of disturbance rejection and setpoint tracking is the one using the optical model to calculate the feed forward term. The controller is shown to have a maximum overshoot of 2.2^oC corresponding to a maximum POR of only 5.5% upon setpoint change, compared to a high POR of 91% for the conventional PID controller. The controller was stable even under disturbances from inlet temperature with a decay ratio of 0.6, well below 1.0 which indicates a stable system compared to a decay ratio of 1.25 for the conventional PID controller. The RMSE in setpoint tracking for this controller ranges from $\pm0.25^oC$ to $\pm0.36^oC$.

Since this controller requires the measurement of DNI, it is not always feasible to implement. Another method for calculating the feed forward term is also presented. The method uses past measurement data to estimate the available collector power $\dot{Q}_{net}$. The controller presented a good damped response with a POR of only 4% and a decay ratio of 0.75. The RMSE in setpoint tracking is $\pm0.54^oC$.

A combination of the optical model and the use of historical data as a fall back solution is shown to be the best option in operation.

Other controllers based on the manipulation of the collector effective area are also presented. These controllers proved to be necessary for special applications, for instance when flow rate manipulation is not possible.

Chapter 6

Control Strategies for DSG

PID based control is by far the favorite control concept in the industry, and direct steam generation is no exception. Most workers in the field use or have used PID controllers. However when it comes to the details of controllers used in such systems the amount of information available in the literature is very limited because,

1. The number of operating DSG systems worldwide is limited. Especially those for process heat applications.

2. Information from available systems are typically not disclosed because they represent valuable intellectual property.

Moreover, although the control and dynamics of solar DSG systems was studied by some researchers, these studies were almost exclusively related to DSG power plants and not for process heat applications [66, 67, 27].

In this section, the PID based control of DSG system is developed. The control concept is based on PID control theory in its wider sense. It includes advanced control techniques like feedforward, anti-windup, setpoint-scheduling, supervisory control and other advanced control concepts that work around the PID controller to gap their inherent limitations.

It is worth mentioning that the advanced PID control system developed within this work has been tested for an extended period of time in the test facility. Eventually it has been implemented and commissioned in commercial operation in March 2015 [49, 9, 44]. This control law represents the current deployment-mature control concept for DSG systems. Performance and test results are also shown in this chapter from the testing facility in Freiburg and also from the commercial plant in Jordan.

In Section 6.2, an Adaptive-Horizon nonlinear model predictive control strategy is suggested for the control of DSG systems. Results from the test of this strategy are presented and discussed. Model predictive control is used to provide a universal and enhanced control law. Model predictive control is gradually gaining grounds in the industrial arena with advent of

high speed controllers. Model predictive control has many advantages over classical control especially for nonlinear and complex systems. However the development effort and the high computational loads, makes it very challenging to come up with a robust, stable and accurate controller. For sake of comparison, the PID based control law requires less than a millisecond to be calculated in a standard low-speed industrial PLC, whereas the MPC controller requires 500 millisecond to be evaluated on a $1.6GHz$ processor.

6.1 Development and Experimental Testing of an Advanced PID Control

Three controllers are used to control the system in DSG mode as seen in Figure 2.7. These controllers are assumed independent in this approach as compared to the modern control theory approach.

1. Steam Network Pressure Controller: The pressure controller maintains the pressure of the steam network at the required setpoint. At the event where there is no enough steam in the steam drum, the pressure controller should close the regulating valve. Moreover, in the case when the demand in the steam network is cut-off the control valve should also close rapidly to prevent over pressurizing the steam network. This can happen quite fast if the demand drops abruptly. Another version of this controller can be used to control the pressure of the steam drum itself.

2. Feedwater Controller: This controller will control the supply of feedwater to the system. The main task of this controller is to prevent the level of the steam drum from exceeding the limits. Not too high to result in liquid carryover and not too low to starve the recirculation pump. Although this might seem straight forward enough, the changes of the water content of the collector field combined with changes of liquid volume and the presence of steam bubbles under the liquid level prove to be hard challenges to resolve and result in a non-minimum phase control problem as described by [4].

3. Recirculation flow controller: This controller has the crucial task of maintaining enough flow in the absorbers to prevent overheating. This is especially important during transient conditions when the flow rate changes as a result of pressure drop variation across the absorber. The change in pressure drop is induced by two phase flow dynamics and can lead to flow instabilities. The recirculation flow controller is also designed to receive flow rate setpoints from the supervisory controller to avoid undesired two phase flow patterns.

6.1.1 BOP Supervisory Controller

Since PID controllers are typically used for single input single output (SISO) systems, it is necessary to have a supervisory controller that overlooks the operation of the several controllers and handles system transitions between different modes of operation. This controller is called the Balance of Plant (BOP) supervisory controller. The duties of the BOP supervisory controller are summarized in this section.

Transition between system states

The DSG system is normally in one of two states, either operation or standby. The transition from standby to operation state is achieved through the startup procedure. The startup procedure is started by the BOP controller when the DNI is $> 200W/m^2$ and the sun zenith angle is $< 80.0^o$. During startup procedure the recirculation pump is turned on and circulates water from the steam drum through the solar field. This is done to ensure that there are no excessive temperature gradients within the system before the mirrors are focused on the absorber. These gradients exist since the pump is turned off at night and since the thermal losses at night are higher in the piping and in the absorbers compared to the steam drum. The startup procedure is terminated when the temperature at different parts of the system is within 5^oC.

After startup, the operation procedure is reached. In operation state, all controllers are activated and the steam production and supply can begin. During the operation procedure the BOP controller still has the task of overseeing the controllers operation, and modifying setpoints when necessary.

As the system reaches end of operation, either because of the end of the day or because of reaching the minimum value of DNI for a certain amount of time, the BOP controller initiates the flood procedure.

The flood procedure is used to remove all the steam from the absorber tubes and fill them with liquid water to avoid under pressure at night when the steam condenses. The flood procedure is a timed procedure, where the recirculation pump is turned on at full speed for five minutes.

After the execution of the flood procedure the BOP controller puts the system in standby mode where all the pumps are turned off and the system is in standby waiting for the startup procedure again.

Power Staging

In order to avoid abrupt changes in input power, the BOP controller regulates the power input from the solar field. This is achieved by determining the amount of mirrors focused on the absorber at a given time. For example, when the pressure in the steam exceeds a certain limit, the supervisory

controller will gradually reduce the amount of power delivered by the solar field. It will also increase it gradually when more power is needed. Similar action is done when the mirrors are removed from focus and then back in focus when a cloud passes. Mirror refocusing is done gradually to ensure a smooth transition, this is called power staging.

Cloud Detection

During operation it is important to be able to detect if a cloud passes above the solar field. This is necessary so that the BOP controller can adapt the system parameters in anticipation of the dynamics that occur as the cloud crosses the solar field (e.g. power staging). The cloud detection is based on DNI measurement and the BOP controller uses two system flags to describe the cloud situation:

1. *CloudDetected* flag: This flag is set to $TRUE$ when the DNI falls below the threshold ($< 300 W/m^2$) for more than $15 seconds$ while the sun zenith angle is $< 70^o$. Otherwise it is reset to $FALSE$

2. *CloudBuffer* flag: This flag is set to $TRUE$ as long as the flag *CloudDetected* is $TRUE$. Once the *CloudDetected* is reset to $FALSE$ it stays $TRUE$ for a buffer period ($120 seconds$) before it is reset to $FALSE$.

When the *CloudDetected* is set, the collector removes all mirrors from the focal point. When the cloud clears, the flag is reset and the collector starts increasing the delivered power slowly to avoid thermal stresses and unfavorable flow patterns. Power staging lasts until the *CloudDetected* is reset.

Steam Drum Level Setpoint Adaption

The steam drum level is not only affected by the mass balance of steam delivery and feedwater flow. It is also affected by the amount of liquid and steam in the solar field. When big changes in the steam drum level are expected, for example between the standby state and operation state. The BOP controller adapts the setpoint of the steam drum liquid level.

For example if the fill level during operation is 70%. And we expect that we need 20% of the steam drum volume to fill the absorber tubes and other two phase flow pipes with liquid, then the standby fill level should be near 50%. If we were to keep the setpoint at 70% the controller will add more cold water to the system to fill the absorbers and unnecessarily cool the system and delay startup next morning.

Other adaptions of level control are handled by the level controller itself and are discussed in section 6.1.3.

Recirculation Flow Setpoint Scheduling

The mass flow rate in the solar field is controlled by the recirculation flow controller. The mass flow setpoint is provided by the BOP controller and is adapted according to the operation conditions. When the system is running normally, a reduced flow rate is used to save electrical energy. However, during certain conditions the flow rate is increased to enhance absorber cooling and prevent unfavorable flow patterns. These conditions are, low DNI, cloud passage, overheating, during end of operation and during flood procedure.

Control Exceptions and Emergency Handling and Detection

The BOP controller maintains the operation of the system within the safe limits. Therefore, one of its most important duties is to detect emergency situations and rectify them. It is also responsible for issuing control exceptions when needed. Following are the situations where the supervisory controller intervenes.

1. Loss of flow: When the supervisory controller detects that not enough flow rate is passing to the solar field it defocuses all mirrors immediately. This is a safety feature to avoid overheating the system. Such a situation can occur because of pump failure, blockage, leakage and cavitation.

2. Over Pressure and Overheating : The solar field operates in saturation conditions. The pressure slides in normal operation between $0bar_g$ and the upper pressure limit. At the higher end of this range the supervisory controller reduces the amount of mirrors focused on the absorbers to control the pressure and temperature in the system. If the pressure or temperature exceeds the limits, the supervisory controller removes all mirrors from focus. This is the first line of defense against over-pressure or over-temperature.

3. Flashing : Excessive flash steam drawn from the steam drum can affect system stability. To avoid this, the supervisory controller can detect flashing situations and limit it using the steam delivery valve. Flashing can be detected by monitoring the saturation pressure and comparing it to the steam drum pressure.

4. First Steam : Each morning the steam delivery pipe is filled with cold condensate from the previous day. When hot steam flows in the pipe it causes steam hammers. Therefore, each morning before steam is delivered to the steam network, the steam valve is opened slightly to let some low pressure steam into the load steam network to heat

it up and push condensate out. This exception is managed by the supervisory controller.

6.1.2 Pressure Controller

The pressure controller is used to control the pressure on the load steam network by changing the opening of the steam valve at the steam drum outlet (see Figure 2.7). In this case the solar system pressure is sliding and the steam network pressure is maintained.

The pressure in the steam line is maintained by matching the supply of solar steam to the demand on the user side. If the mass flow rates of the supply steam and demand steam are matched the pressure stabilizes.

Hence, there is a relationship between the steam mass flow from the solar system to the steam network and the steam network pressure. This relationship can be investigated by evaluating the cross-correlation between the two measured signals as shown in Figure 6.1.

The cross-correlation shows that the two signals are correlated as evident from the peaks in the cross-correlation diagram in Figure 6.1. We know that the pressure is the leading signal, that is to say that the flow rate is regulated to maintain the pressure and not vice versa. Hence, we can neglect the peak at the negative side of the diagram.

The peak on the positive side however is an estimate of the delay between the two signals which is in this case $50s$. This value represents the delay in which the changes in pressure are reflected in changes in steam mass flow including all measurement latencies (see Figure 1.6). This delay is mainly related to the time delay between the changes in pressure on the steam network and the response by the controller and the actuator to counteract the change.

Figure 6.2 depicts the block diagram of the load pressure controller which consists of a PID controller with an advanced anti-windup and exception handling engine. The PID controller output is processed by the exception handling engine before it is fed to the process. The controller also includes an (Infinite Impulse Response (IIR)) filter on the measured signal to reduce noise induced controller action.

The PID controller output O_{PID} is calculated from the error signal $e(t)$ as follows:

$$O_{PID} = K_p e + K_i \int e + K_d \frac{de}{dt}, \tag{6.1}$$

where e is the error signal, K_p is the proportional gain of the PID controller, K_i is the integral gain and K_d is the derivative gain.
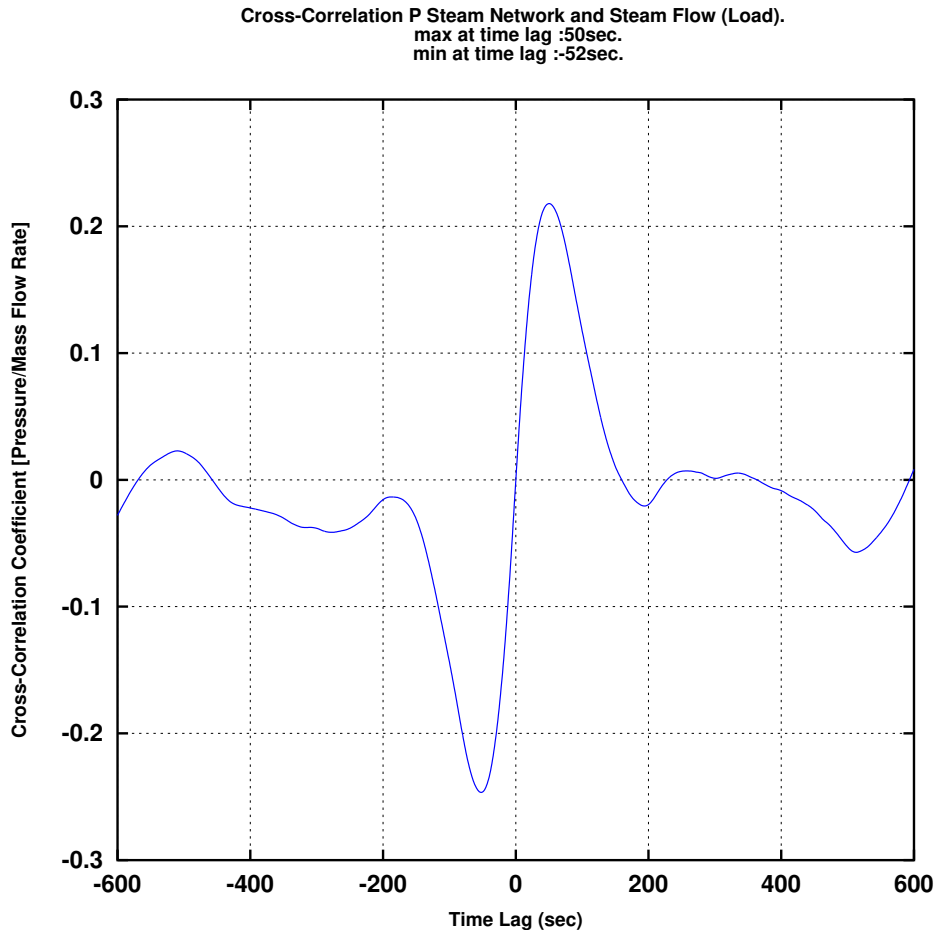
Figure 6.1: Normalized cross-correlation between the steam network pressure and the steam mass flow rate. The steam network pressure ranged from $5.0bar_g$ **to** $6.7bar_g$**, while the steam mass flow rate ranged between** $0kg/hr$ **and** $290kg/hr$**. Steam drum pressure ranged from** $10.0bar_g$ **to** $14.0bar_g$**. (Testing facility: RamPharma).**

Exceptions Handling

The exceptions handling engine illustrated in Figure 6.3 represents an important part of the load pressure controller. The exception handling block is responsible for handling situations where the PID controller fails to provide the appropriate course of action. This mainly occurs due to system nonlinearities. The exceptions handling engine reacts in the following situations:

- Windup: A practical issue of all real actuators is their saturation limits. For example, the valve cannot open more than $O_{max} = 100\%$ and
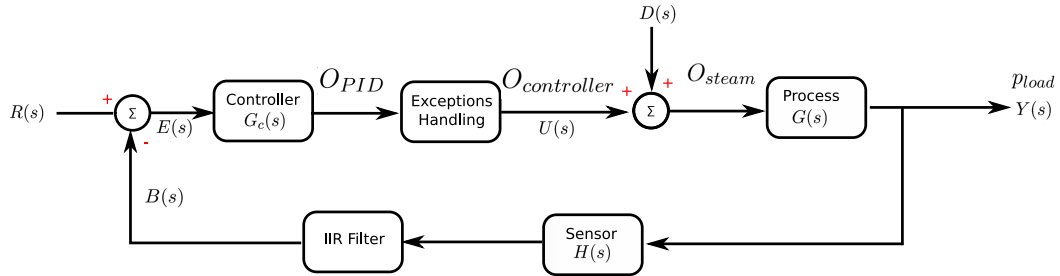
Figure 6.2: Block diagram of the steam network pressure controller consisting of a PID controller with an exceptions handling engine.

cannot close below $O_{min} = 0\%$.

As can be seen in the Diagram in Figure 6.3, when the PID controller exceeds the upper or lower limits, the PID output value (O_{PID}) is set to the corresponding limit (O_{max} or O_{min}).

Since the PID controller output (O_{PID}) cannot be changed directly, a modification on the integral part of the controller ($\int e$) is done so that the new controller output matches the required output as seen in Equation: 6.2

$$\int e = \frac{(O_{PID} - K_p e - K_d \frac{de}{dt})}{K_i},$$ (6.2)

where O_{PID} is substituted by O_{max} or O_{min}.

- Low Supply Pressure Exception: When the steam drum pressure (p_{sd}) falls below either the load network pressure (p_{load}) or the pressure setpoint (p_r), the steam valve should close because this means that no enough steam is available in the steam drum. This is a non-linear control action since in such occasions the valve moves from completely open to completely closed. Such situations cannot be handled by a typical PID controller and are handled as an exception. In fact, a typical PID controller would open the valve completely instead of closing it.

  In order to prevent the steam valve from opening and closing several times (i.e. hunting) by this exception, the steam valve will be only allowed to open if $p_{sd} > (p_{load} + \Delta p_3)$ and $p_{sd} > (p_r + \Delta p_4)$. The steam valve will be closed if $p_{sd} < (p_{load} + \Delta p_1)$ and $p_{sd} < (p_r + \Delta p_2)$ (See Figure 6.3) . The pressure differences $\Delta p_1, \Delta p_2, \Delta p_3$ and Δp_4, are adjustable values depending on each system. The default settings are $\Delta p_1 = \Delta p_2 = 1.0bar$ and $\Delta p_2 = \Delta p_4 = 3.0bar$.

- Over Pressure Protection : This exception occurs when over pressurization of the steam network occurs. As shown in Figure 6.3, Over-

pressure is detected if $p_{load} > p_r + \Delta p_5$. In this case the controller closes the steam valve. The default value for Δp_5 is $2.0 bar$.

- Flashing: Excessive flashing rate in the steam drum results in undesirable effects in the flow regime. This exception is used to prevent excessive flashing. When flashing is detected combined with a low mass flowrate ($\dot{m}_{rec}$) in the recirculation line the opening of the steam valve is reduced by 20%.

- Small Errors: This last exception is used to prevent excessive correction attempts by the controller when the error is small enough ($e < 0.001 bar$). This results in less wear and tear on the actuator and also makes the system less susceptible to noise and interference.

Exceptions Handling
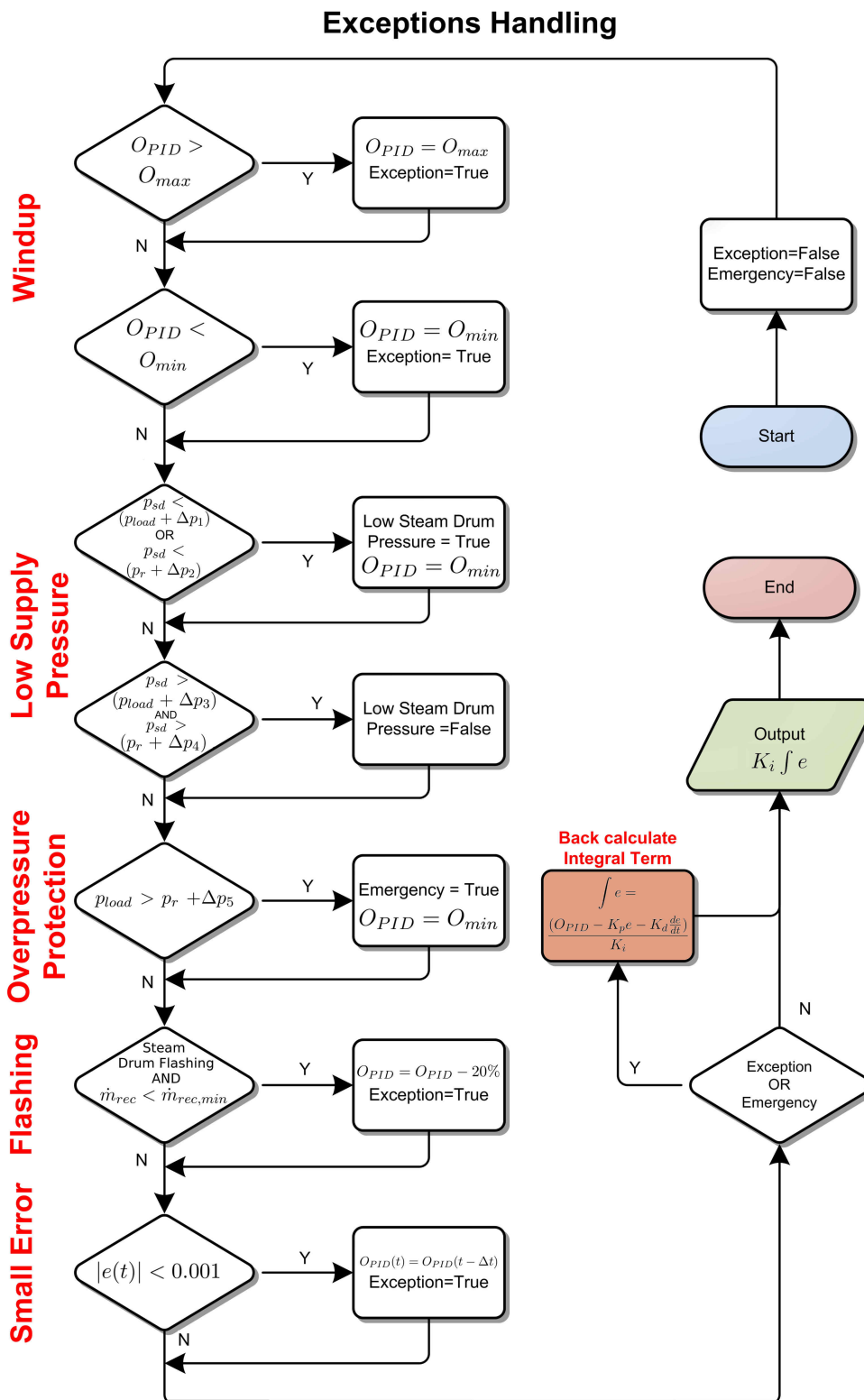
Figure 6.3: Exceptions handling block of the steam network pressure controller.

After all exceptions are considered, the back calculation of the integral term as shown in Equation 6.2 is done if needed. Then, the new $K_i \int e$ term is passed back to the process.

IIR filter

As seen in Figure 6.2, the IIR filter filters the signal measured by the pressure sensor before being used in the controller calculation. Such filtering is essential to get rid of measurement noise and interference. It is also important to avoid unnecessary corrections attempted by the controller for oscillatory pressure changes and hence, increases system stability. The disadvantage of such filter is that it introduces a delay in the system response depending on the filter interval.

$$\hat{p}_{load}(t) = \hat{p}_{load}(t - \Delta t) + x(p_{load}(t) - \hat{p}_{load}(t - \Delta t)) \qquad (6.3)$$

IIR filters digital filters are commonly used because of the remarkable simplicity in implementation. Equation 6.3 describes the implementation of an IIR filter as a recursive filter at each time step. Where $\hat{p}_{load}$ is the filtered pressure signal, p_{load} is the measured pressure signal and x is the filter weight. $x = 1.0$ results in no filtering action, while $x = 0.0$ results in the strongest filter where all changes are rejected.

Plant Identification and PID Tuning Values

Although plant dynamics change often depending on the operating conditions, it is helpful to conduct plant identification tests for the pressure controller. This is best done around the most common operating point of the system. It proves, however, that it is practically challenging to maintain stable conditions with no changes in the steam demand or the solar irradiation, hence approximations are inevitable.

Figure 6.4 illustrates the results of the bump test performed on the steam network pressure controller. The steam valve opening is reduced by 10% at $t = 225$ and then increased again at $t = 370s$. This results in a change in the pressure on the load side and also the steam mass flow.

The objective of the bump test is to extract the first order plus dead time (FOPTD) model parameters as outlined in the model equation.

$$G_p(s) = \frac{b}{\tau s + 1} e^{-s\kappa}, \qquad (6.4)$$

where b is the plant static gain, τ is the time constant and κ is the dead time.

From the figure, the plant static gain can be approximated to be $b = K_o/K_i = 1.25bar/10\% = 0.125bar/\%$. Notice that the pressure on the
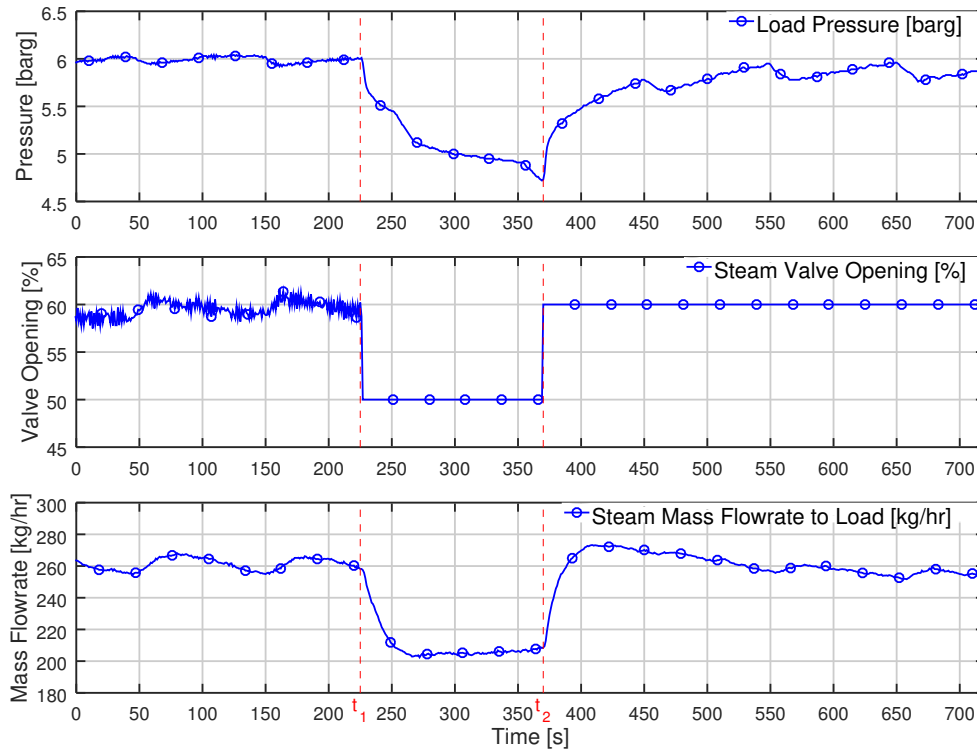
Figure 6.4: Measured response of the load steam network pressure during a 10% bump test on the steam valve from t_1 to t_2. Reduction of steam valve opening results in a drop of load pressure and a reduction in steam mass flowrate. (Testing facility : RamPharma).

steam line does not return exactly to the original value, but rather to a value $0.15 bar_g$ less. This is because of changes in the operating conditions of the system.

In order to evaluate the time constant of the plant, the maximum slope of the pressure is taken when the valve reopens. This slope is found to be $0.11 bar/s$. The time constant is the time that the system needs to reach the steady state value if it continues to move at the same maximum slope. Hence, the time constant is $\tau = 1.25/0.11 = 11.36s$. The dead time of this particular plant is small to be seen from the figure but was estimated to be $\kappa = 1s$.

Another test has been performed leading to slightly different results, $b = 0.11 bar/\%$ and $\tau = 8.2s$.

Based on these values one can can evaluate starting values for the PID parameters based on tuning recipes available in the literature. For this we choose the tuning recipe outlined by Doug Cooper in [21] in Table 6.1.

The closed loop time constant, t_c is used to specify the desired speed

Table 6.1: Tuning correlations for PI controller, and PID controllers. Courtesy of [21].

	Controller Gain(K_c)	Reset Time (t_i)	Derivative Time (t_d)
PI	$\frac{1}{b}\frac{\tau}{\kappa+t_c}$	τ	
PID	$\frac{1}{b}\frac{\tau+0.5\kappa}{t_c+0.5\kappa}$	$\tau + 0.5\kappa$	$\frac{\tau\kappa}{2\tau+\kappa}$

or quickness of the resulting controller in responding to a setpoint change or rejecting a disturbance [21]. The closed loop time constant is computed as follows[21]:

- for aggressive performance, t_c is the larger of 0.1τ or 0.8κ,

- for moderate performance, t_c is the larger of 1.0τ or 8.0κ,

- for conservative performance, t_c is the larger of 10.0τ or 80.0κ.

Based on the approximated first order system parameters and the tuning recipe, the starting tuning parameters of the PID controller are summarized in Table 6.2. The last row of the table include the fine tuned PID controller parameters which are actually used.

Table 6.2: PID Controller Tunning Parameters for the RamPharma facility in Jordan. The table shows results from first and second trials in addition to the experimentally fine tuned parameters which are actually used in operation.

	K_p	K_i	K_d
First Trial	8.00	0.67	3.83
Second Trial	9.09	1.04	4.28
Fine Tuned Values	10.0	0.08	5.0

Experimental Results of PID Load Pressure Control

The steam network pressure controller has been implemented on a commercial system that provides saturated steam to a pharmaceuticals manufacturer in Jordan. Since the system is a commercial and non-R&D

system, it has been subject to real life operating conditions and the controller has to be able to cope with many exceptions and disturbances.

In this particular system, perhaps the biggest challenge is to deal with the intermittent nature of the steam demand on the customer side. Most of the steam consumers are drying processes that use hot air to dry the pills after mixing. These dryers heat the air using a steam/air heat exchanger. The temperature of the hot air is being controlled using an ON/OFF valve on the steam inlet of the heat exchanger. This control action (compared to continuous control) results in sudden changes in the steam demand and rapid pressure changes.

Figure 6.5 depicts the response of the load pressure controller. The controlled variable is the load pressure (p_{load}) depicted in the top graph in blue. The controller tries to maintain p_{load} close to the setpoint pressure (p_r) depicted in green. As seen in the figure, the setpoint pressure is set to $5.0 bar_g$. The controller manipulates the steam valve opening (O_{steam}) as shown in the middle graph to achieve p_r.

The steam mass flowrate ($\dot{m}_s$) depicted in the bottom graph in Figure 6.5 represents the steam demand by the load.

Figure 6.6 depicts the response of the steam valve at the beginning of operation. The pressure controller shows quick response, with a rise time of $106s$. The peak over shoot was only $0.15 bar_g$ corresponding to a POR of 13.7%. The controller reached and maintained the setpoint after the first overshoot with a decay ratio of only 0.06 which indicates almost no oscillations.

Again in Figure 6.5, one can notice that the controller manages to keep the setpoint within $\pm 0.1 bar$ of the setpoint. The RMSE in load pressure control from $t = 8.5hr$ to $t = 16.5hr$ was only $\pm 0.015 bar$.

The pressure control accuracy is strongly related to the steam demand changes. When the changes in demand is slow the pressure controller can achieve very high control accuracy as seen was shown in Figure 6.5. When the steam demand changes quickly, the pressure control accuracy will be less.

Such a situation is depicted in Figure 6.7. Here, the steam demand varies abruptly seen as sudden jumps in the steam mass flowrate in the bottom graph. These spikes directly affect the pressure in the steam network and provoke the steam valve to increase the opening. These changes are considered disturbances to the system.

Nevertheless, the load pressure controller manages to provide adequate performance as the peak overshoot despite demand changes was $0.58 bar_g$. The POR calculated for system startup at $t = 7.9hr$ is 14%. The controller also manages to limit oscillations after reaching the setpoint as the decay ratio was only 0.095. The pressure control accuracy during this day was RMSE $= \pm 0.15 bar$, which was calculated between $t = 8.5hr$ to $t = 16.5hr$. This is ten times more than that calculated for Figure 6.5.
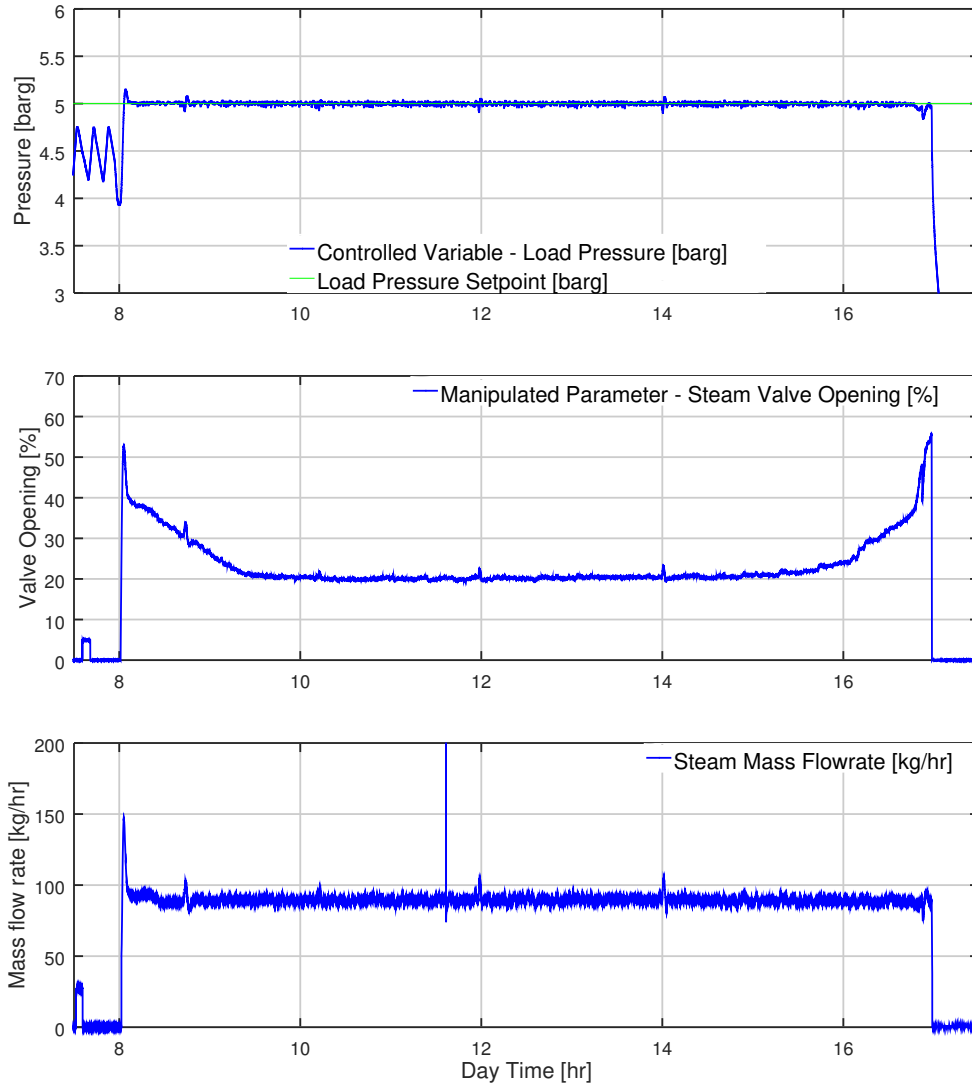
Figure 6.5: Measured response of load pressure controller. Top: Pressure signal of the load steam pressure representing the controlled variable. Middle: Percent opening of the steam valve representing the manipulated parameter. Bottom: Steam mass flowrate. (Testing facility: RamPharma)

6.1.3 Steam Drum Liquid Level Controller (Feedwater Controller)

The liquid level in the steam drum changes during normal operation and in transient conditions. The two extremes are :

- Too high liquid level risking overflow or resulting in liquid carryover as steam leaves the steam drum.
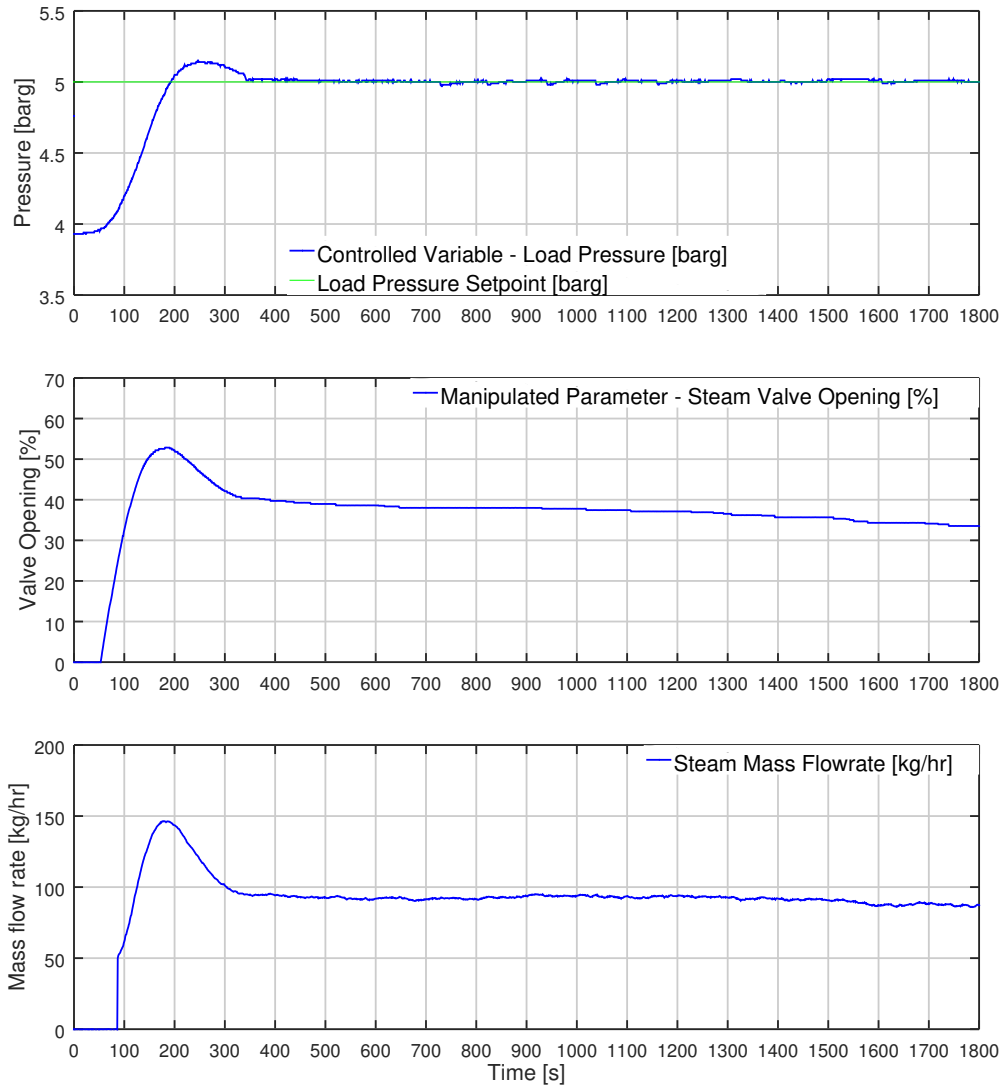
Figure 6.6: Measured dynamic response of the steam valve starting to feed steam to the load network in the morning. Top: Pressure signal of the load steam pressure representing the controlled variable. Middle: Percent opening of the steam valve representing the manipulated parameter. Bottom: Steam mass flowrate. (Testing facility: RamPharma)

● Too low liquid level risking starving the recirculation pumps.

On another level, it is desirable to maintain a high water level in the steam drum when storage capacity is needed since energy is actually stored as sensible heat in the liquid phase in the steam drum.

Meanwhile, during normal operation and when extra storage capacity
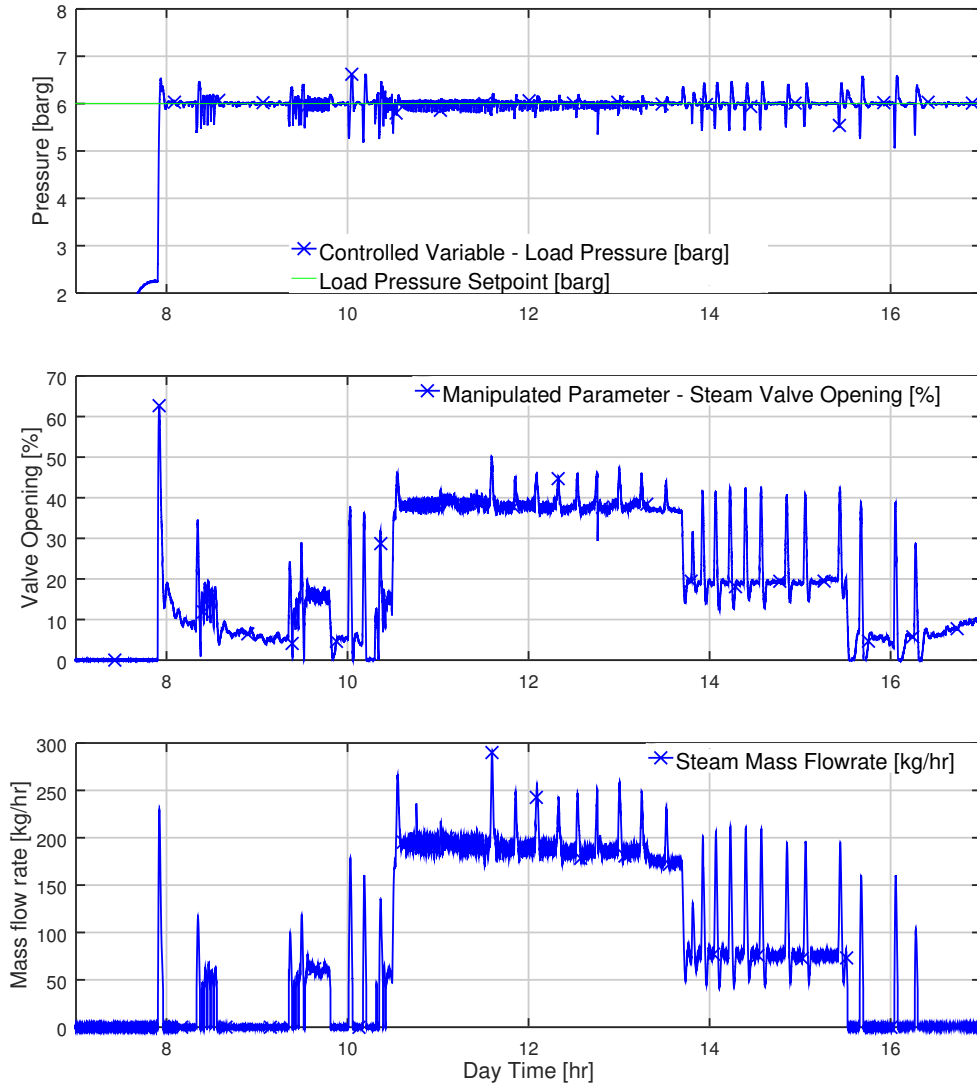
Figure 6.7: Measured response of network pressure controller under varying demand levels. Top: Pressure signals of the steam drum and the load steam network. Middle: Steam drum liquid level and percent opening of the steam valve. Bottom: Steam mass flow rate and expected collector power.(Testing facility: RamPharma)

is not needed, the controller should avoid adding any cold feedwater when not necessary. This is to avoid disturbing the thermal balance in the steam drum and to avoid delaying system startup.

The feedwater controller should actually compensate for steam drum level changes only caused by outward steam mass flow. Hence, it is essential that the controller distinguishes changes in level which are not caused

by steam outward flow.

Changes in steam drum level are induced by the following factors:

1. Outward steam mass flow.

2. Inwards feedwater flow.

3. Change in density of liquid at different operating conditions. During operation pressure normally changes from $7.0bar_g$ up to $16.0bar_g$. Then liquid water density will also vary from $896.9kg/m^3$ to $859.5kg/m^3$ respectively, which corresponds to a 4.17% change. The change of water density when the system is cold at 25^oC is 13.79%.

4. Change of density of vapor at different operating conditions. This is similar to the effect described for liquid density. (A detailed example is given in section 3.2.5).

5. The void fraction of the absorbers and pipes that contain two-phase flow depending on the operating conditions. At startup, two phase flow pipes and absorber tubes are filled with liquid water. As the evaporation starts in the absorber tubes liquid water is pushed out to the steam drum which raises liquid level. Moreover in transient conditions like cloud passing, evaporation is slowed down and liquid water from the steam drum is used to fill up these pipes again causing a drop in liquid level.

6. The amount of steam which is present under the liquid level as bubbles. The steam bubbles under liquid level will either expand or collapse depending on the changes of pressure which leads to a sudden swell or shrink. This in turn changes the apparent liquid level.[4, 43]. Such phenomena is hard to control using a classic PID controller but also heavily depends on whether the two-phase flow pipe from the solar field feeds the steam drum above or below the liquid level. Feeding below liquid level will greatly increase the number of steam bubbles under liquid level and hence in this case the situation is more severe.

Figure 6.8 depicts the PID feedwater controller with adaptive setpoints and all the necessary calculation blocks. Ideally, the feedwater controller should match the first two factors, inward feedwater and outward steam mass flows. The later factors however, are disturbances and are accounted for by employing mass control inside the system and using setpoint scheduling for normal conditions and abnormal conditions as follows:

1. Under normal operation conditions, the setpoint is defined by defining the desired maximum liquid fill volume ($V_{wd,max}$). This occurs during DSG operation at maximum temperature (and pressure). The mass of water inside the steam drum under those conditions ($M_{wd,max}$) is

then used as the setpoint of the feedwater controller. Hence in these conditions the water level in the steam drum is changing while the mass will be constant. In this manner change in water density inside the steam drum is taken into account implicitly within the controller algorithm.

2. During transitions, standby and other abnormal conditions , the steam drum level is supposed to drop. In these situations loose control on the steam drum contents will be tolerated, that is why the steam drum mass setpoint is reduced to a lower level. The lower level is calculated by the worst condition, i.e. when the system is the coldest and all the pipes are filled completely with liquid water. The events when reduced steam drum level is used are summarized as follows.

   (a) Low Irradiation and Cloud Passage (see section 3.2.4),
   (b) Standby Mode
   (c) Flooding Procedure (Transition from operation to Standby)
   (d) Startup after Standby
   (e) Abrupt changes in system pressure (see section 3.2.5).
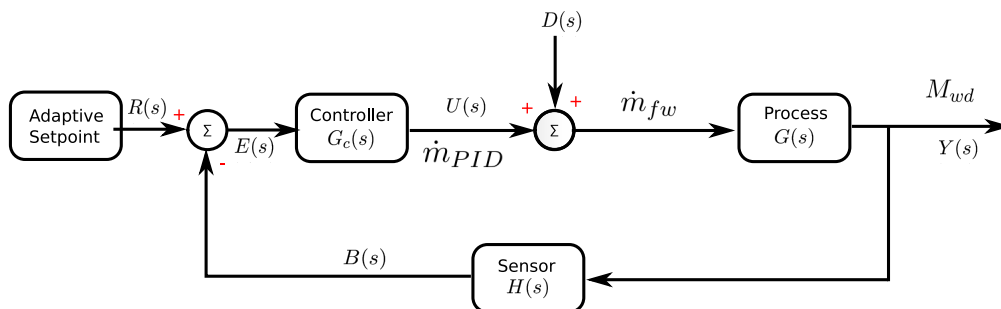
Figure 6.8: Feedwater controller block diagram depicting classic PID controller with closed loop feedback system. For accurate operation the controller relies on an adaptive setpoint generator block as an input.

Another control algorithm can be built based on mass balance as the controlled variable in contrast to liquid level. However, this requires accurate mass flow measurements of both feedwater and steam flows. Such controller is perhaps simpler in general. However, it requires two additional sensors to operate (three in total).

Study Case for Steam Drum Level Reduction Expectation

As an example for calculating the reduction in steam drum level at worst case scenario, the system in Jordan at RAMPharma is taken. The system

has a $2.0m^3$ steam drum, and a desired maximum volume fill level of 80%, then $V_{wd,max} = 80\% * 2.0m^3 = 1.6m^3$. The water mass in the steam drum is then $M_{wd,max} = 1369kg$ at 200^oC.

1. When the system is cold at 4.0^oC the water volume will shrink from $1.6m^3$ to $1.369m^3$ for the same water mass with a total reduction of $V_{shrink} = 0.231m^3$.

2. Water is taken from the steam drum to fill the absorber pipes reducing it by $V_{abs} = 0.247m^3$.

3. Water is taken from the steam drum to fill the two phase pipes reducing it by $V_{2ph} = 0.034m^3$.

As mentioned this is a worst case scenario with some over estimation since the pipes are never actually completely full of steam and also it does not account for the mass of steam already in the pipes. This calculation also neglects the expansion of water inside the inlet line. The overall reduction in steam drum volume is then $0.512m^3$ which is 25.5% of total steam drum volume. 14.0% of this reduction is attributed to filling of the absorber tubes and the two phase flow piping.

Non-linearities of level controllers caused by DSG dynamics

Controlling the feed pump using the described control strategy is often not enough. Mainly because of the time delay in the response of the steam drum level. As can be seen in Figure 6.9, the feedpump is operated here as ON/OFF actuator. It runs at full speed for 6.75 minutes until the level of the steam drum reaches the setpoint of 70%. However after the pump shuts down, the steam drum level keeps increasing, reaching a maximum of 76.5% and afterwards settles at 72.5% after 4.5 minutes of feedpump shutdown. During this phase, it can be also seen that the pressure of the steam drum drops by more than $1.0bar$ as a result of feeding the cold water.

This delay in the steam drum level can be explained by the fact that when cold water is pumped in the solar field, the evaporation interface moves further downstream. This in turn results in increasing the liquid content in the solar field which counteracts the added liquid volume. As the liquid is heated up the evaporation interface will go back to the steady state and the extra liquid in the solar field will be returned to the drum. This also explains the steady state overshoot in the steam drum level.

The steam drum level overshoot is also related to the pressure drop that combines the feeding water to the steam drum. This is similar to the situation of abrupt pressure changes described in section 3.2.5.

Ideally, to solve this issue, the feed pumpPID controller's "sensitivity" can be reduced (detuned) since fast response in this case is not really critical. This however, is not possible since the pump operates in ON/OFF
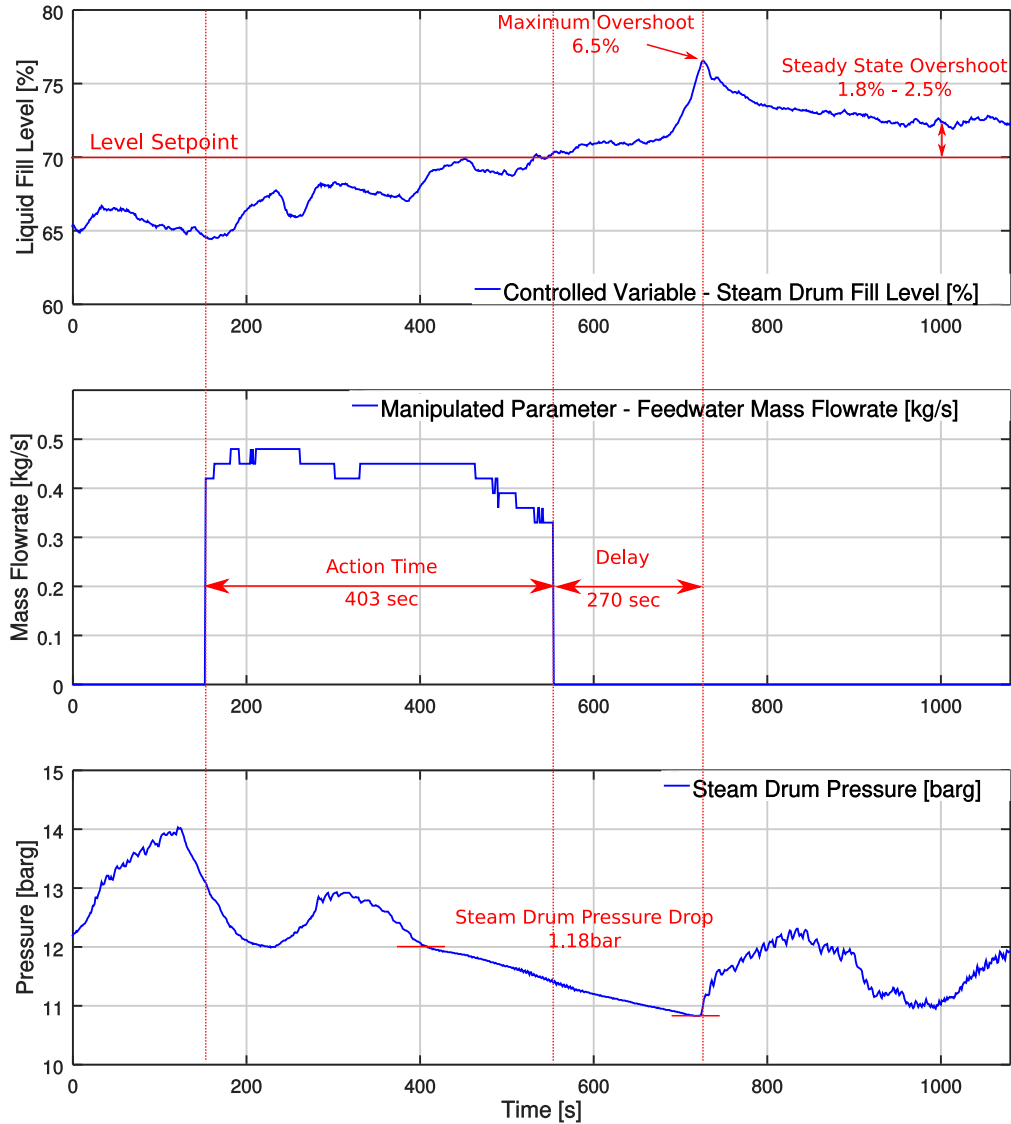
Figure 6.9: Measured response of steam drum level to feed pump ON/OFF operation. Time delay between feedpump shutdown and maximum overshoot in steam drum fill level is experienced. (Average feedwater temperature $= 87.0^oC$. Average steam drum liquid temperature $= 190.4^oC$). (Testing facility : RamPharma).

mode. Therefore, a fixed duty cycle can be used to prevent excessive switching of the pump and giving enough time for the system to respond. This is depicted in Figure 6.10 where the feedpump operates in 50% duty cycle. One can see in the figure that the steam drum level overshoot is minimized and so is the disturbance to the system as seen from the stem

drum pressure.
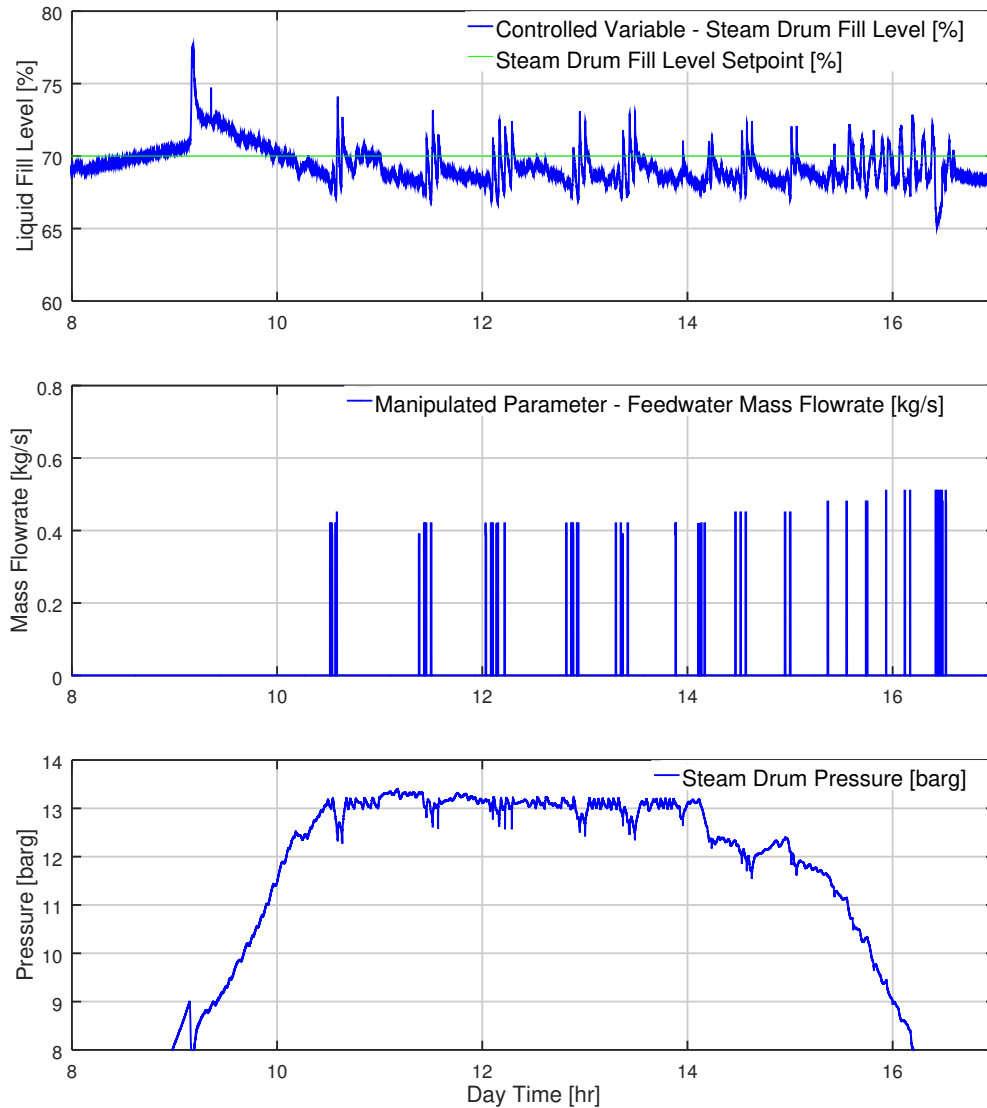
Figure 6.10: Measured response of steam drum level when the feed pump is operated in a 50% duty cycle mode. Duty cycle based operation prevents big overshoot in steam drum level as the system has more time to react. (Testing facility : RamPharma).

The system can be further enhanced by feeding makeup water more smoothly and in a continuous manner as described before to match the steam flow. This implies that there is a pump that can provide the required feedwater mass flow and the required head.

Practically this proves to be a non-trivial problem. This is because

pumps are defined based on head and flow ratings. And certain combinations of low flow and high head are not available in all pump designs. The two main pump options in our case are:

1. Positive Displacement Pumps: these pumps are characterized by an almost vertical flow/head pump curve. Which ideally mean that they can provide their nominal flow rate at any required head. The flow rate is regulated by changing the frequency of the pump. The disadvantage of such a pump for our application is the pulsating nature of the resulting flow, this presents challenges in measuring the resulting flow rate from the pump.

2. Multistage Centrifugal Pumps: these pumps are characterized a more of a horizontal pump curve at least at low flow. These pumps achieve higher head than single stage pumps by having multiple impellers inline. The advantage of these pumps in comparison to positive displacement pumps is that continuous nature of the output flow. Hence, the flow can be easily measured. The problem however is that the high head of these pumps can be only achieved at a minimum flow rate for stable operation. For the RamPharma system shown in Figure 6.10, this flow is already too much and hence the pump has to operate in ON/OFF mode and a duty cycle of 50% [1] Running the pump at reduced speed would not help in this case, because it will also mean reduction in the head of the pump and with the head reduction, the pump wont be able to push against the check valve and the flow will go to zero.

It should be noted here that this problem is project dependent. Depending on the required feed flow and head the problem can be resolved. For example, if the system size is increased while maintaining the operating pressure levels multistage centrifugal pumps will fit the application well. Moreover, other pump types like vane pumps can provide a solution, however, cost constraints have to be considered.

6.1.4 Recirculation Flow Controller

Recirculation flow controller is used to maintain the mass flow rate inside the absorber tubes at the setpoint required by the supervisory controller. The controller is supposed to keep the mass flow rate constant by changing the pump speed continuously.

The mass flow rate inside the absorber tubes is affected by temperature driven density changes. In addition, variations in the pressure drop

---

[1]The duty cycle is defined as the percent of time the pump is turned on over a time interval of 60 seconds. A duty cycle of 50% means that if the controller orders the pump to run, the pump is only turned on for 30 seconds each one minute.

in the system as the flow patterns in the solar field change presents a big disturbance to the recirculation flow controller. (see section 3.2.7).

The major task of the flow controller is to ensure adequate cooling of the absorber tubes under all operation conditions.

The recirculation flow controller receives its setpoint from the supervisory controller depending on the operating conditions. Normally a reduced flow rate is used to save pumping power. However, certain conditions call for increased flow rate to enhance absorber cooling and prevent unfavorable flow patterns.

The recirculation flow controller consists of a PID controller with a feed forward loop to enhance response. The controller also employs anti-windup algorithm.

Figure 6.11 illustrates the operation of the recirculation flow controller. The controller corrects for errors resulting from variation of operation conditions. Severe disturbances, for example resulting from adding cold feedwater to the system as seen in the figure, result in sudden changes in the mass flow rate. The controller however responds by changing the pump speed until the disturbance is finished. One can also notice that this controller does not match the setpoint exactly. That is because it has a special feature in it allowing the controller to stop correcting the error as it approaches a certain region around the setpoint. This is intended to reduces wear and tear on the pump. The RMSE in setpoint tracking for this controller is $\pm 0.031 kg/s$ and the maximum overshoot caused by an external disturbance was $0.22 kg/s$. The controller achieves a good decay ratio after the disturbance of 0.15.
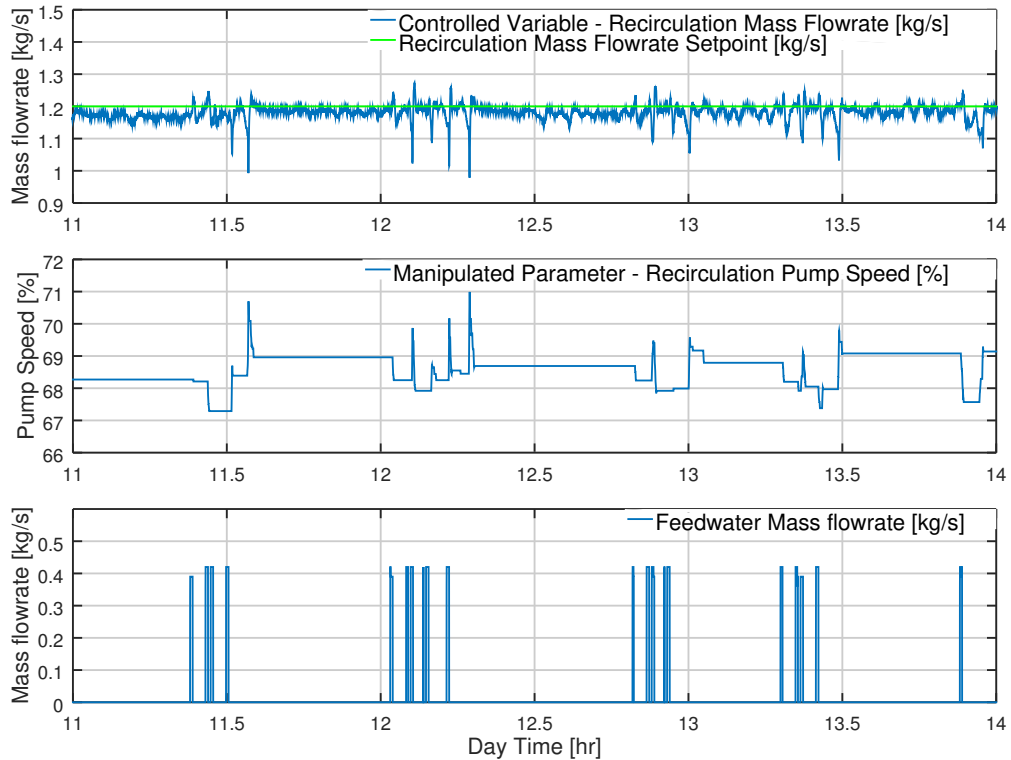
Figure 6.11: Measured response of the recirculation flow controller. The controller manipulates the recirculation pump speed to maintain a constant mass flow rate. Mass flow rate setpoint is $1.2 kg/s$**. (Testing facility: Ram-Pharma).**

6.2 Development and Experimental Testing of a Non-linear Model-Predictive Control with Adaptive Horizon

Model Predictive Control (MPC) emerged in the late 1970s and has been under considerable development ever since [14]. It first became popular in the 1980s though [45]. MPC is a general purpose control scheme that does not impose a specific control strategy but rather a way of thinking which can be translated to several customized control algorithms [14, 59, 45].

MPC has optimal control in its roots. It involves repeatedly solving a constrained optimization problem at each time step. Using current plant states as initial states for the prediction model, an optimal control sequence is generated. The result is a sophisticated feed-forward and feed-back control action. [45, 46]

As the name suggests MPC takes advantage of dynamic system mod-

els to forecast system behavior and optimize the forecast to produce the best decision [38]. MPC deals with the multivariable control problem as a universal problem instead of dealing with each control variable separately as shown in Figure 6.12, where all system inputs are passed to the MPC controller and control actions for all actuators are calculated by the same controller.
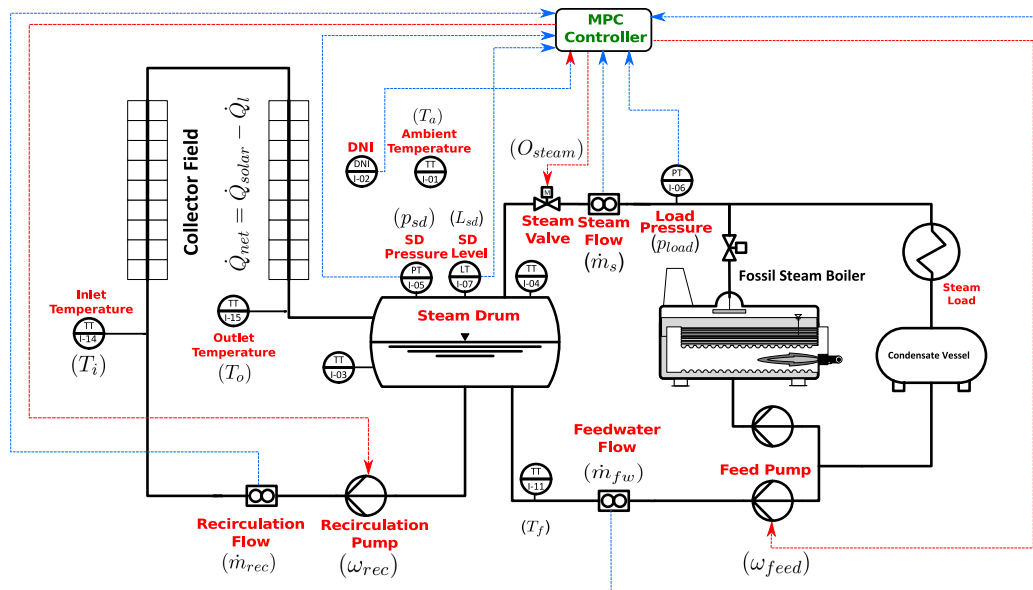
Figure 6.12: MPC controller schematic diagram. MPC controller accepts inputs from several sensors to evaluate the system model at each time step. The controller then provides a comprehensive control action for all actuators taking into account measurements and constrains.

MPC control strategies are based on three main aspects [14]:

1. The explicit use of a dynamic system model.

2. Calculating the control action by minimizing a cost function.

3. Using a receding horizon strategy, which involves continuously moving the prediction horizon to the future.

MPC has many aspects which makes it appealing especially for systems with complex dynamics [14, 59]:

1. The multivariable control case can be dealt with easily.

2. Intrinsically deals with dead time compensation.

3. Measured disturbances are accounted for through the model implicitly. (Feedforward action)

4. Feedback is introduced by estimating the deviation of the model estimates from the measured states.

5. Constraints are dealt with systematically through the solution of the optimization problem. Hence, they are optimally satisfied in contrast to classic control where they are sub-optimally handled using anti-windup or de-tuning techniques [18].

The predictive controller will choose the optimal decision at each time step. Unlike classical controllers which only deal with current inputs and outputs, MPC operates more strategically and might sacrifice immediate gains for future ones.

MPC is a nonlinear control policy that can handle system constraints and several control objectives resulting in a superior control to linear control [45].

The biggest drawback of MPC during development is the need for a suitably complex dynamic model in order to provide a good control action. During operation the biggest hurdle is the need to solve an optimization problem at each time step [45]. This implies using fast algorithms with sufficient accuracy to solve the problem in time.

6.2.1 State Space Models

A convenient way to represent the dynamic model of the system is the state space representation. State space representation lends itself neatly for numerical solution as it is suited for matrix notation. A linear continuous-time state space model consists of two main equations, the state equation and the output equation:

$$
\begin{aligned}
\dot{x}(t) &= \hat{\mathbf{A}}x(t) + \hat{\mathbf{B}}u(t), \\
y(t) &= \hat{\mathbf{C}}x(t) + \hat{\mathbf{D}}u(t) + d(t),
\end{aligned}
\tag{6.5}
$$

where x is the state vector that contains all system states (such as pressures and temperatures) at time t and has the size of $n \times 1$ where n is the number of system states. u is the input (control) vector, which has the size of $m \times 1$, where m is the number of system inputs or outputs. y is the output vector, which has the size of $m \times 1$, d is the system disturbance which has the size $m \times 1$. $\hat{\mathbf{A}}$ is the state or system matrix ($n \times n$), $\hat{\mathbf{B}}$ is the input matrix ($n \times m$), $\hat{\mathbf{C}}$ is the output matrix ($m \times n$), $\hat{\mathbf{D}}$ is the feedforward matrix ($m \times m$) which is often set to 0 .

From the above representation, one can see that the assumption of having a single input single output system (SISO) is not a constraint in the state space representation as is the case for classic control methods. This is a big advantage of the state space representation as it allows us to deal with the system as one unit compared to the classic methods.

In discrete time, the state space representation is converted to:

$$x_{k+1} = \mathbf{A}x_k + \mathbf{B}u_k,$$
$$y_k = \mathbf{C}x_k + \mathbf{D}u_k + d_k, \tag{6.6}$$

where the subscript k represents the kth sampling instant.

Notice that the system matrices ($\mathbf{A}, \mathbf{B}, \mathbf{C}$ and $\mathbf{D}$) in the discrete system are not equal to their counterparts in the continuous time system. There isn't a unique set of discrete matrices either, as they depend on the discretization method used.

Using Equation 6.6 one can estimate (predict) the future states based on the current states and future input sequence:

$$x_{k+1} = \mathbf{A}x_k + \mathbf{B}u_k,$$
$$x_{k+2} = \mathbf{A}[\mathbf{A}x_k + \mathbf{B}u_k] + \mathbf{B}u_{k+1},$$
$$x_{k+3} = \mathbf{A}[\mathbf{A}[\mathbf{A}x_k + \mathbf{B}u_k] + \mathbf{B}u_{k+1}] + \mathbf{B}u_{k+2}.$$

Assume a new vector $\hat{x}_k$, which is evaluated at the time step k. This vector contains all state vectors $x_{k+1|k}$, $x_{k+2|k}$ up to $x_{k+\mathbf{h}|k}$, where $_{|k}$ represents the time step when these values were calculated and $\mathbf{h}$ is the prediction horizon. This vector has the size of $(n * \mathbf{h}) \times 1$. We can also define another vector of input vectors, namely $\hat{u}_k$, which contains the input vectors $u_{k|k}$, $u_{k+1|k}$ up to $u_{k+\mathbf{h}-1|k}$, all evaluated at time step k as well. Using these two new vectors we can show that the state prediction equation becomes:

$$\hat{x}_k = \begin{bmatrix} \mathbf{A} \\ \mathbf{A}^2 \\ \vdots \\ \mathbf{A}^{\mathbf{h}} \end{bmatrix} x_k + \begin{bmatrix} \mathbf{B} & 0 & \cdots & 0 \\ \mathbf{A}\mathbf{B} & \mathbf{B} & \cdots & 0 \\ \vdots & \vdots & \ddots & \vdots \\ \mathbf{A}^{\mathbf{h}}\mathbf{B} & \mathbf{A}^{\mathbf{h}-1}\mathbf{B} & \cdots & \mathbf{B} \end{bmatrix} \hat{u}_k, \tag{6.7}$$

where

$$\hat{x}_k = \begin{bmatrix} x_{k+1|k} \\ x_{k+2|k} \\ \vdots \\ x_{k+\mathbf{h}|k} \end{bmatrix} \quad and \quad \hat{u}_k \begin{bmatrix} u_{k|k} \\ u_{k+2|k} \\ \vdots \\ u_{k+\mathbf{h}-1|k} \end{bmatrix}. \tag{6.8}$$

The model predictive control law is then computed using a cost function defined in terms of $\hat{x}_k$ and $\hat{u}_k$ similar to the following general form: [18].

$$J_k = \sum_{i=0}^{\mathbf{h}} (x_{k+i|k}^T Q x_{k+i|k} + u_{k+i|k}^T R u_{k+i|k}) \tag{6.9}$$

where Q, and R are positive definite or semi definite matrices in case of Q [18]. Mathematically speaking, Equation 6.9 represents a quadratic cost function which is suitable for LTI systems as it results in a convex and smooth optimization problem.

The optimization problem is then defined as

$$
\begin{aligned}
\hat{u}_k &= \underset{u}{\text{argmin}} \ \ J_k, \\
&\text{subject to } g(\hat{u}_k, \hat{x}_k) < 0,
\end{aligned}
\tag{6.10}
$$

where $g(\hat{u}_k, \hat{x}_k)$ is a function that defines constraints.

The previous equations described the predictions and optimization problem for a LTI system in state space representation. The predictions for an LTI system are obtained in the neat matrix notation and in closed form. This however, is not possible if the prediction model is nonlinear as in our case.

Because of the nonlinear dependence of state predictions ($\hat{x}_k$) on the input sequence ($\hat{u}_k$), the cost function $J(\hat{x}_k, \hat{u}_k)$ becomes also a nonlinear function of $\hat{x}_k$ and $\hat{u}_k$ and the constraints $g(\hat{x}_k, \hat{u}_k)$. Thus, the resultant optimization is nonlinear and nonconvex and therefore significantly more challenging [18, 17].

As a result there is in general no guarantee that the optimizer will converge to a global minimum. Moreover the time required to find a local solution is typically much longer compared to linear systems of the same size [18, 17].

A more general formulation of the non-linear time invariant system we are dealing with is given in Equation 6.11:

$$
\begin{aligned}
\dot{x}(t) &= f(t, x(t), u(t)), \\
y(t) &= g(t, x(t), u(t)) + d(t).
\end{aligned}
\tag{6.11}
$$

The system equations described by Equation 6.11 are derived from the model introduced in section 4.2.9, where the state vector x is given by:

$$
x = \begin{bmatrix} x_0 \\ x_1 \\ x_2 \\ x_3 \\ x_4 \end{bmatrix} = \begin{bmatrix} p_{sd} \\ M_d \\ \alpha_d \\ M_r \\ \alpha_m \end{bmatrix},
\tag{6.12}
$$

and the system inputs are arranged in the inputs vector u as follows:

$$
u = \begin{bmatrix} u_0 \\ u_1 \end{bmatrix} = \begin{bmatrix} \dot{m}_s \\ \dot{m}_{fw} \end{bmatrix}.
\tag{6.13}
$$

The output vector y can be freely chosen based on the controlled variable. In this system the output vector y is defined as:

$$
y = \begin{bmatrix} y_0 \\ y_1 \end{bmatrix} = \begin{bmatrix} p_{sd} \\ M_d + M_r \end{bmatrix}.
\tag{6.14}
$$

6.2.2 Adaptive-Horizon Non-Linear MPC Algorithm

The MPC Algorithm has two main components at its core, the model and the optimizer. The optimizer uses the model to predict the optimal inputs (control actions).

As seen in Figure 6.13, the algorithm starts off with initial conditions of the states $(x(0))$ and initial inputs $(u(0))$. The next step is to evaluate the model for the current time step to find out $y_m(k)$. $y_m(k)$ is the output vector calculated by the model based on the current state and inputs:

$$y_m(k) = g(k, x(k), u(k)) + d(k), \tag{6.15}$$

here, $d(k)$ is the disturbance estimate. The disturbance estimate is calculated from the previous time step by subtracting the output vector calculated by the model $y_m(k-1)$ from the measured value of the actual plant output $y_p(k-1)$. The disturbance estimate $d(k)$ is given by:

$$d(k) = y_p(k-1) - y_m(k-1). \tag{6.16}$$

Notice that the disturbance estimate is a method used to account for modeling errors and for actual unmeasured disturbances by comparing the measured plant output to that calculated by the model.

When the disturbance estimate is calculated, the MPC Engine is called. The current states and the disturbance estimate are passed to the MPC Engine.

In the MPC Engine, the optimization problem is solved using the model for the current time step. An action plan for the full prediction horizon is produced and returned in the form of a vector of input vectors: $[u(k+1), u(k+2), u(k+3), ..., u(k+\mathbf{h})]$. The controller applies the first control actions of this plan to the actual system.

At the next time step, the horizon is shifted forward $(k = k + 1)$ and the plan is updated taking into account new measurements (feedback) and measured disturbances estimates (feedforward). The controller then applies the first control actions of the updated plan, and so on.

6.2.3 Implementation of Adaptive-Horizon Non-Linear MPC

The implementation of the MPC control is complicated compared to classical controllers. For instance, PID control law is based on the idea of model-less control, MPC however, has model-based control in its core. The calculation of the control law for a PID controller is very well suited for industrial controllers as it only involves the calculation of numerical derivatives and integrals during runtime. These calculations are simple enough for a very small and slow microcontroller to perform.

MPC on the other hand, involves a model which is being used to drive the states to the desired values by optimizing the inputs over the prediction
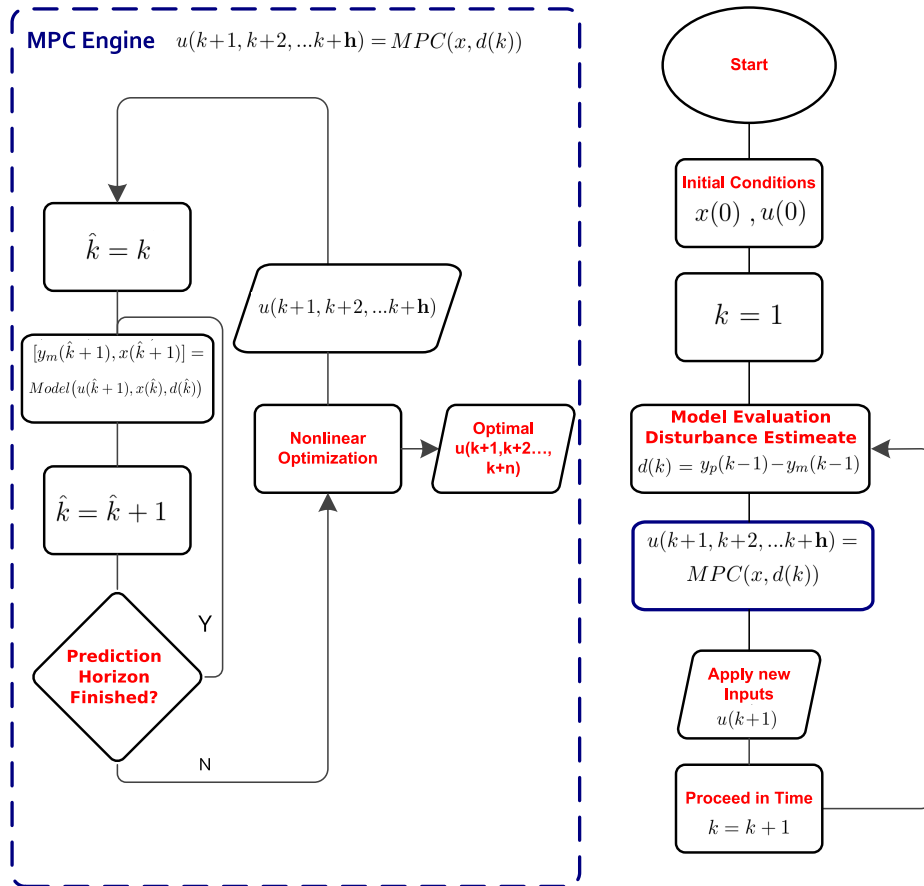
Figure 6.13: Flow chart of the MPC controller algorithm. Left: Schematic of the MPC engine. Right: Flow chart of the main control algorithm.

horizon. In it simplest form, where the model is linear and the optimization cost function is quadratic, the optimization problem is convex [14] and a closed form solution may be found, which makes the computation simple.

This isn't always the case. When the model is not linear or cannot be linearized, non-linear MPC is to be used. In this case both the evaluation of the model and the optimization problem get very complicated for any manual operations and numerical solutions are inevitable. This leads to the high computational power needed for MPC controllers.

Luckily with modern computing power, which is also finding its way slowly to the industry, the problem is mitigated.

The first trials with MPC were done using `Octave` which was quick enough for the simplest form of the MPC controller. But for the full model, the DAE solver `daspk` and the `SQP` optimizer had to be used which made the

time stepping too slow to be usable. In some trials the calculation needed for a time step of one second took more than twenty seconds. Another trial with `Octave` was done by trying another solver namely `fsolve`, but the enhanced performance has shown not to be sufficient.

Therefore the algorithm had to be translated to `C`. This required the translation of all the subroutines and searching for new libraries for the optimizer, the solver and water properties. At the end, the resulting code has shown approximate 100 times faster in execution and hence suitable for usage in realtime.

The main components of the MPC implementation on `C`, which contribute to the main portions of the computation times and the programming effort are listed below:

1. Solver: The solver is used to solve the system of nonlinear equations which results from the system model as described in Sections 4.2.8 and 4.2.9.

   The solver is used to provide predictions for the system states along the prediction horizon based on the inputs suggested by the optimizer. At each time step, the solver is run by the optimizer between several hundred times to a couple of thousand times until the optimizer finds the minimum cost point. Hence it is essential to have a quick solver to perform the calculation. The package `MINPACK` from `CMINPACK` [23] is used as a solver here. `MINPACK` includes software for solving nonlinear equations and nonlinear least squares problems [23]. `MINPACK` was originally written in `FORTRAN` by Jorge Moré, Burt Garbow, and Ken Hillstrom from Argonne National Laboratory [50]. The `FORTRAN` version was translated to `C` by Manolis Lourakis using the `f2c` library. Devernay, Frédéric enhanced the `f2c` version and released the current `CMINPACK` version which we use here [23] .

2. Optimizer: The optimizer is used to minimize the cost function defined by the control law. Most importantly, the cost function is formulated to penalize deviation from the setpoint. This is discussed in more detail in Section 6.2.4.

   Because of the non-linearity of the model, non-linear optimization algorithms are to be used. In this work, the `NLOPT` [39] library was chosen for optimization, which is an open-source library implemented in several languages including `C/C++`. The library contains several optimization algorithms for non-linear optimization. The optimization algorithms being used in this work are mainly derivative-free algorithms which where originally developed by M. J. D. Powell [55] and later implemented in `NLOPT` by [39]. One of the algorithms which was seen to be fast compared to other routines is the `BOBYQA` algorithm which stands for Bound Optimization BY Quadratic Approximation. `BOBYQA`

is used for bound constrained optimization without the need to calculate gradients of the cost function. `BOBYQA` performs the minimization using an iteratively constructed quadratic approximation of the cost function. The other algorithm which was also developed originally by M. J. D. Powell [54] is the `COBYLA` (Constrained Optimization BY Linear Approximations), which uses linear approximations. This routine was found to be slower at convergence but more stable during real time runs.

3. Properties Calculation: water properties evaluation represents a challenge because it is a time consuming process that normally involves linear interpolations of the property correlations. In this work the `freesteam` library is used. `freesteam` is an open source implementation of international-standard IAPWS-IF97 steam tables from the International Association for the Properties of Water and Steam (IAPWS). The code for `freesteam` was written as a part of the work done by John D. Pye in his dissertation [58]. Although the library includes differential properties but some accuracy issues were noticed, so these properties were calculated from other properties.

6.2.4   Description of the Adaptive-Horizon Non-Linear MPC

The Prediction Horizon

The prediction horizon is a key component of MPC and is hence essential to define correctly. The prediction horizon defines how far into the future should the controller look and predict states and control actions. The prediction horizon should be long enough to include the main dynamics of the system. If the prediction horizon is too short, the controller fails to respond to the dynamics early enough. A prediction horizon which is too long is not recommended either as it increases the computational time.

Receding Horizon

The idea of receding horizon is that we always update our predictions and decision making to make use of the most recent measurements and setpoints [59]. The concept of receding horizon is core in MPC that it is sometimes called Receding Horizon Control [45].

At each time step k, the controller evaluates the state prediction vector $\hat{x}_k$ and the input sequence $\hat{u}_k$ for the whole horizon, but only the first elements of the optimal input sequence are used, i.e those corresponding to time step k. The process of computing $\hat{u}_k$ by minimizing the predicted cost and implementing the first element of $\hat{u}_k$ is then repeated at each sampling instant. As time progresses by one step, the prediction horizon shifts to

the future by the same amount leaving its length constant. Therefore the approach is known as a receding horizon strategy. [18]

Since the state predictions $\hat{x}$ and the optimal input sequence $\hat{u}$ depend on the current state measurement x_k, this procedure introduces feedback into the MPC law, thus providing a degree of robustness to modeling errors.[18]

The Cost Function (Performance Index)

The MPC controller requires a performance index according to which it will steer the process. The performance index represents the cost function used by the optimizer. The choice of the performance index is essential in establishing the stability and computational load of the control law.

The optimization problem for MPC is typically a multi-objective optimization. For simplicity a weighted sum of the various cost functions is minimized. The tuning of the MPC controller is done by modifying the weights of the cost function. There aren't any solid rules for the cost functions to be used with MPC. However, the cost function should be constructed so that the model converges to the required states. At the same time, it is important that the cost function remains smooth and as simple as possible so that the optimization algorithm converges.

The cost function for a multi-input multi-output problem can be constructed as a sum of different terms or cost functions. Some of the common choices of cost functions in MPC are [59]:

1. Deviation of states from the setpoint. $J_1 = r - y$.

2. Rate of change in the inputs. $J_2 = \Delta u$.

3. Deviation of inputs from steady state inputs. $J_3 = u_{ss} - u$.

4. Deviation of inputs from current inputs. $J_4 = u_o - u$.

5. Deviation of current states from the setpoint (current errors). $J_5 = r - y(k)$.

The first cost function J_1 penalizes the deviations of the states from the setpoints. This cost function is perhaps the most important. Based on this cost function the inputs are chosen by the optimizer to achieve the minimum deviation of the states from the setpoints along the prediction horizon. This cost function implicitly includes a feedback component since the predictions are typically corrected using a disturbance estimate which is discussed later.

Although J_1 is a very important part of the cost function, including it alone will result in excessive corrections and will quickly saturate the actuators trying to correct the states as soon as possible. This is neither practical

nor desirable. In order to prevent excessive input changes that result in actuator wear and tear, another cost function is typically used. This can be any of the other cost functions J_2, J_3, J_4 or J_5.

Hence the final cost function is given in Equation 6.17.

$$J = \sum_{i=1}^{H} a_1(r-y) + a_2(\Delta u) + a_3(u_{ss}-u) + a_4(u_o-u) + a_5(r-y(k)), \quad (6.17)$$

where a_1 to $a5$ represent the weights of the cost function terms. Notice as well that although H is typically equal to the horizon length (h), it should not necessarily be. In fact, each term can have a different summation length.

The Disturbance Estimate

The main complexity of MPC control comes from the model used. While accurate and high order models are desirable to achieve good state predictions, it comes at the cost of higher modeling effort, increased computational load and possibly stability and robustness. Hence, the MPC model is generally a compromise between accuracy and complexity.

To that end, most practical model predictions have a deviation from the actual states which result from modeling inaccuracies, nonlinearities, parameter estimation errors and unmeasured disturbances.

To correct for these deviation, at each time step, a disturbance estimate is calculated for the output(s) using the measured output and the model output.

$$d = y_p(0) - y_m(0), \quad (6.18)$$

where d is the disturbance estimate, y_p is the actual plant output, y_m is the model predicted output. Notice that the disturbance estimate is calculated for using the current time step values but is applied for all the predictions along the horizon. The disturbance estimate is also update at each MPC time step. Notice as well that Equation 6.18 is used for all outputs, where a disturbance estimate for each output can be evaluated.

Disturbance estimate is a key component of MPC control law as it ensures unbiased predictions [59]. It also provides the needed feedback path for the MPC controller.

The Constraints

Constraints handling is one of the biggest advantages of MPC. In classic control, constraints which typically arise from actuator or plant operating limits, are typically not taken into account in the control law itself, they are rather dealt with after the control law evaluation. This means that the controller does not really know of these constraints. This often results in very

common problems like wind-up for example, which are not trivial and have to be handled properly. Often handling these issues is more important than the control law itself.

MPC however presents a neat, standardized and systematic way to handle constraints by including them in the optimization algorithm. This means that the controller will take the system constraints into account when evaluating the next control action. Moreover, constraints can have a positive effect on the optimizer since it reduces the search domain and hence can make the optimization process much faster.

Adaptive-Horizon Non-Linear MPC

Modern numerical differential equations and differential algebraic equation solvers feature adaptive stepsize. In fact Press et al. [57] recommend the use of "adaptive stepsize control" and describe its use for a Runge-Kutta ODE solver. Solvers with adaptive stepsize typically monitor how errors evolve and try to increase the stepsize when possible, and reduce it when needed. The Non-Linear MPC (NMPC) requires the solution of a system of differential equations each time step, however it cannot allow for variation of time stepping within each run. Therefor off the shelf adaptive stepsize algorithms are not suitable for this application.

To overcome this hurdle, a new technique is suggested in this work. Instead of changing time stepping during the solution run, the horizon length is changed.

Initially, the solver starts with the default horizon length ($200s$) and step size ($20s$). As the algorithm runs, the controller monitors the if the solver fails to converge. When the solver diverges, the step size is reduced to $2s$ and the horizon length is reduced to $20s$. The algorithm will get back to the default values after the solver converges for more than sixty times.

The suggested method was tested in several situations and was seen to successfully avoid solver crashing and hence increased controller stability.

Since the method relies on horizon length adjustment, the controller is called Adaptive-Horizon NMPC.

Controller Tuning

The tuning of the MPC controller is done using the cost function weights. The choice of the cost function will determine how the controller reacts to changes in the system states. The cost function that resulted in best results during the experimental trials contained four terms as seen in Equation 6.19:

$$
\begin{aligned}
J = \sum_{i=1}^{H} & a_1(r_0 - y_0)^2 + a_2(u_0(k) - u_0)^2 \\
& + a_3(r_1 - y_1)^2 + a_4(u_1(k) - u_1)^2,
\end{aligned}
\tag{6.19}
$$

The first and second terms are quadratic error terms of the steam drum pressure and the total water mass in the system, respectively. These terms are a summation of the current error and future errors predicted by the model. Hence the feedback component of the MPC controller is embedded in these terms. The other two terms are a penalty for changes in inputs, they serve as a damper to quick changes in inputs. This increases system stability and reduces wear on actuators.

6.2.5 Results and Comparison with PID based Controls

In this section the results from operating the testing facility in Freiburg Hochdorf using the Adaptive-Horizon NMPC controller are presented. The Adaptive-Horizon NMPC controller has been operated in several operating conditions including sunny and cloudy days. The cost function used for these tests is given by Equation 6.19. During the tests, two sets of tuning parameters have been used which are summarized in Table 6.3:

Table 6.3: Summary of Adaptive Horizon NMPC tuning parameters

Test Results of	a_1	a_2	a_3	a_4
Figure 6.14	0.022	3.00	5.00×10^{-6}	0.2
Figure 6.15	0.022	5.00	5.00×10^{-6}	0.4
Figure 6.16	0.022	5.00	5.00×10^{-6}	0.4

Setpoint Tracking

Figure 6.14 depicts the DSG system response using the Adaptive-Horizon NMPC. The top graph depicts the measured steam drum pressure which is the first controlled variable in this test (x_0). The second graph from top depicts the measured steam drum liquid fill level. The third graph depicts both manipulated parameters of the system, namely feed pump speed in blue and steam valve opening in red. And finally the bottom graph depicts measured DNI during the test.

The test was performed in a sunny, cloud free day as can be see from the figure. During the measurement the DNI has remained close to the average of $858W/m^2$. As can be seen from Figure 6.14, the controller maintains the pressure of the steam drum steady at different setpoints. The controller demonstrated a smooth transition between setpoints with a peak overshoot of merely $0.05bar_g$ corresponding to a POR of only 2.5%. This came at the cost of a longer rise time reaching up to $340s$. The controller manages to keep the pressure within $\pm 0.1bar$ of the setpoint. The RMSE

in steam drum pressure control from $t = 13.75hr$ to $t = 14.75hr$ was only $\pm 0.027bar$.
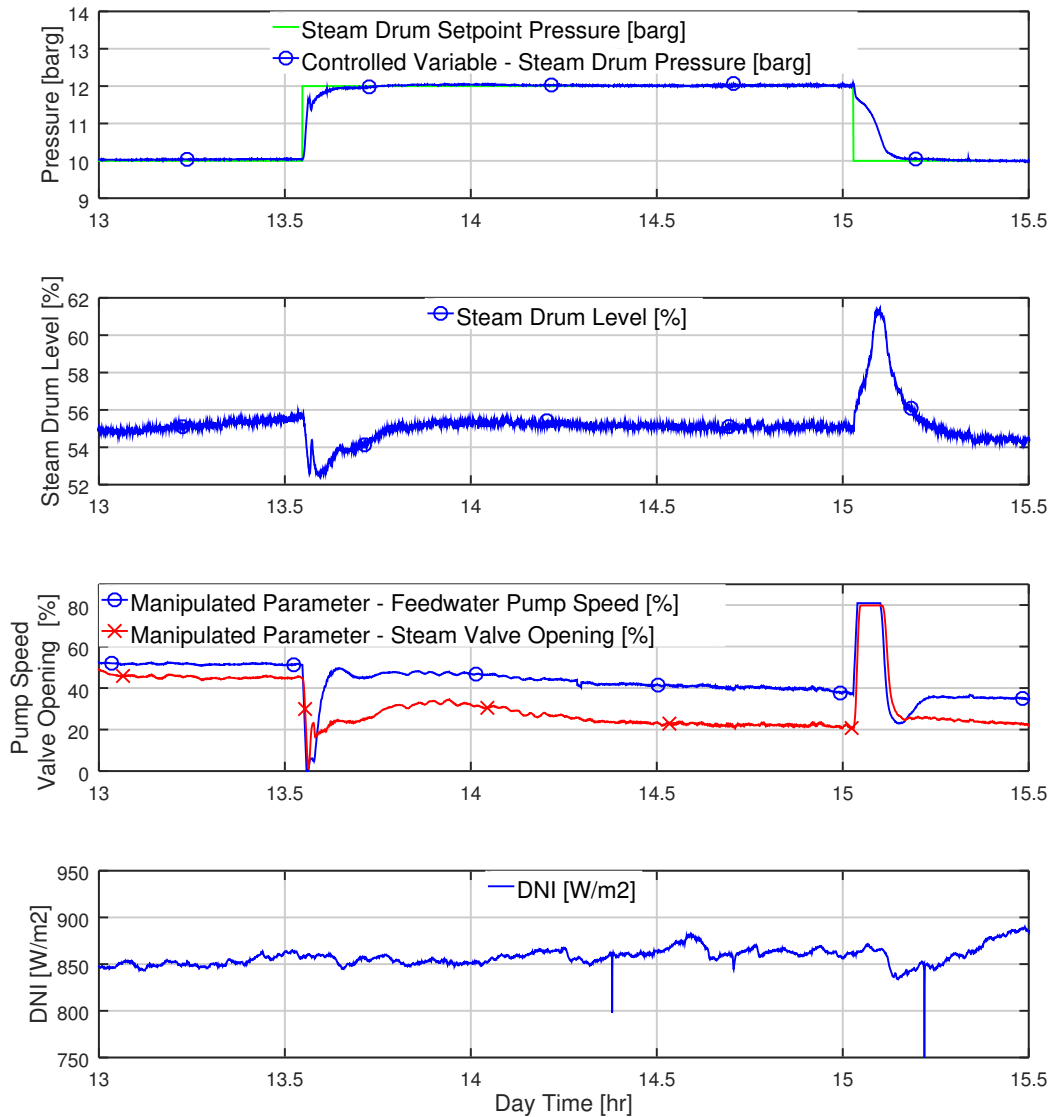
Figure 6.14: Measured response of DSG system control using Adaptive-Horizon NMPC. Controlled variables are steam drum pressure and the total water mass in the system. The actuators are the steam exit valve and the feed water pump. (Testing facility : Hochdorf).

Notice that lowering the pressure from $12bar_g$ to $10bar_g$ is slower than rising the pressure, since lowering the pressure quickly requires a high steam mass flow which saturated the load.

The second controlled variable is the total water mass in the system. This variable is actually a combination of two state variables, namely, water

mass in the steam drum (x_1) and water mass in the absorbers (x_3). This controlled variable cannot be directly measured and can only be estimated.

Under steady boundary conditions one can assume that the water mass in the absorbers is steady. Therefore, the steam drum liquid fill level depicted in Figure 6.14 can provide insight into the performance of the system mass control. Between $t = 13.75hr$ to $t = 14.75hr$ the system boundary conditions did not change and during that time the steam drum level was maintained around the average value with a total RMSE of only $\pm 0.16\%$. This suggests that the NMPC controller successfully maintains the mass balance in the system.

From Figure 6.14, one can also notice a slight decreasing trend in the steam drum level between $t = 13.75hr$ to $t = 14.75hr$. This is caused by the decrease in collector power as the sun elevation angle decreases with time. This causes less steam to be in the absorber tube, which in turn means that more liquid water is used from the steam drum.

Dealing with Nonlinear Dynamics

A very important aspect of NMPC control is that it reacts according to the system model and not merely to measured outputs. This can be demonstrated in Figure 6.14 when the pressure setpoint is changed. The abrupt increase in steam drum pressure results in steam drum level to drop. And vice versa, a decrease in the steam drum pressure results in an increase in the steam drum liquid level which is larger in magnitude compared to the level drop because of the swelling effect.

A conventional PID controller is not capable of dealing with such nonlinearity. When the steam drum level drops, a conventional PID controller tries to counteract the drop by increasing the feedwater flow, but as the transience is over, the steam drum will be over filled. The NMPC controller however, stops the feedwater flow as the level drops. The opposite is seen when the pressure drops. As the level increases, the NMPC turns on the feedpump to full speed and hence manages to maintain the steam drum level after the transience. In both cases the NMPC controller reacts correctly and counter intuitively

Integrated System Control

Contrary to PID control, NMPC does not associate an actuator to each controlled variable. For example, although its intuitive that the steam drum pressure is mainly affected by the steam exit valve, the steam drum pressure is also affected by the feed water flow. This interdependency of system states, inputs and outputs are not considered in PID controlled, but is key in NMPC, which considers the effect of each input on all system states and outputs. (see Figure 6.12.)

Cloudy Conditions

During cloudy conditions, the sudden change in solar irradiation has a tremendous effect on the stability of the numerical model solver. Such rapid changes typically require the numerical solver to adjust the time-stepping. For simulations and non-realtime application this is typically a feature of modern differential equation solvers, but is not suitable for real-time applications. To avoid this instability an adaptive prediction horizon is used in the NMPC controller.

As can be seen in Figure 6.15, during mild changes in solar irradiation between $12.0hr$ and $13.6hr$, the controller shows a tracking accuracy of $\pm 0.04bar$ (RMSE). As the solar irradiation changes afterwards because of passing clouds, the pressure in the steam drum fluctuates. The controller however manages to restore the pressure when the irradiation level goes back to normal.

One can also notice that the steam drum level stabilizes after the irradiation disturbance. However, it has a steady decrease as the collector optical power decreases at the end of the day (although DNI remains high). This is explained by the fact that more and more liquid is transferred from the steam drum to the absorber when the collector power drops. This happens because the steady state average steam quality in the absorber is proportional to the net collector power, and hence the lower the collector power the lower the steam quality and so more liquid is present in the absorber. This liquid can only be drawn from the stream drum. So although the total water mass in the system is constant, the amount of water in the steam drum is reduced.

Figure 6.16 shows the performance of the controller when high clouds are present. At the beginning of the test period at $12.0hr$ the irradiation is steady and only attenuated by high clouds. At the period until $12.6hr$ the pressure and steam drum level are stable. Later the collector power starts dropping slowly because of the increased cloud cover, however the controller manages to maintain good setpoint tracking for both water content and pressure and at different setpoints. Shortly after $13.8hr$ the irradiation drops to a very low value that the controller cannot maintain the pressure anymore and the steam exit valve is shut completely.
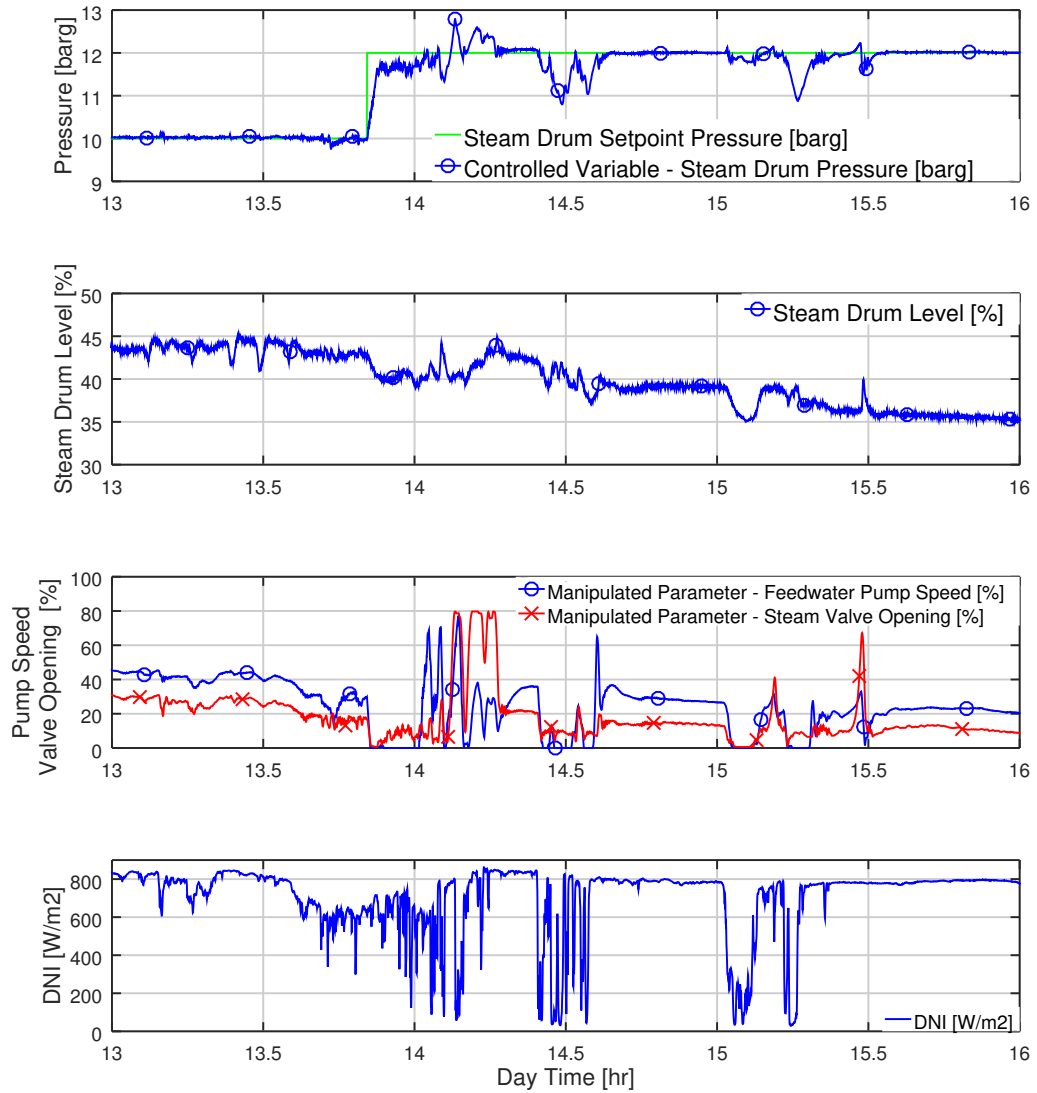
Figure 6.15: Measured response of DSG system control using Adaptive-Horizon NMPC during cloudy conditions. Controlled variables are steam drum pressure and the total water mass in the system. The actuators are the steam exit valve and the feed water pump. (Testing facility : Hochdorf).
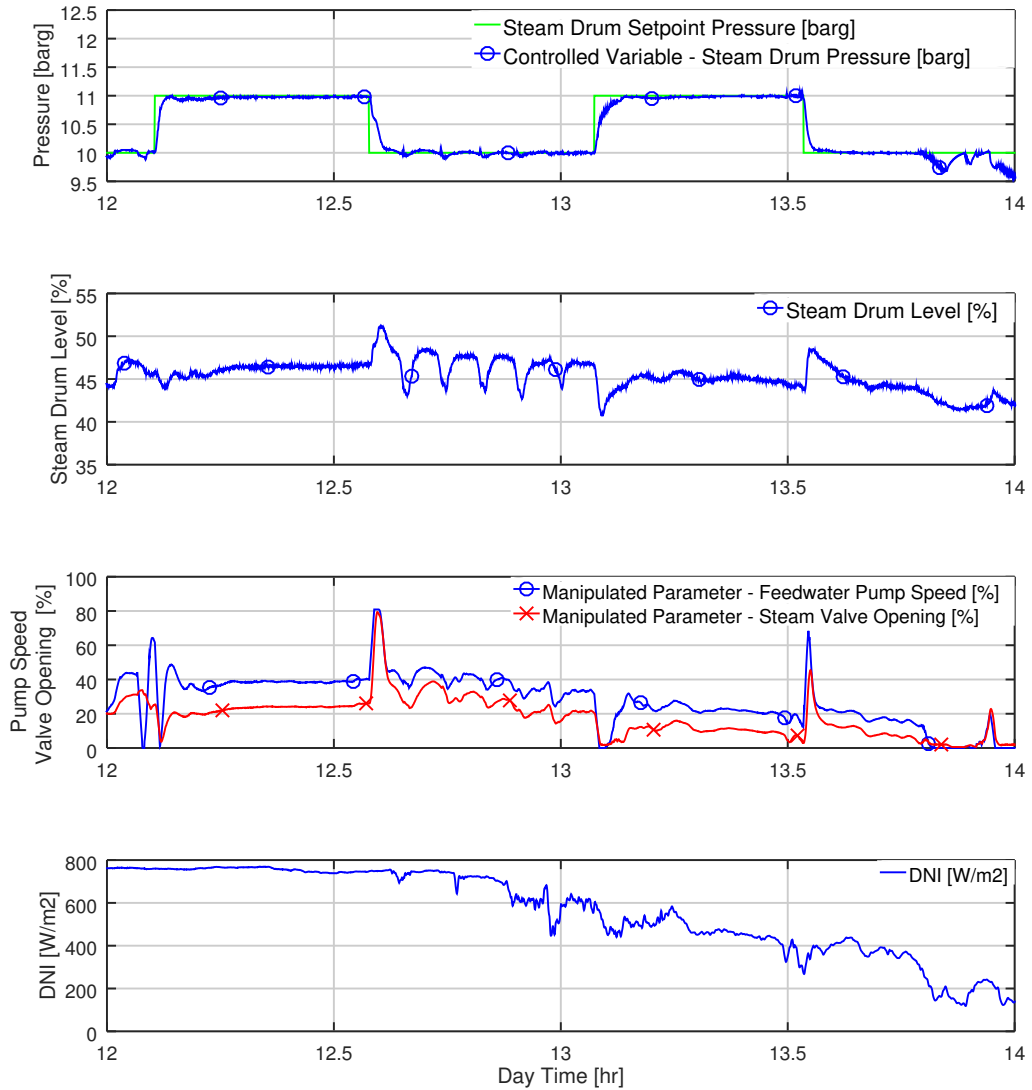
Figure 6.16: Measured response of DSG system control using Adaptive-Horizon NMPC when high clouds are present. Controlled variables are steam drum pressure and the total water mass in the system. The actuators are the steam exit valve and the feed water pump. (Testing facility : Hochdorf).

6.3 Summary

The DSG system is a multi-input multi-output (MIMO) system. One can either adapt classic control methods designed for single-input single-output (SISO) systems, or use control methods that can handle MIMO systems. In this Chapter, both alternatives are used.

The first control system developed is based on PID controllers which encompassed three main controllers, namely, recirculation flow, supply pressure and level control. To overcome the shortcomings of PID controllers as is evident from early experiments, several modifications have been made on the controllers structure. These included several advanced techniques like, feed-forward control, exception handling, setpoint scheduling and windup control. The resulting control system has been thoroughly tested in the test facility and eventually deployed in commercial operation for the first time in March-2015. The system is completely automated and requires no operator intervention. The controller has been also recently implemented in another new commercial DSG plant in Jordan.

The modified PID controllers exhibited satisfactory control performance. The most important of which is the pressure controller which is shown to provide good setpoint tracking accuracy reaching $\pm 0.015 bar$. The controller has also shown a good POR of merely 14% and a quick response with a rise time of $106s$. To handle unique system dynamics and nonlinearities, the pressure controller is designed with several special features like low supply pressure, over pressure protection and anti-windup algorithm.

The PID level controller is also shown to successfully deal with system non-linearities. In level control the focus is not on maintaining the setpoint tracking accurately but rather on avoiding large deviations from the setpoint caused by disturbances. The controller is designed with an adaptive setpoint algorithm to deal with system dynamics. The recirculation mass flow controller illustrated good disturbance rejection performance with a maximum overshoot of $0.22 kg/s$ after a disturbance event. The decay ratio after the disturbance is only 0.14. The controller also manages to keep the flow rate around the setpoint with an accuracy of $\pm 0.031 kg/s$.

Driven by the need to reduce time needed for controller tuning required for PID controllers and the appeal of a universal controller that takes into account system dynamics, MPC has been investigated. An NMPC control system is designed and implemented in the testing facility in Hochdorf. The control system is based on a model used for drum type steam boilers which is adapted to fit the application.

The preliminary results from the test facility have been promising. The NMPC is able to provide good control accuracy of the steam drum pressure reaching an accuracy of $\pm 0.0271 bar$ and a POR of only 2.5%. The results demonstrate that control system takes "wiser" decisions compared to the PID based controller without having to add exceptions for each single

special situation, especially in level control.

Chapter 7

Conclusions

Solar thermal energy is yet to significantly penetrate the industrial sector. Technical hurdles related to the controllability and reliability of solar thermal installations are a major concern. In this thesis, the control problem of concentrated solar thermal plants is addressed where the work was developed on linear Fresnel collector plants.

The first group of control strategies treats the temperature control problem in single phase flow systems. Several control methods where developed depending on the application and developed controllers exhibited stability and robustness during operation.

It is shown that using enhanced PID controllers with properly designed feed forward control loops give good results. The most suitable controller included a feed forward loop that incorporates a collector model which is also developed within this work. The model is based on DNI measurement to evaluate the available solar power. The controller managed to track the temperature setpoint with an accuracy of less than $\pm 0.5^{o}C$. Thanks to the feed forward term, it is also shown that the controller manages to react to disturbances in solar irradiation before it affects the outlet temperature.

The performance of the enhanced PID controller shows that the development of a more complex controller is not necessary.

The second group of control strategies tackle the control problem in DSG mode. The control problem in DSG is more complicated due to the multivariable nature of the system. For this system two approaches were developed and tested under real life conditions. First the PID based control strategy and second the MPC based control strategy. For both control strategies, a unique set of detailed experimental data is presented to help in future development.

The PID based control strategy was shown to work reliably both in the testing facility and in commercial operation. The controller was shown to track the pressure setpoint accurately with a root mean square error of merely $\pm 0.15 bar$ during normal operation conditions, and down to $\pm 0.015 bar$

147

when the variation in steam demand is minimized. The controller was also shown to control all other operation parameters like, recirculation mass flow rate, liquid level in the steam drum and operating pressure and temperature within the safe operation limits even under heavy disturbances.

The PID based control strategy represents the current market ready control strategy for DSG operation. However, the main disadvantage of this control strategy is the time consuming process of designing, tuning and commissioning of the controller.

The second control approach is based on the MPC method. The main driver behind the development of this control strategy is to come up with a universal control law that is able to handle all controlled variables, input parameters, and plant constraints as one single controller. This way the interdependency of system variables are intrinsically taken into account. A reduced version of this method has been successfully developed and implemented in the testing facility which proved that the concept feasible. Further development is still needed however to take this control strategy to commercial implementation.

A detailed experimental study was conducted to investigate the dynamics of DSG systems. Such detailed study is completely missing from literature and will serve as a valuable reference for other workers in the field. The study was also supported by direct measurement of flow patterns a the outlet of the absorber tube using a wire mesh sensor.

The main finding of this research is that in spite of the inherent complexities of solar thermal plants, with properly designed systems and controllers, a solar thermal plant can become a reliable and robust source of thermal energy. Even in the most demanding sectors, like the industrial sector.

Chapter 8

Outlook

The control problem in single phase flow mode is complicated by system dead-time and outside disturbances. It is recommended that future work focuses on this issue especially for large installations where the problem of dead-time is amplified. It is worth noting that designing systems in a way to reduce disturbances, especially from inlet temperature variations, can greatly enhance controllability and robustness. Furthermore, DNI measurement is crucial for the success of the control strategy, not only that it represents a big contribution in model uncertainty, but it also decreases system robustness. Therefore, enhanced instruments with good accuracy and better soiling tolerance (e.g. variants of the rotating shadow band pyranometer) are needed.

The operation of the Fresnel system in direct steam generation mode can be challenging during transience as was evident throughout this study. Better understanding of transient phenomena can be achieved by developing accurate models of the system which can be then used to develop simpler models suitable for control purposes. Several areas of further research in direct steam generation were identified during this work as follow:

- Development of a detailed system model that can increase the accuracy of Model Predictive Controllers while maintaining simplicity. This includes enhancements of the numerical solution of the optimization problem to improve controller robustness and speed of the solution.

- Flow patterns prediction during steady state and transient

- Heat transfer evaluation at different locations in the absorber tube based on flow pattern. Including a heat transfer model in the control system can help in preventing overheating incidents.

- Modeling pressure drop variation across the collector field depending on flow pattern. This is important in order to be able to balance the flow rates in different parallel evaporation loops.

Appendices

Appendix A

The Wire Mesh Sensor

The Wire Mesh Sensor (WMS) developed by the Helmholtz-Zentrum Dresden-Rossendorf (HZDR) is used for the study of transient two-phase flow. The sensor provides gas fraction distributions in space and time. Compared to X-ray or γ-ray tomography, the WMS represents an affordable and more simple method for investigating transient two-phase flows. [56]

The WMS is typically constructed of two electrode meshes of 16 equidistant wires (see Figure A.1). The meshes are arranged so that the electrodes of the two meshes are perpendicular resulting in a grid of 16×16 sensitive crossing points distributed equally over the pipe cross-section. The two meshes are $2mm$ apart, one mesh is used as a transmitter and the other is used as a receiver.[56]

During measurement one of the transmitters is activated by energizing it through a square wave with zero DC offset. The zero offset ensures that there is no electrolysis taking place around the electrode. The square wave is sensed by the receiver and the amplitude of the signal indicates the resistance of the medium between the transmitter-receiver. During the measurement other sensor transmitter pairs are grounded to minimize crosstalk.[56]

Since the WMS depends on conductivity measurement, the liquid phase conductivity should not be less than $0.01\mu S/cm$. The sensor and data acquisition system are capable of performing a measurement at a frequency of 10,000 frames per second for a maximum period of 1966 seconds.[63]

Thanks to recent development the wire mesh sensor can reach higher temperatures and pressures . This enabled us to use them for measuring two-phase flow at the Fresnel collector outlet. The current models can reach up to $286^{o}C$ and $7.0MPa$ [53].

The recorded values are a 12-bit representation of conductivity at the region of each crossing point of receiver and transmitter wires. Since conductivity is affected by temperature, the sensitivity of the sensor changes at different temperature levels. To cope with this, the gain of the data acqui-

151
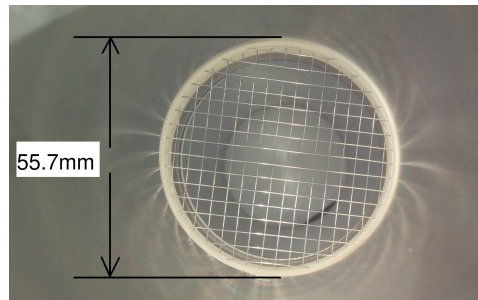
Figure A.1: Wire Mesh Sensor internal view.

Figure A.2: Wire Mesh Sensor installed.

sition electronics should be adapted to prevent saturation in the electronics on one hand and small signals on the other hand. The gain of the data acquisition system is thus modified in the software so that the measured signal remains between 60% and 80% all the time.

Moreover, it is also necessary to perform a calibration measurement at different operating conditions. The calibration measurement is used to correct the difference in sensitivity between different nodes. This is achieved by making a measurement with liquid only in the sensor. The measurement is done with high time resolution reaching 10,000 frames per second. The measurement time is 10 seconds. The average of all 100,000 calibration frames is then taken resulting in a 16×16 calibration matrix.

The actual measurements are done at a lower frequency, typically 1kHz. The calibration matrix is then used with the measurement data to calculate

the void fraction matrix of the tube cross-section. The void fraction matrix is a 16×16 matrix that has zero when there is pure liquid and has one when there is pure gas. The void fraction matrix is calculated using Equation A.1.

$$Void\ Fraction = 1 - \frac{M_{i,j}}{C_{i,j}} \tag{A.1}$$

where M is the measurement matrix and C is the calibration matrix.

The void fraction matrix is then used to illustrate the liquid/gas distribution in the cross-section as can be seen in Figure A.3. The figure depicts a stratified flow pattern where steam (red) is flowing on top of the liquid water (blue).
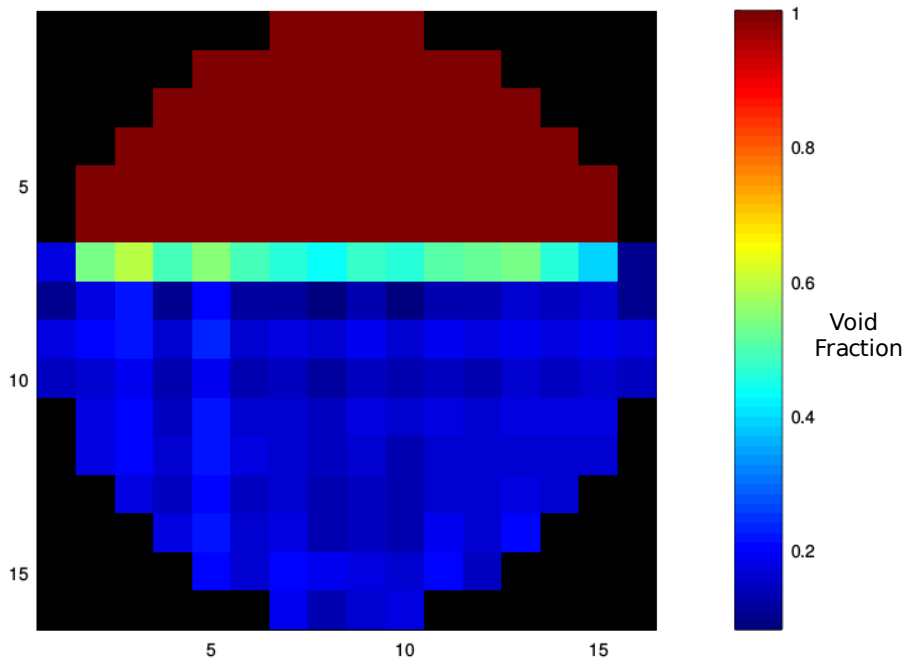
Figure A.3: Cross-sectional view of the flow pattern near the solar field outlet. The gas/liquid distribution, as described by the void fraction, illustrates a stratified flow pattern. Measurement done at 182^oC and $10bar_g$. The color bar on the left represents the void fraction.

Appendix B

Variation of Fluid Properties

During operation system pressure can vary considerably because of the inherent intermittent nature of solar energy. Hence it is beneficial to take a closer look at the change of fluid properties at varying pressure levels. The most influential fluid properties being densities of both the vapor and liquid phases and the enthalpy of evaporation.

Figure B.1 depicts the change of the enthalpy of evaporation of water at varying saturation pressures. It can be seen from the figure that the evaporation enthalpy is not constant. This means that at higher pressures, less solar energy is needed to evaporate the liquid. Moreover, it can be seen that the relationship is nonlinear in the pressure range from $0.0bar_g$ to $20.0bar_g$

The variation of fluid density under different pressures is also important, the density of the liquid phase drops with the increasing saturation pressure (because of the increasing saturation temperature) as can be seen in Figure B.2. This drop in density is also more linear at higher pressure range. The change in liquid density has to be accounted for to ensure stable control of the steam drum.

The vapor density is more affected by pressure than by temperature (in contrast to the incompressible liquid phase), hence as can be seen in Figure B.3, the density increases with increasing saturation pressure in almost a linear fashion.

The ratio between the volume of the liquid and vapor phases is also important to note since it defines the flow structure inside the absorber tube and hence is instrumental in transient analysis of the system. Figure B.4 depicts the variation of the ratio between vapor and liquid specific volumes at different saturation pressures. It can be seen that because of vapor density sensitivity to pressure increase, the ratio drops quickly at low pressures. The ratio will keep on dropping up to water's critical point where the ratio becomes 1.

Under the same mass flow and solar power conditions, this change

154
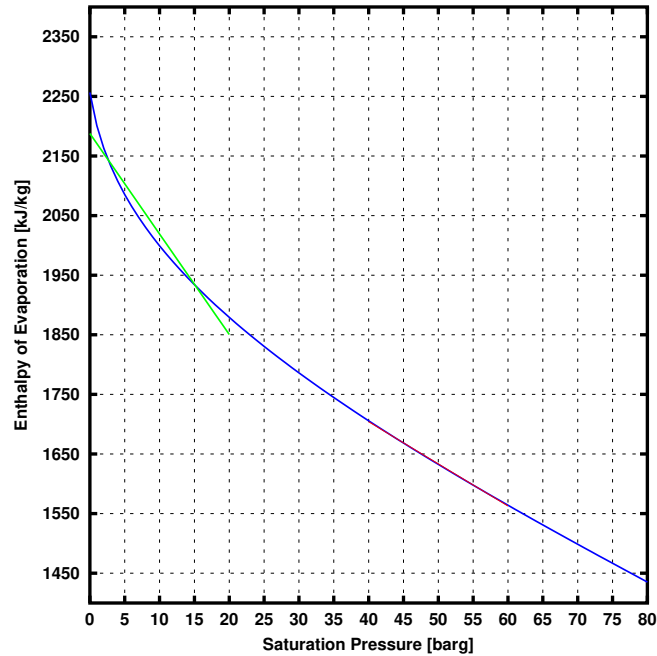
Figure B.1: Relationship between saturation pressure and enthalpy of evaporation. The relationship is more linear at higher pressures.

in the ratio between the vapor and liquid specific volumes result in a big change in the phases velocity in the absorber tube. Compared to atmospheric pressure the superficial vapor velocity is more than fifteen times higher. From flow pattern point of view, this means that at higher pressure, the possibility of having stratified flow is higher as a result of the reduced velocity.
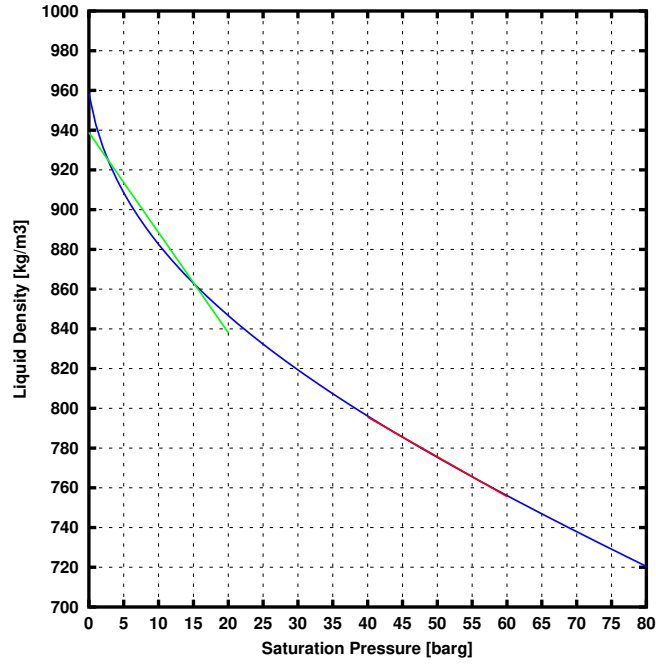
Figure B.2: Relationship between saturation pressure and liquid water density.
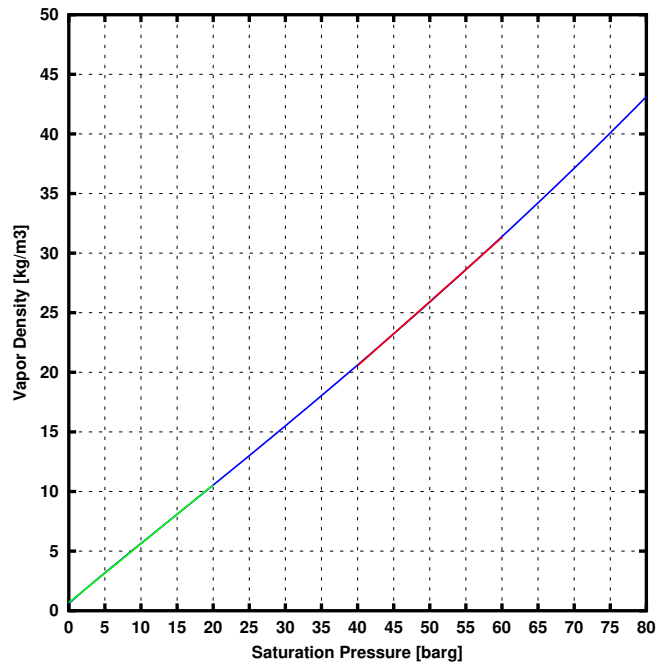
Figure B.3: Relationship between saturation pressure and vapor density.
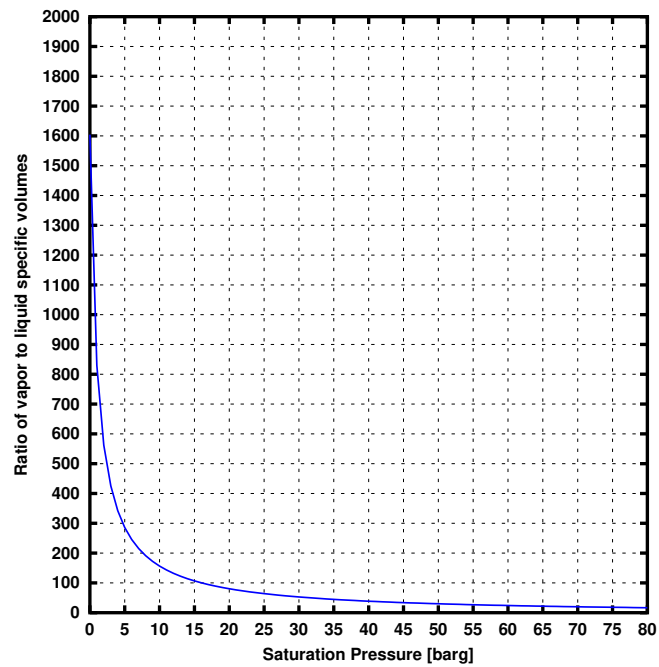
Figure B.4: Variation of the ratio between vapor and liquid specific volumes at different saturation pressures.

Bibliography

[1] Rafael Almanza, Alvaro Lentz, and Gustavo Jimenez. Receiver behavior in direct steam generation with parabolic troughs. *Solar Energy*, 61 (4):275–278, 1997. ISSN 0038092X.

[2] Gustavo Artur de Andrade, D.J. Pagano, José Domingo Álvarez, and Manuel Berenguel. A practical nmpc with robustness of stability applied to distributed solar power plants. *Solar Energy*, 92: 106 − 122, 2013. ISSN 0038-092X. doi: https://doi.org/10.1016/j. solener.2013.02.013. URL http://www.sciencedirect.com/science/ article/pii/S0038092X13000789.

[3] Michael Anger and Johannes Pernpeintner. Thermorec - heat loss test bench. Technical report, Deutsches Zentrum für Luft- und Raumfahrt (DLR), 2012.

[4] Karl Johan Åström and Rodney D Bell. Drum-boiler dynamics. *Automatica*, 36(3):363–378, 2000. ISSN 0005-1098.

[5] Antoine Aurousseau, Valéry Vuillerme, and Jean-Jacques Bezian. Control systems for direct steam generation in linear concentrating solar power plants – a review. *Renewable and Sustainable Energy Reviews*, 56:611 − 630, 2016. ISSN 1364-0321. doi: https:// doi.org/10.1016/j.rser.2015.11.083. URL http://www.sciencedirect. com/science/article/pii/S1364032115013507.

[6] Michael Berger, Andreas Haeberle, Johannes Louw, Tobias Schwind, and Christian Zahler. Mirroxx fresnel process heat collectors for industrial applications and solar cooling. In *Proceedings of the 15th International Symposium on Concentrating Solar Power and Chemical Energy Technologies, Berlin, Germany*, 2009.

[7] Michael Berger, Christian Zahler, Andreas Häberle, Johannes Louw, Tobias Schwind, and Frank Luginsland. Demonstration of direct steam generation in a mirroxx linear fresnel collector. In *proceedings of EuroSun Conference, Graz, Austria*, 2010.

[8] Michael Berger, Matthias Weckesser, Christine Weber, Jochen Döll, Alexander Morgenstern, and Andreas Häberle. Solar driven cold rooms for industrial cooling applications. *Energy Procedia*, 30:904–911, 2012. ISSN 18766102.

[9] Michael Berger, Mirko Meyer-Grünefeldt, Dirk Krüger, Klaus Hennecke, Marwan Mokhtar, and Christian Zahler. First year of operational experience with a solar process steam system for a pharmaceutical company in jordan. In *International Conference on Solar Heating and Cooling for Buildings and Industry, SHC, Istanbul, Turkey*, pages 301–307. Solar Heating and Cooling, 2015.

[10] Michael Berger, Marwan Mokhtar, Christian Zahler, Daniel Willert, Anton Neuhäuser, and Eckhard Schleicher. Two-phase flow pattern measurements with a wire mesh sensor in a direct steam generating solar thermal collector. *AIP Conference Proceedings*, 1850(1):070003, 2017. doi: 10.1063/1.4984417. URL https://aip.scitation.org/doi/abs/10.1063/1.4984417.

[11] Juergen Birnbaum, Jan Fabian Feldhoff, Markus Fichtner, Tobias Hirsch, Markus Joecker, Robert Pitz-Paal, and Gerhard Zimmermann. Steam temperature stability in a direct steam generation solar power plant. *Solar Energy*, 85(4):660–668, 2011. ISSN 0038092X.

[12] Christopher E Brennen. *Fundamentals of multiphase flow*. Cambridge University Press, 2005. ISBN 9780521848046.

[13] Frank Burkholder and Charles F Kutscher. Heat loss testing of schott's 2008 PTR70 parabolic trough receiver. Technical Report NREL/TP-550-45633, National Renewable Energy Laboratory (NREL), 2009.

[14] Eduardo Camacho and Carlos Bordons. *Model Predictive Control*. Springer-Verlag, 2003. ISBN 9780857293985.

[15] Eduardo Camacho, Manuel Berenguel, and Francisco Rubio. *Advanced control of solar plants*. Springer Berlin, 1997. ISBN 9781447109815.

[16] Eduardo Camacho, Fracisco Rubio, Manuel Berenguel, and Loreto Valenzuela. A survey on control schemes for distributed solar collector fields. part i: Modeling and basic control approaches. *Solar Energy*, 81(10):1240–1251, 2007. ISSN 0038092X.

[17] Eduardo Camacho, Francisco Rubio, Manuel Berenguel, and Loreto Valenzuela. A survey on control schemes for distributed solar collector fields. part ii: Advanced control approaches. *Solar Energy*, 81(10): 1252–1272, 2007. ISSN 0038092X.

[18] Mark Cannon. Model predictive control lecture notes. `http://www.eng.ox.ac.uk/~conmrc/mpc/`, 2013. Last Visited: 21/08/2016.

[19] Cristina M Cirre, Manuel Berenguel, Loreto Valenzuela, and Eduardo F Camacho. Feedback linearization control for a distributed solar collector field. *Control Engineering Practice*, 15(12):1533–1544, 2007. ISSN 09670661.

[20] John G Collier and John R Thome. *Convective boiling and condensation*. Oxford University Press, 1994. ISBN 9780198562962.

[21] Douglas Cooper. *Practical Process Control, Proven Methods and Best Practices for Automatic PID Control*. 2006. URL `http://www.controlguru.com/`. Last Visited: 01/06/2018.

[22] Alexandre Bittencourt de Sá, Victor César Pigozzo Filho, Lounès Tadrist, and Júlio César Passos. Direct steam generation in linear solar concentration: Experimental and modeling investigation – a review. *Renewable and Sustainable Energy Reviews*, 90:910 – 936, 2018. ISSN 1364-0321. doi: https://doi.org/10.1016/j.rser.2018.03.075. URL `http://www.sciencedirect.com/science/article/pii/S1364032118301631`.

[23] Frédéric Devernay. C/C++ minpack, 2007. URL `http://devernay.free.fr/hacks/cminpack/`. Last Visited: 01/06/2018.

[24] Jochen Döll, Hatem Bentaher, and Alexander Morgenstern. First results of a pilot installation of a solar thermally driven cold store. *International Journal of Refrigeration*, 39:77–85, 2014. ISSN 0140-7007.

[25] Richard C Dorf. *Modern control systems*. Addison-Wesley Longman Publishing Co., Inc., 1995. ISBN 9780134408330.

[26] John A Duffie and William A Beckman. *Solar engineering of thermal processes*. John Wiley & Sons, 2013. ISBN 9780471510567.

[27] Markus Eck and Tobias Hirsch. Dynamics and control of parabolic trough collector loops with direct steam generation. *Solar Energy*, 81 (2):268–279, 2007. ISSN 0038092X.

[28] Markus Eck, Eduardo Zarza, Martin Eickhoff, Jürgen Rheinländer, and Loreto Valenzuela. Applied research concerning the direct steam generation in parabolic troughs. *Solar Energy*, 74(4):341–351, 2003. ISSN 0038092X.

[29] Su Guo, Deyou Liu, Xingying Chen, Yinghao Chu, Chang Xu, Qunming Liu, and Ling Zhou. Model and control scheme for recirculation mode direct steam generation parabolic trough solar power

plants. *Applied Energy*, 202:700 − 714, 2017. ISSN 0306-2619. doi: https://doi.org/10.1016/j.apenergy.2017.05.127. URL `http://www.sciencedirect.com/science/article/pii/S0306261917306670`.

[30] Martin Haagen, Christian Zahler, Elke Zimmermann, and Mahmoud Al-Najami. Solar process steam for pharmaceutical industry in jordan. *Energy Procedia*, 70:621–625, 2015. ISSN 18766102.

[31] Andreas Häberle, Christian Zahler, Hansjörg Lerchenmüller, Max Mertins, Christof Wittwer, Franz Trieb, and Jürgen Dersch. The solarmundo line focussing fresnel collector. optical and thermal performance and cost calculations. In *proceedings of the International Symposium on Concentrated Solar Power and Chemical Energy Technologies, SolarPACES, Zurich,Switzerland*, pages 4–6, 2002.

[32] Andreas Häberle, Christian Zahler, Hansjörg Lerchenmüller, Max Mertins, Christof Wittwer, Franz Trieb, and Jürgen Dersch. The solarmundo line focussing fresnel collector. optical and thermal performance and cost calculations. In *proceedings of the 11th International Symposium on Concentrating Solar Power and Chemical Energy Technologies, Zurich,Switzerland*, 2002.

[33] Andreas Häberle, Michael Berger, Frank Luginsland, Christian Zahler, Michael Baitsch, Hans-Martin Henning, and Matthias Rommel. Linear concentrating fresnel collector for process heat applications. In *proceedings of 13th International Symposium on Concentrated Solar Power and Chemical Energy Technologies, Seville, Spain*, pages 20–23, 2006.

[34] IAWPS. Revised release on the iapws industrial formulation 1997 for the thermodynamic properties of water and steam. Technical Report IAPWS-IF97, The International Association for the Properties of Water and Steam, 2007.

[35] IEA. Key world energy statistics. Technical report, International Energy Agency, 2015. URL `http://large.stanford.edu/courses/2015/ph240/khaliq2/docs/keyworld-2015.pdf`. Last Visited : 01/06/2018.

[36] Oliver Iglauer and Christian Zahler. A new solar combined heat and power system for sustainable automobile manufacturing. *Energy Procedia*, 48:1181–1187, 2014. ISSN 18766102.

[37] IndustrialSolar. Industrial solar linear fresnel collector LF-11, 2016. URL `https://www.industrial-solar.de/app/download/6894157211/Fresnel_technical_data.pdf?t=1508927020`. Last Visited: 18/06/2018.

[38] David Q. Mayne James B. Rawlings. *Model Predictive Control: Theory and Design*. Nob Hill Publishing, 2013. ISBN 978-0-975-93770-9.

[39] Steven G. Johnson. The nlopt nonlinear-optimization package, 2007. URL `http://ab-initio.mit.edu/wiki/index.php/NLopt`. Last Visited: 01/06/2018.

[40] Nakhlé Kattan, John R Thome, and D Favrat. Flow boiling in horizontal tubes: part 3—development of a new heat transfer model based on flow pattern. *Journal of Heat Transfer*, 120(1):156–165, 1998. ISSN 00221481.

[41] Nakhlé Kattan, JR Thome, and D Favrat. Flow boiling in horizontal tubes: Part 1—development of a diabatic two-phase flow pattern map. *Journal of Heat Transfer*, 120(1):140–147, 1998. ISSN 00221481.

[42] Nakhlé Kattan, JR Thome, and D Favrat. Flow boiling in horizontal tubes: Part 2—new heat transfer data for five refrigerants. *Journal of heat transfer*, 120(1):148–155, 1998. ISSN 00221481.

[43] Hyoungrock Kim and Sangmin Choi. A model on water level dynamics in natural circulation drum-type boilers. *International Communications in Heat and Mass Transfer*, 32(6):786–796, 2005. ISSN 07351933.

[44] Dirk Krüger, Michael Berger, Marwan Mokhtar, Lisa Willwerth, Christian Zahler, Mahmoud Al-Najami, and Klaus Hennecke. Experiences with industrial solar process steam generation in jordan. *AIP Conference Proceedings*, 1850(1):180003, 2017. doi: 10.1063/1.4984570.

[45] Jacob Mattingley, Yang Wang, and Stephen Boyd. Receding horizon control. *Control Systems, IEEE*, 31(3):52–65, 2011. ISSN 1066033X.

[46] David Q. Mayne, James B. Rawlings, Christopher V. Rao, and Pierre O.M. Scokaert. Constrained model predictive control: Stability and optimality. *Automatica*, 36(6):789–814, 6 2000. ISSN 00051098. doi: 10.1016/S0005-1098(99)00214-9.

[47] Adrian Meaburn and F. Michael Hughes. A simple predictive controller for use on large scale arrays of parabolic trough collectors. *Solar Energy*, 56(6):583–595, 1996. ISSN 0038092X.

[48] Max Mertins. *Technische und wirtschaftliche Analyse von horizontalen Fresnel-Kollektoren*. PhD thesis, Universität Karlsruhe, 2009.

[49] Marwan Mokhtar, Michael Begrer, Christian Zahler, Dirk Krüger, Heiko Schenk, and Robert Stieglitz. Direct steam generation for process heat using fresnel collectors. *International Journal of Thermal and Environmental Engineering*, 10(1):3–9, 2015. ISSN 19237316.

[50] Jorge J Moré, Burton S Garbow, and Kenneth E Hillstrom. User guide for minpack-1. Technical report, CM-P00068642, 1980.

[51] Katsuhiko Ogata. *Modern control engineering*. Prentice Hall, 2002. ISBN 0130432458.

[52] Johannes Pernpeintner. Measurement of parabolic trough receiver thermal loss power and relative optical efficiency under solar simulator light. Technical report, Deutsches Zentrum für Luft- und Raumfahrt (DLR), 2012.

[53] Heiko Pietruske and Horst-Michael Prasser. Wire-mesh sensors for high-resolving two-phase flow studies at high pressures and temperatures. *Flow measurement and instrumentation*, 18(2):87–94, 2007. ISSN 09555986.

[54] Michael JD Powell. A direct search optimization method that models the objective and constraint functions by linear interpolation. In *Advances in optimization and numerical analysis*, pages 51–67. Springer, 1994. ISBN 9789048143580.

[55] Michael JD Powell. The BOBYQA algorithm for bound constrained optimization without derivatives. *Cambridge NA Report NA2009/06, University of Cambridge, Cambridge*, 2009.

[56] Horst Michael Prasser, Arnd Böttger, and Jochen Zschau. A new electrode-mesh tomograph for gas–liquid flows. *Flow measurement and instrumentation*, 9(2):111–119, 1998. ISSN 09555986.

[57] William H Press, Saul A Teukolsky, William T Vetterling, and Brian P Flannery. *Numerical recipes in C*, volume 2. Cambridge university press Cambridge, 1996. ISBN 9780521375160.

[58] John D Pye. *System modelling of the Compact Linear Fresnel Reflector*. PhD thesis, University of New South Wales, 2008.

[59] John Rossiter. *Model Predictive Control Ebook*. University of Sheffield, 2014. URL `http://controleducation.group.shef.ac.uk/indexwebbook.html`. Last Visited: 01/06/2018.

[60] United Nations Climate Change Secretariat. Historic paris agreement on climate change. 195 nations set path to keep temperature rise well below 2 degrees celsius, 2015. URL `http://unfccc.int/files/press/press_releases_advisories/application/pdf/pr20151112_cop21_final.pdf`. Last Visited: 01/06/2018.

[61] Dieter Steiner. *VDI-Wärmeatlas (VDI Heat Atlas), Section Hbb*. Springer, 2006. ISBN 9783642199806.

[62] Wolf-Dieter Steinmann and Markus Eck. Buffer storage for direct steam generation. *Solar Energy*, 80(10):1277–1282, 2006. ISSN 0038092X.

[63] teletronic Rossendorf GmbH. Wire mesh sensor system WMS200 manual. Technical report, 2013.

[64] John R Thome. *Engineering data book III*. Wolverine Tube Inc, 2004.

[65] John R Thome and Jean El Hajal. Two-phase flow pattern map for evaporation in horizontal tubes: latest version. *Heat Transfer Engineering*, 24(6):3–10, 2003. ISSN 15210537. doi: 10.1080/714044410.

[66] Loreto Valenzuela, Eduardo Zarza, Manuel Berenguel, and Eduardo F Camacho. Control concepts for direct steam generation in parabolic troughs. *Solar Energy*, 78(2):301–311, 2005. ISSN 0038092X.

[67] Loreto Valenzuela, Eduardo Zarza, Manuel Berenguel, and Eduardo F Camacho. Control scheme for direct steam generation in parabolic troughs under recirculation operation mode. *Solar energy*, 80(1):1–17, 2006. ISSN 0038092X.

[68] NB Vargaftik, BN Volkov, and LD Voljak. International tables of the surface tension of water. *Journal of Physical and Chemical Reference Data*, 12(3):817–820, 1983. ISSN 00472689.

[69] K. Warwick and D. Rees. *Industrial Digital Control Systems*. IEEE control engineering series. Peter Peregrinus, 1988. ISBN 9780863411373.

[70] Christine Weber, Michael Berger, Florian Mehling, Alexander Heinrich, and Tomas Núñez. Solar cooling with water-ammonia absorption chillers and concentrating solar collector–operational experience. *International Journal of Refrigeration*, 2013. ISSN 0140-7007.

[71] Christian Zahler and Oliver Iglauer. Solar process heat for sustainable automobile manufacturing. *Energy Procedia*, 30:775–782, 2012. ISSN 18766102.

[72] Christian Zahler, Michael Berger, and Johannes Louw. Industrial solar fresnel collectors powering the largest solar cooling system in the middle east for a football stadium. In *proceedings of the 17th International Symposium on Concentrating Solar Power and Chemical Energy Technologies, Granada, Spain*, 2011.

[73] Eduardo Zarza, L. Gonzalez, Angel Morales, Enrique Rojas, Klaus Hennecke, Markus Eck, Olaf Goebel, P. Geskes, S. Zunft, F. Lippke, U. Hermann, and J. Langenkamp. Diss-phase i project. Technical Report JOR3-CT95-0058, CIEMAT,DLR,ZSW,PILKINGTON, 1998.

[74] Eduardo Zarza, Loreto Valenzuela, Javier Leon, Klaus Hennecke, Markus Eck, H Weyers, Martin Eickhoff, et al. Direct steam generation in parabolic troughs: Final results and conclusions of the diss project. *Energy*, 29(5):635–644, 2004. ISSN 03605442.